Stability of compressible boundary layers with a velocity overshoot

Adam Peter Tunney

Supervisory Panel

Prof. Jim Denier (University of Auckland)
Dr. Trent Mattner (University of Adelaide)
Dr. John Cater (University of Auckland)

A thesis submitted in fulfilment of the requirements for the degree of Doctor of Philosophy in Engineering Science, the University of Auckland, 2016.

DEPARTMENT OF ENGINEERING SCIENCE
UNIVERSITY OF AUCKLAND

Abstract

The stability of compressible boundary layers is advanced in the literature, however, boundary layers with a velocity overshoot are yet to be considered. These boundary layers can arise when the surface over which the fluid flows is heated, and an accelerating pressure gradient is applied. The analytic behaviour of solutions of the governing equations was investigated in order to demonstrate the existence of velocity overshoot. An analysis of the structure of these solutions in the large Mach number limit is given. The local maximum in the streamwise velocity and the presence of multiple generalised points of inflection in these boundary layers, indicate that the stability properties of the flow are likely to be affected. A numerical study of the inviscid stability behaviour of a class of boundary layers with overshoot, reveals a new mode of instability, in addition to the classical first- and higher-mode solutions previously described in the literature. The circumstances under which this new unstable mode can attain higher growth rates than the classical modes are explored together with its role in laminar-turbulent transition. To support, and validate, the numerical results an analytic solution of the new mode in the small wavenumber limit was derived from which it is demonstrated that this mode propagates at a wavespeed equal to the maximum boundary-layer velocity. The inviscid stability results were extended by demonstrating that they match with the viscous stability behaviour in the large Reynolds number limit. In cases where the velocity overshoot and/or the Mach number are sufficiently large, the inflectional and the new non-inflectional neutral modes may propagate at a wavespeed that is no longer subsonic relative to the free-stream velocity; this is shown to render the basic boundary-layer flow stable to the first-mode and the newly discovered new-mode disturbance.

Acknowledgements

This thesis would not have been accomplished without the support of others. Firstly, I am indebted to Prof. Jim Denier; without his unwavering support this thesis would simply not have eventuated. His broad technical knowledge has been invaluable in all stages of the research. Dr. Trent Mattner has been involved in my research since my Honours project at the University of Adelaide and his assistance in all things of a computational nature was much appreciated. Dr. John Cater was always the first to provide feedback on things I had written and his enthusiasm kept me on track for a timely submission.

The funding support from the University of Auckland was integral to the completion of my thesis and the development of my career. The experience of spending time at world-class overseas institutions and presenting my research at international conferences created academic connections that could prove useful in the future.

I am thankful for the friendships fostered with fellow postgraduate students at Adelaide, Auckland and beyond that enabled experiences and difficulties in the research process to be shared. While not involved in the thesis whatsoever, I would also like to thank all the other friends who have provided an escape from research so that I could maintain a semblance of sanity.

Finally, the most heartfelt thanks are for my family and especially my parents Peter and Kyra who have always been there to encourage and believe in me throughout my long and arduous journey as a student.

Contents

Graduate Centre
The Clock Tower – East Wing
22 Princes Street, Auckland
Phone: +64 9 373 7599 ext 81021

THE UNIVERSITY OF AUCKLAND
SCHOOL OF GRADUATE STUDIES

Co-Authorship Form

This form is to accompany the submission of any PhD that contains published or unpublished co-authored work. **Please include one copy of this form for each co-authored work.** Completed forms should be included in all copies of your thesis submitted for examination and library deposit (including digital deposit), following your thesis Acknowledgements. Co-authored works may be included in a thesis if the candidate has written all or the majority of the text and had their contribution confirmed by all co-authors as not less than 65%.

Please indicate the chapter/section/pages of this thesis that are extracted from a co-authored work and give the title and publication details or details of submission of the co-authored work. Section 4.1 - 4.2 "A new minimal mode of instability in compressible boundary-layer flows" Journal of Fluid Mechanics 785 p 301-323 Nov 2015	
Nature of contribution by PhD candidate	Mathematical Analysis and majority of text
Extent of contribution by PhD candidate (%)	70

CO-AUTHORS

Name	Nature of Contribution
J. P. Denier	Text, critique of analysis, editing
T. W. Mattner	Critique of analysis, editing
J. E. Cater	Critique of analysis, editing.

Certification by Co-Authors

The undersigned hereby certify that:

- the above statement correctly reflects the nature and extent of the PhD candidate's contribution to this work, and the nature of the contribution of each of the co-authors; and
- that the candidate wrote all or the majority of the text.

Name	Signature	Date
Jim Denier	Jim Denier	14/2/2016
TRENT MATTNER	T. Mattner	15/2/2016
JOHN CATER	[illegible]	16/2/2016

Chapter 1

Background

The efficiency of aerodynamic surfaces, such as aircraft bodies and turbine blades, are affected by the transition of the fluid flow over the surface from laminar to turbulent. The nature of the transition process is complex and may follow many paths. For high-speed external flows, small natural disturbances may cause the transition process due to the laminar flow being unstable. The development of efficient high-speed aircraft requires an understanding of the both the structure of the flow over the surface (the boundary layer) and its stability characteristics. In applications where local velocities approach or exceed the speed of sound, the fluid flow is compressible, which along with other supersonic and hypersonic phenomena, increases the complexity of both the boundary-layer and stability problems. In this thesis, compressible boundary layers where the surface is heated and an accelerating pressure gradient is applied are investigated. These boundary layers are special in that they contain a region where the fluid flows faster than the flow in the free stream and has an internal maximum velocity, a so-called "overshoot". This is in contrast to most cases where the velocity profile in the boundary layer is monotonic. The structure and stability behaviour of overshoot boundary layers is the subject of the thesis.

1.1 Historical Background

The first results concerning the stability of external fluid flows were those of Lord Rayleigh (1879), who demonstrated that an incompressible, inviscid, parallel, external fluid flow was stable to small disturbances should the velocity profile not contain a point of inflection, otherwise the disturbance amplitude grows exponentially. The importance of viscosity in external flows was recognised by Prandtl (1928), who identified the boundary layer, a thin region near the surface where viscosity is still important. This solved an outstanding issue that inviscid external flows were not compatible with the accepted no-slip boundary condition, which forbids tangential fluid motion at the surface. Blasius (1950) determined that the thickness of the boundary layer decreases with increasing flow speed and developed a similarity solution to the equations governing fluid flow in the boundary layer over a flat plate, often called the Blasius boundary layer. The velocity profile of Blasius was non-inflectional and hence it was expected to be stable. Similarity solutions for different arrangements were developed, for example, the equations of Falkner and Skan (1931), further investigated by Hartree (1937), extended Blasius' similarity equation to the case where the external velocity varies along the surface.

Including the effects of fluid compressibility increases the complexity of the boundary-layer equations; the energy and momentum equations become linked through dissipation terms whereas in the incompressible case they may be solved independently. Despite this, the co-ordinate transform of Dorodnitsyn (1942) and Howarth (1948) enabled a variety of similarity solutions for compressible boundary-layer flows. Stewartson (1964) provides an excellent overview of compressible boundary-layer theory, covering solutions including heat transfer and applied pressure gradients, separation, three-dimensional boundary layers and interaction with shocks.

While viscosity was previously assumed to be stabilising in all applications, the independent work of Taylor and Prandtl in the early 20th century suggested that viscous flows can be unstable while the corresponding inviscid flow is stable. **?** first presented a framework for solving the viscous stability problem at large

Reynolds number and resolved the viscous critical layer in a bounded flow. Tollmien (1931) and Schlichting (1933) developed a theory for viscous, parallel boundary-layer instability and numerical results were calculated to predict the transition to turbulence. This theory was popularised when Schubauer (1948) presented experimental results confirming that the so-called Tollmien-Schlichting (TS) waves indeed existed and were a precursor to laminar-turbulent transition. Smith and Gamberoni (1956) and Van Ingen (1956) subsequently developed the so-called "e^N method", an empirical method using linear stability results to predict the location of, and the initial disturbance causing boundary-layer transition. This method is still in contemporary use (Fedorov, 2015).

Early stability theory assumed that the flow analysed was parallel; it only varied in a direction normal to the surface. However, in boundary-layer flows there is some streamwise development (asymptotically small in the inviscid limit). Gaster (1974) investigated the effects of the streamwise development by applying the method of successive approximations to introduce non-parallel correction terms to the parallel stability theory. An internally self-consistent method was developed by Smith (1979), who described a three-tiered structure close to the surface in which the lower-branch TS instability is described, based on the scaling first noted by Lin (1945). Later, the five-tiered structure describing the upper branch was described (Bodonyi and Smith, 1981). While the three-tiered structure is similar to that of a self-separating flow (i.e. Stewartson and Williams, 1969), the connection with the TS instability was a crucial finding and preceded many further results in the incompressible theory.

The first stability analysis including the effects of compressibility was that of Küchemann (1938); however, assumptions made regarding the fluid properties and velocity profile were later proved to be too restrictive. The study of Lees and Lin (1946) was significant in that the theories of Rayleigh were generalised to accommodate compressible flows. A direct outcome of this was that compressible flat-plate boundary layers were demonstrated to be inviscidly unstable, as opposed to the incompressible (Blasius) case. In addition to the inviscid analysis, the viscous stability at high Reynolds numbers was also presented, to extend the incompress-

ible analysis of Lin (1945). A follow-up study by Lees (1947) presented numerical results for neutral stability curves of the compressible version of the TS instability and suggested that it may be diminished by sufficient removal of heat from the boundary layer. However, the analysis and extensive numerical calculations of Mack (1969) uncovered the existence of additional instability modes (of an acoustic nature) in compressible boundary layers that are destabilised through the removal of heat. The three- and five-tiered structures of the lower- and upper-branch TS instability were extended to compressible flows by Smith (1989) and Gajjar (1993) respectively. An outcome of these studies was that for sufficiently high Mach numbers, the TS instability may develop at a scale comparable to the development of the basic state, so that the non-parallel effects are present at leading order, contradicting parallel and quasi-parallel studies where the non-parallel effects are lower-order corrections. In the hypersonic (high Mach number) limit, the contribution of attached shock waves to increasing the growth rates of viscous modes was examined by Cowley and Hall (1990) and the evolution of the acoustic modes and the vorticity mode was analysed by Smith and Brown (1990) to compare with the earlier high but finite Mach number numerical results of Mack.

The preceding discussion focuses on the stability behaviour of two-dimensional flows over flat surfaces. Two other classes of primary instability have also been the focus of research on external flows. When the surface over which the fluid is flowing is concave, the existence of a centrifugal vortex instability was established by Görtler (1954), after whom the instability is named. The analytical complexity of the Görtler instability, requiring the solution of partial differential equations, meant that strong results were not available until much later. The development of these results was reviewed comprehensively by Hall (1990). The final class of primary instability are crossflow vortex instabilities, which may occur in three-dimensional boundary layers. Due to the difficulty in solving the full three-dimensional boundary-layer equations for general cases, studies of this instability are generally limited to three-dimensional boundary layers with an exact solution, such as Von Kármán's rotating disc (Gregory et al. 1955, Hall 1986, Bassom and Gajjar 1988) and the swept attachment-line boundary layer in the vicinity of a

leading edge (i.e. Hall et al., 1984).

In practical arrangements, aerodynamic surfaces are not flat and are finite in size, so the flow is necessarily three-dimensional and boundary-layer development is relevant. Each of the three primary instabilities may therefore be present and in turn, interaction between the primary instabilities may occur. Numerous studies have demonstrated that the growth rates of TS waves can be increased, in some cases dramatically, by both Görtler (i.e. Nayfeh 1981, Malik 1986) and crossflow vortices (i.e. Reed 1984, Reed 1985, Bassom and Hall 1990) and these interactions could ultimately cause transition.

Stability theory operates on the assumption that a disturbance is already present in the boundary layer. An important aspect of the overall boundary-layer transition process is receptivity, which considers the nature of external disturbances (i.e. sound, freestream turbulence, surface imperfections) and how they perturb the base boundary-layer state. It is receptivity theory that determines the initial conditions of disturbances in the boundary layer that grow (or decay) due to the stability characteristics. The concept of receptivity is due to Morkovin (1969) and the theory is summarised comprehensively by Saric et al. (2002) and Reed et al. (2015).

Much recent research has searched for solutions for delaying the transition process on bodies in high Mach number flows. Generally these involve modifying aspects of the flow geometry to reduce or delay the growth of the controlling instability. Current hypersonic vehicles are predominantly designed to resemble nearly two-dimensional wedges (to minimise Görtler and crossflow instabilities) with sharp leading edges and the acoustic second (Mack) mode is dominant (Fedorov, 2011). The application of a porous coating to absorb acoustic disturbances was simulated numerically (Fedorov et al., 2001), experimentally (Rasheed et al., 2002) and later through direct numerical simulation (Wartemann et al., 2012) and was shown to delay transition should the pore size be chosen correctly. Stephen and Michael (2013) considered the effect of a porous surface on the first-mode instability, which has the potential to be dominant should the acoustic (second- and higher-mode) disturbances be sufficiently absorbed. Other recent successful investigations include the injection of carbon dioxide into the boundary layer, which may absorb

the disturbance through molecular vibrations matching the disturbance frequency (Leyva, 2009), and using a "wavy" surface (Bountin et al., 2013).

1.2 Boundary-Layer Formulation

1.2.1 Governing Flow Equations

The models that govern the behaviour of a compressible fluid take advantage of the continuum hypothesis. Rather than modelling many discrete molecules with individual properties (i.e. velocity, temperature), the fluid is taken to be a continuous material with properties that are smooth. That is, an increasingly smaller element of the continuum is still representative of the fluid.

The continuum hypothesis is accurate provided that the fluid's mean free path, L_m – the average distance a molecule travels between collisions – is much smaller than a characteristic length scale L of the system. The Knudsen number,

$$\mathrm{Kn} = \frac{L_m}{L}$$

must be small for the continuum hypothesis to be valid. Under these conditions, conservation laws may be applied on an infinitesimal fluid element. The equations governing the flow of a compressible fluid consist of conservation of mass

$$\frac{\partial \rho}{\partial t} + \nabla \cdot (\rho \mathbf{u}) = 0, \tag{1.1}$$

the conservation of momentum in each Cartesian direction

$$\rho \frac{\mathrm{D}\mathbf{u}}{\mathrm{D}t} = -\nabla p + \left[2\nabla \cdot (\mu \mathbf{E}) + \nabla \left(\left(\lambda - \frac{2}{3}\mu \right) \nabla \cdot \mathbf{u} \right) \right], \tag{1.2}$$

the conservation of energy

$$\rho \frac{\mathrm{D}}{\mathrm{D}t} (c_v T) = \frac{\mathrm{D}p}{\mathrm{D}t} + \nabla \cdot (\kappa \nabla T) + \Phi, \tag{1.3}$$

and an equation of state

$$p = R_g \rho T, \tag{1.4}$$

where

$$\frac{\mathrm{D}}{\mathrm{D}t} = \frac{\partial}{\partial t} + \mathbf{u} \cdot \nabla$$

is the material derivative operator and the rate-of-strain tensor $\mathbf{E}$ is defined with components

$$e_{ij} = \frac{1}{2}\left(\frac{\partial u_i}{\partial x_j} + \frac{\partial u_j}{\partial x_i}\right),$$

the viscous dissipation

$$\Phi = 2\mu\mathbf{E} : \mathbf{E} + \left(\lambda - \frac{2}{3}\mu\right)(\nabla \cdot \mathbf{u})^2,$$

and the ideal gas constant

$$R_g = c_p - c_v. \tag{1.5}$$

The dimensional quantities are non-dimensionalised in the following manner: Displacements in the streamwise, normal and spanwise directions; x, y and z respectively, are scaled by a nominal length scale L, respective velocities u, v and w by u_e, time t by L/u_e, density ρ by ρ_e, pressure p by $\rho_e u_e^2$, temperature T by T_e, thermal conductivity κ by κ_e, dynamic viscosity μ by μ_e and bulk viscosity λ by λ_e. The subscript e corresponds to a reference value, which will be taken to be the value of the quantity at the edge of the boundary layer. When equations (1.1)-(1.3) are non-dimensionalised in this manner a number of similarity quantities arise. These are the Reynolds number

$$Re = \frac{\rho_e u_e L}{\mu_e},$$

the heat capacity ratio

$$\gamma = \frac{c_p}{c_v}, \tag{1.6}$$

where c_p and c_v are the constant-pressure and constant-volume heat capacities of the fluid, the Mach number

$$M = \frac{u_e}{a_e},$$

where a_e is the (dimensional) speed of sound in the freestream, and the Prandtl number

$$Pr = \frac{c_p \mu}{\kappa},$$

which is assumed to be constant to provide a relation between κ and μ.

1.2.2 The No-Slip Condition

When a fluid interacts with a surface it is accepted that at the surface there is a zero relative fluid velocity. This may be inferred from the continuum assumption, or from experimental evidence. Ruban and Gajjar (2014) state "The latter [experimental evidence] is ample and supports the view that the no-slip condition is a universal law of fluid dynamics."

1.2.3 Boundary-Layer Problem

Consider the steady, uniform flow over a surface with $\mu \ll 1$ and with no spanwise motion. The governing equations are singular in the limit $\mu \to 0$; the Euler equations that result provide the inviscid, external solution. The desired behaviour of no slip at the surface cannot be met in this singular limit. It was proposed by Prandtl (1928) that a thin boundary layer exists near the surface where viscosity is still important and the no-slip boundary condition may be realised.

Consider the scaled normal co-ordinate $Y = y/\delta$, where $\delta \ll 1$ is the thickness of the boundary layer. From the continuity equation (1.1),

$$\frac{\partial}{\partial x}(\rho u) + \frac{1}{\delta}\frac{\partial}{\partial Y}(\rho v) = 0.$$

In order to develop a non-trivial solution, v must be $O(\delta)$, hence the scaling $v = \delta V$ is taken. The continuity equation then becomes

$$\frac{\partial}{\partial x}(\rho u) + \frac{\partial}{\partial Y}(\rho V) = 0. \tag{1.7}$$

The conservation of momentum in the x-direction; the streamwise component of the vector equation (1.2) becomes

$$\begin{aligned}\rho\left[u\frac{\partial u}{\partial x} + V\frac{\partial u}{\partial Y}\right] &= -\frac{\partial p}{\partial x} + \frac{1}{\delta^2}\frac{\partial}{\partial Y}\left(\mu\frac{\partial u}{\partial Y}\right)\\ &+ \frac{\partial}{\partial x}\left[2\mu\frac{\partial u}{\partial x} + \left(\lambda - \frac{2}{3}\mu\right)\left(\frac{\partial u}{\partial x} + \frac{\partial V}{\partial Y}\right)\right] + \frac{\partial}{\partial Y}\left(\mu\frac{\partial V}{\partial x}\right).\end{aligned} \tag{1.8}$$

To maintain the effect of viscosity, the balance $\mu\delta^{-2} \sim O(1)$ is chosen, so $\delta \sim O(\mu^{1/2})$ confirming the requirement for a small δ. Taking the leading order terms,

the x- and y-components of (1.2) become

$$\rho\left[u\frac{\partial u}{\partial x}+V\frac{\partial u}{\partial Y}\right]=-\frac{\partial p}{\partial x}+\frac{\partial}{\partial Y}\left(\mu\frac{\partial u}{\partial y}\right) \tag{1.9}$$

and

$$0=-\frac{\partial p}{\partial y} \tag{1.10}$$

respectively. Equation (1.3) becomes

$$\rho c_v\left[u\frac{\partial T}{\partial x}+V\frac{\partial T}{\partial Y}\right]=-\left[u\frac{\partial p}{\partial x}+V\frac{\partial p}{\partial Y}\right]+\frac{1}{Pr}\left[\frac{\partial}{\partial Y}\left(\mu c_v\frac{\partial T}{\partial Y}\right)\right]+\mu\frac{\partial u}{\partial y}^2, \tag{1.11}$$

and the equation of state (1.24) remains unchanged.

1.2.4 Conversion to Enthalpy

The energy equation (1.11) is rewritten as

$$\begin{aligned}\rho\left[u\frac{\partial H}{\partial x}+V\frac{\partial H}{\partial Y}\right]=\rho u^2\frac{\partial u}{\partial x}+\rho uV\frac{\partial U}{\partial Y}+u\frac{\partial p}{\partial x}-\frac{1}{Pr}\frac{\partial}{\partial Y}\left(\mu u\frac{\partial u}{\partial Y}\right)\\ +\mu\frac{\partial u}{\partial Y}^2+\frac{1}{Pr}\frac{\partial}{\partial Y}\left(\mu\frac{\partial H}{\partial Y}\right),\end{aligned} \tag{1.12}$$

where equation (1.10) is used and $H=c_vT+\frac{1}{2}u^2$ is the total enthalpy; a sum of the internal energy (c_vT) and kinetic energy. This form is advantageous for exploring the properties of a compressible boundary layer. The remaining pressure term is removed by adding u(1.9)

$$\rho\left[u\frac{\partial H}{\partial x}+V\frac{\partial H}{\partial Y}\right]=\frac{1}{Pr}\frac{\partial}{\partial Y}\left(\mu\frac{\partial H}{\partial Y}\right)+\left(1-\frac{1}{Pr}\right)\left[\mu\frac{\partial u}{\partial y}^2+\frac{\partial}{\partial Y}\left(\mu\frac{\partial u}{\partial Y}\right)\right]. \tag{1.13}$$

1.2.5 The Stream Function

In order to eliminate the continuity equation (1.7) from the problem, the stream function $\psi(x,Y)$ defined by

$$\rho u=\frac{\partial\psi}{\partial Y}, \tag{1.14}$$

$$-\rho v=\frac{\partial\psi}{\partial x}, \tag{1.15}$$

is implemented. Two equations remain, the conservation of streamwise momentum

$$\frac{\partial\psi}{\partial Y}\frac{\partial}{\partial x}\left(\frac{1}{\rho}\frac{\partial\psi}{\partial Y}\right)-\frac{\partial\psi}{\partial x}\frac{\partial}{\partial Y}\left(\frac{1}{\rho}\frac{\partial\psi}{\partial Y}\right)=\frac{\mathrm{d}p}{\mathrm{d}x}+\frac{\partial}{\partial Y}\left[\mu\frac{\partial}{\partial Y}\left(\frac{1}{\rho}\frac{\partial\psi}{\partial Y}\right)\right] \tag{1.16}$$

and conservation of energy

$$\begin{aligned}\frac{\partial\psi}{\partial Y}\frac{\partial H}{\partial x}-\frac{\partial\psi}{\partial x}\frac{\partial H}{\partial Y}=&\frac{1}{Pr}\frac{\partial}{\partial Y}\left(\mu\frac{\partial H}{\partial Y}\right)+\\ \left(1-\frac{1}{Pr}\right)&\left[\mu\left(\frac{\partial}{\partial Y}\left(\frac{1}{\rho}\frac{\partial\psi}{\partial Y}\right)\right)^2+\frac{1}{p}\frac{\partial\psi}{\partial Y}\frac{\partial}{\partial Y}\left(\mu\frac{\partial}{\partial Y}\left(\frac{1}{\rho}\frac{\partial\psi}{\partial Y}\right)\right)\right].\end{aligned} \tag{1.17}$$

In doing this the order of the system has increased by one, creating the need for another boundary condition. Without loss of generality,

$$\psi(x,0)=0 \tag{1.18}$$

is taken.

1.2.6 Similarity Solution

Under certain conditions, there are variable transformations available that allow the boundary-layer equations (1.16)-(1.17) to be written as a set of ordinary differential equations. These conditions are explored in more detail in Chapter 2.1.

1.2.7 Velocity Overshoot

Of interest in the body of work presented here is a specific class of compressible boundary layer whereby the flow is accelerated; u_e is then an increasing function of x and the surface is heated so that thermal energy is added into the boundary layer. The increasing edge velocity may also be considered as a favourable pressure gradient. This class of boundary-layer solutions is notable for containing an internal velocity maximum higher than the freestream velocity. This is caused by the high temperature of the fluid near the surface, which is coincident with a low fluid density, and the pressure gradient which increases acceleration in this region (Stewartson, 1964).

The existence of velocity overshoot was first described by Brown and Donoughe (1951), who presented numerical solutions for compressible, porous-surface boundary layers with variable heat transfer and pressure gradients. Li and Nagamatsu (1955) also presented similar results for non-porous surfaces and postulated that a critical amount of surface heating was required to develop a velocity overshoot.

Cohen and Reshotko (1955), however, provided some asymptotic analysis arguing the existence of overshoot for any amount of surface heating. This analysis was restricted to the case of $Pr = 1$ and $\mu \propto T$ however several terms were omitted without adequate justification. McLeod and Serrin (1968a,b) considered the same problem in greater detail and provided a rigorous analysis demonstrating the existence of overshoot with these restrictions.

Following this, there has been little in the literature concerning this class of boundary-layers. However, a similar case of this velocity overshoot phenomena is present in other boundary-layer problems, such as on a cone (Moore, 1953) or that of a yawed, infinite cylinder (Reshotko and Beckwith, 1958).

A similar phenomena occurs in incompressible boundary layers when the surface is heated; the change in fluid density causes a buoyancy-driven pressure gradient and the physical effect causing the velocity overshoot is similar. In this case, the velocity overshoot affects the stability structure and is strongly destabilising (Denier and Mureithi, 1996, Mureithi et al., 1997).

Local maxima in the velocity profile may also occur in unsteady boundary layers. Cowley and Smith (1985) investigated a model of an oscillating (Stokes) boundary-layer model and identified a low-wavenumber instability that compares well with the work of **?** on incompressible jet-like flows.

1.3 Linear Stability Theory

For the linear stability analysis, the variables in the governing equations are non-dimensionalised in the manner set out in section 1.2.1, however the length scale is now chosen to be δL, where δ is the thickness of the boundary layer. Henceforth, the boundary-layer normal coordinate Y will be referred to as y. It has already been ascertained that $\delta \sim (\mu^{1/2})$ and to maintain the correct dimensions of the length scale

$$\delta = Re^{-\frac{1}{2}} = \left(\frac{\mu_e}{\rho_e u_e L}\right)^{\frac{1}{2}} \tag{1.19}$$

is chosen and a new definition of the Reynolds number using this length scale, called the stability Reynolds number, is

$$R = \frac{\rho_e u_e \delta L}{\mu_e} = \frac{\rho_e u_e}{\mu_e}\left(\frac{\mu_e L}{\rho_e u_e}\right)^{\frac{1}{2}} = \left(\frac{\rho_e u_e L}{\mu_e}\right)^{\frac{1}{2}} = Re^{\frac{1}{2}}. \tag{1.20}$$

With these definitions the governing flow equations are the conservation of mass

$$\frac{\partial \rho}{\partial t} + \nabla \cdot (\rho \mathbf{u}) = 0 \tag{1.21}$$

the conservation of momentum in each Cartesian direction

$$\rho \frac{\mathrm{D}\mathbf{u}}{\mathrm{D}t} = -\nabla p + \frac{1}{R}\left[2\nabla \cdot (\mu \mathbf{E}) + \nabla\left(\left(\lambda - \frac{2}{3}\mu\right)\nabla \cdot \mathbf{u}\right)\right], \tag{1.22}$$

the conservation of energy

$$\rho \frac{\mathrm{D}T}{\mathrm{D}t} = (\gamma - 1)\, M^2 \frac{\mathrm{D}p}{\mathrm{D}t} + \frac{1}{PrR}\nabla \cdot (\mu \nabla T) + \frac{(\gamma - 1)\, M^2}{R}\Phi, \tag{1.23}$$

and the equation of state

$$\gamma M^2 p = \rho T. \tag{1.24}$$

Now consider a perturbation expansion of these equations in the form $u = \bar{u} + \tilde{u}$, $v = \bar{v} + \tilde{v}$, $w = \bar{w} + \tilde{w}$, $\rho = \bar{\rho} + \tilde{\rho}$, $p = \bar{p} + \tilde{p}$, $T = \bar{T} + \tilde{T}$, $\mu = \bar{\mu} + \tilde{\mu}$ and $\lambda = \bar{\lambda} + \tilde{\lambda}$, where barred quantities are the known boundary-layer solution and tilde quantities are small perturbations. As μ and λ are solely functions of temperature, these perturbations have the form

$$\tilde{\mu} = \frac{\mathrm{d}\mu}{\mathrm{d}T}\tilde{T}, \quad \tilde{\lambda} = \frac{\mathrm{d}\lambda}{\mathrm{d}T}\tilde{T}.$$

This expansion is introduced into (1.21)-(1.24), the original equations implementing the known solution are subtracted, and products of disturbance quantities and/or their derivatives are discarded. The known solution implemented is a parallelised solution of the boundary-layer equations (1.16)-(1.17); the streamwise boundary-layer development is $O(\delta)$ and is assumed to be irrelevant over the wavelength of the disturbance. In this so-called locally-parallel theory, $\bar{u} = \bar{u}(y)$, $\bar{v} = 0$, $\bar{w} = \bar{w}(y)$, $\bar{T} = \bar{T}(y)$ and $\bar{\rho} = 1/\bar{T}(y)$. The continuity equation (1.21) becomes

$$\frac{\partial \tilde{\rho}}{\partial t} + \frac{1}{\bar{T}}\frac{\partial \tilde{u}}{\partial x} + \bar{u}\frac{\partial \tilde{\rho}}{\partial x} - \frac{1}{\bar{T}^2}\frac{\mathrm{d}\bar{T}}{\mathrm{d}y}\tilde{v} + \frac{1}{\bar{T}}\frac{\partial \tilde{v}}{\partial y} + \frac{1}{\bar{T}}\frac{\partial \tilde{w}}{\partial z} + \bar{w}\frac{\partial \tilde{\rho}}{\partial z} = 0. \tag{1.25}$$

The components of the momentum equation (1.22) become

$$\begin{aligned}\frac{1}{\bar{T}}\left[\frac{\partial\tilde{u}}{\partial t}+\bar{u}\frac{\partial\tilde{u}}{\partial x}+\frac{\mathrm{d}\bar{u}}{\mathrm{d}y}\tilde{v}+\bar{w}\frac{\partial\tilde{u}}{\partial z}\right] &= -\frac{\partial\tilde{p}}{\partial x}\\ +\frac{1}{R}\Bigg[\bar{\mu}\left(\frac{\partial^2\tilde{u}}{\partial y^2}+\frac{\partial^2\tilde{u}}{\partial z^2}\right)+\left(\bar{\lambda}+\frac{1}{3}\bar{\mu}\right)\left(\frac{\partial^2\tilde{v}}{\partial x\partial y}+\frac{\partial^2\tilde{w}}{\partial x\partial z}\right)+\left(\bar{\lambda}+\frac{4}{3}\bar{\mu}\right)\frac{\partial^2\tilde{u}}{\partial x^2}\\ +\frac{\mathrm{d}\bar{\mu}}{\mathrm{d}\bar{T}}\frac{\mathrm{d}\bar{T}}{\mathrm{d}y}\left(\frac{\partial\tilde{u}}{\partial y}+\frac{\partial\tilde{v}}{\partial x}\right)+\frac{\mathrm{d}^2\bar{\mu}}{\mathrm{d}\bar{T}^2}\frac{\mathrm{d}\bar{u}}{\mathrm{d}y}\frac{\mathrm{d}\bar{T}}{\mathrm{d}y}\tilde{T}+\frac{\mathrm{d}\bar{u}}{\mathrm{d}y}\frac{\mathrm{d}\bar{\mu}}{\mathrm{d}\bar{T}}\frac{\partial\tilde{T}}{\partial y}+\frac{\mathrm{d}^2\bar{u}}{\mathrm{d}y^2}\frac{\mathrm{d}\bar{\mu}}{\mathrm{d}\bar{T}}\tilde{T}\Bigg],\end{aligned} \tag{1.26}$$

$$\begin{aligned}\frac{1}{\bar{T}}\left[\frac{\partial\tilde{v}}{\partial t}+\bar{u}\frac{\partial\tilde{v}}{\partial x}+\bar{w}\frac{\partial\tilde{v}}{\partial z}\right] &= -\frac{\partial\tilde{p}}{\partial y}+\frac{1}{R}\Bigg[\bar{\mu}\left(\frac{\partial^2\tilde{v}}{\partial x^2}+\frac{\partial^2\tilde{v}}{\partial z^2}\right)\\ &+\left(\bar{\lambda}+\frac{1}{3}\bar{\mu}\right)\left(\frac{\partial^2\tilde{u}}{\partial x\partial y}+\frac{\partial^2\tilde{w}}{\partial y\partial z}\right)+\left(\bar{\lambda}+\frac{4}{3}\bar{\mu}\right)\frac{\partial^2\tilde{v}}{\partial y^2}+\frac{\mathrm{d}\bar{\mu}}{\mathrm{d}\bar{T}}\frac{\mathrm{d}\bar{u}}{\mathrm{d}y}\frac{\partial\tilde{T}}{\partial x}\\ &+2\frac{\mathrm{d}\bar{\mu}}{\mathrm{d}\bar{T}}\frac{\mathrm{d}\bar{T}}{\mathrm{d}y}\frac{\partial\tilde{v}}{\partial y}+\frac{\mathrm{d}\bar{\mu}}{\mathrm{d}\bar{T}}\frac{\mathrm{d}\bar{w}}{\mathrm{d}y}\frac{\partial\tilde{T}}{\partial z}+\left(\frac{\mathrm{d}\bar{\lambda}}{\mathrm{d}\bar{T}}-\frac{2}{3}\frac{\mathrm{d}\bar{\mu}}{\mathrm{d}\bar{T}}\right)\frac{\mathrm{d}\bar{T}}{\mathrm{d}y}\left(\frac{\partial\tilde{u}}{\partial x}+\frac{\partial\tilde{v}}{\partial y}+\frac{\partial\tilde{w}}{\partial z}\right)\Bigg],\end{aligned} \tag{1.27}$$

and

$$\begin{aligned}\frac{1}{\bar{T}}\left[\frac{\partial\tilde{w}}{\partial t}+\bar{u}\frac{\partial\tilde{w}}{\partial x}+\frac{\mathrm{d}\bar{w}}{\mathrm{d}y}\tilde{v}+\bar{w}\frac{\partial\tilde{w}}{\partial z}\right] &= -\frac{\partial\tilde{p}}{\partial z}+\frac{1}{R}\Bigg[\bar{\mu}\left(\frac{\partial^2\tilde{w}}{\partial x^2}+\frac{\partial^2\tilde{w}}{\partial y^2}\right)\\ &+\left(\bar{\lambda}+\frac{1}{3}\bar{\mu}\right)\left(\frac{\partial^2\tilde{u}}{\partial x\partial z}+\frac{\partial^2\tilde{v}}{\partial y\partial z}\right)+\left(\bar{\lambda}+\frac{4}{3}\bar{\mu}\right)\frac{\partial^2\tilde{w}}{\partial z^2}\\ +\frac{\mathrm{d}\bar{\mu}}{\mathrm{d}\bar{T}}\frac{\mathrm{d}\bar{T}}{\mathrm{d}y}\left(\frac{\partial\tilde{v}}{\partial z}+\frac{\partial\tilde{w}}{\partial y}\right)+\frac{\mathrm{d}^2\bar{\mu}}{\mathrm{d}\bar{T}^2}\frac{\mathrm{d}\bar{w}}{\mathrm{d}y}\frac{\mathrm{d}\bar{T}}{\mathrm{d}y}\tilde{T}+\frac{\mathrm{d}\bar{\mu}}{\mathrm{d}\bar{T}}\frac{\mathrm{d}\bar{w}}{\mathrm{d}y}\frac{\partial\tilde{T}}{\partial y}+\frac{\mathrm{d}^2\bar{w}}{\mathrm{d}y^2}\frac{\mathrm{d}\bar{\mu}}{\mathrm{d}\bar{T}}\tilde{T}\Bigg].\end{aligned} \tag{1.28}$$

The energy equation (1.23) and equation of state (1.24) become

$$\begin{aligned}\frac{1}{\bar{T}}\left[\frac{\partial\tilde{T}}{\partial t}+\bar{u}\frac{\partial\tilde{T}}{\partial x}+\frac{\mathrm{d}\bar{T}}{\mathrm{d}y}\tilde{v}+\bar{w}\frac{\partial\tilde{T}}{\partial z}\right] &= (\gamma-1)\,M^2\left[\frac{\partial\tilde{p}}{\partial t}+\bar{u}\frac{\partial\tilde{p}}{\partial x}+\bar{w}\frac{\partial\tilde{p}}{\partial z}\right]\\ +\frac{1}{RPr}\Bigg[\bar{\mu}\frac{\partial^2\tilde{T}}{\partial x^2}+\frac{\mathrm{d}\bar{\mu}}{\mathrm{d}\bar{T}}\frac{\partial\tilde{T}}{\partial y}+\bar{\mu}\frac{\partial^2\tilde{T}}{\partial y^2}+\frac{\mathrm{d}^2\bar{\mu}}{\mathrm{d}\bar{T}^2}\frac{\mathrm{d}\bar{T}}{\mathrm{d}y}^2\tilde{T}+\frac{\mathrm{d}\bar{\mu}}{\mathrm{d}\bar{T}}\frac{\mathrm{d}\bar{T}}{\mathrm{d}y}\frac{\partial\tilde{T}}{\partial y}\\ +\frac{\mathrm{d}\bar{\mu}}{\mathrm{d}\bar{T}}\frac{\mathrm{d}^2\bar{T}}{\mathrm{d}y^2}\tilde{T}+\bar{\mu}\frac{\partial^2\tilde{T}}{\partial z^2}\Bigg]+\frac{(\gamma-1)\,M^2}{R}\left[\frac{\mathrm{d}\bar{\mu}}{\mathrm{d}\bar{T}}\frac{\mathrm{d}\bar{u}}{\mathrm{d}y}^2\tilde{T}+\frac{\mathrm{d}\bar{\mu}}{\mathrm{d}\bar{T}}\frac{\mathrm{d}\bar{w}}{\mathrm{d}y}^2\tilde{T}\right]\end{aligned} \tag{1.29}$$

and

$$\tilde{\rho}=\frac{\gamma M^2}{\bar{T}}\tilde{p}-\frac{1}{\bar{T}^2}\tilde{T}. \tag{1.30}$$

The state equation (1.30) is used to eliminate $\tilde{\rho}$ from the equations. Noting the parallel-flow assumption the disturbance variables can be decomposed into the

harmonic form, for example with $\tilde{u}$

$$\tilde{u}(x,y,z,t) = \hat{u}(y)\exp\left[i\left(\alpha x + \zeta z - \omega t\right)\right]. \tag{1.31}$$

This transforms the linearised stability equations (1.25)-(1.29) to ordinary differential equations in y. With $D \equiv \mathrm{d}/\mathrm{d}y$, and dividing each equation by the exponential term $\exp\left[i\left(\alpha x - \zeta z - \omega t\right)\right]$,

$$\begin{aligned} D\hat{v} = \hat{u}\left[-i\alpha\right] + \hat{v}\left[\frac{D\bar{T}}{\bar{T}}\right] + \hat{p}\left[-i\gamma M^2\left(\alpha\bar{u} + \zeta\bar{w} - \omega\right)\right] \\ + \hat{T}\left[\frac{i\left(\alpha\bar{u} + \zeta\bar{w} - \omega\right)}{\bar{T}}\right] + \hat{w}\left[-i\zeta\right], \end{aligned} \tag{1.32}$$

$$\begin{aligned} &\hat{u}\left[\frac{i\left(\alpha\bar{u} + \zeta\bar{w} - \omega\right)}{\bar{T}} + \frac{\left(\alpha^2 + \zeta^2\right)\bar{\mu}}{R} + \frac{\alpha^2\left(\bar{\lambda} + \frac{1}{3}\bar{\mu}\right)}{R}\right] + D\hat{u}\left[-\frac{\bar{\mu}' D\bar{T}}{R}\right] \\ &+ D^2\hat{u}\left[-\frac{\bar{\mu}}{R}\right] + \hat{v}\left[\frac{D\bar{u}}{\bar{T}} - \frac{i\alpha\bar{\mu}' D\bar{T}}{R}\right] + D\hat{v}\left[-\frac{i\alpha\left(\bar{\lambda} + \frac{1}{3}\bar{\mu}\right)}{R}\right] + \hat{p}\left[i\alpha\right] \\ &+ \hat{T}\left[-\frac{\bar{\mu}'' D\bar{u} D\bar{T} + \bar{\mu}' D^2\bar{u}}{R}\right] + D\hat{T}\left[-\frac{\bar{\mu}' D\bar{u}}{R}\right] + \hat{w}\left[\frac{\alpha\zeta\left(\bar{\lambda} + \frac{1}{3}\bar{\mu}\right)}{R}\right] = 0, \end{aligned} \tag{1.33}$$

$$\begin{aligned} &\hat{u}\left[-\frac{i\alpha D\bar{T}\left(\bar{\lambda}' + \frac{1}{3}\bar{\mu}'\right)}{R}\right] + D\hat{u}\left[-\frac{i\alpha\left(\bar{\lambda} + \frac{1}{3}\bar{\mu}\right)}{R}\right] \\ &+ \hat{v}\left[\frac{i\left(\alpha\bar{u} + \zeta\bar{w} - \omega\right)}{\bar{T}} + \frac{\left(\alpha^2 + \zeta^2\right)\bar{\mu}}{R}\right] + D\hat{v}\left[-\frac{\left(\bar{\lambda}' + \frac{4}{3}\bar{\mu}'\right) D\bar{T}}{R}\right] \\ &+ D^2\hat{v}\left[-\frac{\left(\bar{\lambda} + \frac{4}{3}\bar{\mu}\right)}{R}\right] + D\hat{p} + \hat{T}\left[-\frac{i\bar{\mu}'\left(\alpha\bar{u} + \zeta\bar{w}\right)}{R}\right] \\ &+ \hat{w}\left[-\frac{i\zeta\left(\bar{\lambda}' - \frac{2}{3}\bar{\mu}'\right)}{R}\right] + D\hat{w}\left[-\frac{i\zeta\left(\bar{\lambda} + \frac{1}{3}\bar{\mu}\right)}{R}\right] = 0, \end{aligned} \tag{1.34}$$

$$\begin{aligned} &\hat{u}\left[\frac{\alpha\zeta\left(\bar{\lambda} + \frac{1}{3}\bar{\mu}\right)}{R}\right] + \hat{v}\left[\frac{D\bar{w}}{\bar{T}} - \frac{i\zeta\bar{\mu}' D\bar{T}}{R}\right] + D\hat{v}\left[-\frac{i\zeta\left(\bar{\lambda} + \frac{1}{3}\bar{\mu}\right)}{R}\right] \\ &+ \hat{p}\left[i\zeta\right] + \hat{T}\left[-\frac{\bar{\mu}'' D\bar{w} D\bar{T} + \bar{\mu}' D^2\bar{w}}{R}\right] + D\hat{T}\left[-\frac{\bar{\mu}' D\bar{w}}{R}\right] \\ &+ \hat{w}\left[\frac{i\left(\alpha\bar{u} - \zeta\bar{w} - \omega\right)}{\bar{T}} + \frac{\left(\alpha^2 + \zeta^2\right)\bar{\mu}}{R} + \frac{\zeta^2\left(\bar{\lambda} + \frac{1}{3}\bar{\mu}\right)}{R}\right] \\ &+ D\hat{w}\left[-\frac{\bar{\mu}' D\bar{T}}{R}\right] + D^2\hat{w}\left[-\frac{\bar{\mu}}{R}\right] = 0, \end{aligned} \tag{1.35}$$

$$
\begin{aligned}
&\hat{v}\left[\frac{D\bar{T}}{\bar{T}}\right]+\hat{p}\left[-i\left(\gamma-1\right)M^{2}\left(\alpha\bar{u}+\zeta\bar{w}-\omega\right)\right]\\
&+\hat{T}\left[\frac{i\left(\alpha\bar{u}+\zeta\bar{w}-\omega\right)}{\bar{T}}+\frac{\bar{\mu}\left(\alpha^{2}+\zeta^{2}\right)}{RPr}-\frac{\bar{\mu}''D\bar{T}^{2}+\bar{\mu}'D^{2}\bar{T}}{RPr}\right.\\
&\left.-\frac{\left(\gamma-1\right)M^{2}\bar{\mu}'\left(D\bar{u}^{2}+D\bar{w}^{2}\right)}{R}\right]+D\hat{T}\left[\frac{2\bar{\mu}'D\bar{T}}{RPr}\right]+D^{2}\hat{T}\left[\frac{\bar{\mu}}{RPr}\right]=0.
\end{aligned}
\tag{1.36}
$$

Now $D\hat{v}$ can be eliminated using (1.32), and $D^2\hat{v}$ by differentiating (1.32) by y. The equations (1.32)-(1.36) thus make up an 8th order system of equations for the variable vector $\mathbf{q}$; with components $q_1 = \hat{u}$, $q_2 = D\hat{u}$, $q_3 = \hat{v}$, $q_4 = \hat{p}$, $q_5 = \hat{T}$, $q_6 = D\hat{T}$, $q_7 = \hat{w}$, $q_8 = D\hat{w}$; and

$$
D\mathbf{q} = A\mathbf{q}. \tag{1.37}
$$

The first row of this system is an identity for q_2, so

$$
a_{12} = 1 \tag{1.38}
$$

is the only non-zero entry on this row. The second row is given by equation (1.33), with non-zero entries

$$
\begin{aligned}
a_{21} &= iR\frac{\bar{K}}{\bar{\mu}\bar{T}}+\alpha^{2}+\zeta^{2},\\
a_{22} &= -\frac{\bar{\mu}'D\bar{T}}{\bar{\mu}},\\
a_{23} &= R\frac{D\bar{u}}{\bar{\mu}\bar{T}}-i\alpha\frac{\bar{\mu}'\bar{T}}{\bar{\mu}}-i\alpha J_{1}\frac{D\bar{T}}{\bar{T}},\\
a_{24} &= \frac{i\alpha R}{\bar{\mu}}-\alpha\gamma M^{2}J_{1}\bar{K},\\
a_{25} &= i\alpha J_{1}\frac{\bar{K}}{\bar{T}}-\frac{\bar{\mu}''D\bar{u}D\bar{T}+\bar{\mu}'D^{2}\bar{u}}{\bar{\mu}},\\
a_{26} &= -\frac{D\bar{u}\bar{\mu}'}{\bar{\mu}},
\end{aligned}
\tag{1.39}
$$

where $\bar{K} = \alpha\bar{u} + \zeta\bar{w} - \omega$ and $J_n = \bar{\lambda}/\bar{\mu} + n/3$. The third row is from equation

(1.32), with non-zero entries

$$
\begin{aligned}
a_{31} &= -i\alpha, \\
a_{33} &= \frac{D\bar{T}}{\bar{T}}, \\
a_{34} &= -i\gamma M^2 \bar{K}, \\
a_{35} &= i\frac{\bar{K}}{\bar{T}}, \\
a_{37} &= -i\zeta.
\end{aligned}
\tag{1.40}
$$

The fourth row is from equation (1.34), with

$$
\begin{aligned}
a_{41} &= -i\alpha\chi\left(2\frac{\bar{\mu}' D\bar{T}}{\bar{\mu}} + J_2\frac{D\bar{T}}{\bar{T}}\right), \\
a_{42} &= -i\alpha\chi, \\
a_{43} &= \chi\left[-iR\frac{\bar{K}}{\bar{\mu}\bar{T}} + \alpha^2 + \zeta^2 + J_2\left(\frac{\bar{\mu}' D\bar{T}^2 + D^2\bar{T}}{\bar{T}}\right)\right], \\
a_{44} &= -i\gamma M^2 \chi J_2\left[D\bar{K} + \bar{K}\left(\frac{\bar{\mu}' D\bar{T}}{\bar{\mu}} + \frac{D\bar{T}}{\bar{T}}\right)\right], \\
a_{45} &= i\chi\left[D\bar{K}\left(\frac{J_2}{\bar{T}} + \frac{\bar{\mu}'}{\bar{T}}\right) + \bar{K}\frac{J_2\bar{\mu}' D\bar{T}}{\bar{\mu}\bar{T}}\right], \\
a_{46} &= i\chi\frac{J_2\bar{K}}{\bar{T}}, \\
a_{47} &= -i\zeta\chi\left(\frac{2\bar{\mu}' D\bar{T}}{\bar{\mu}} + J_2\frac{D\bar{T}}{\bar{T}}\right), \\
a_{48} &= -i\zeta\chi,
\end{aligned}
\tag{1.41}
$$

where $\chi = \left(R/\bar{\mu} + i\gamma M^2 J_2 \bar{K}\right)^{-1}$. The fifth row is an identity for q_6, so

$$
a_{56} = 1 \tag{1.42}
$$

is the only non-zero entry in this row. The sixth row is from equation (1.36), with

non-zero entries

$$
\begin{aligned}
a_{62} &= -2\left(\gamma-1\right)M^2 Pr D\bar{u},\\
a_{63} &= -2i\left(\gamma-1\right)M^2 Pr D\bar{K} + PrR\frac{D\bar{T}}{\bar{\mu}\bar{T}},\\
a_{64} &= -i\left(\gamma-1\right)M^2 PrR\frac{\bar{K}}{\bar{\mu}},\\
a_{65} &= iPrR\frac{\bar{K}}{\bar{\mu}\bar{T}} + \alpha^2 + \zeta^2 + \left(\gamma-1\right)M^2 Pr\frac{\bar{\mu}'\left(D\bar{u}^2 + D\bar{w}^2\right)}{\bar{\mu}} - \frac{\bar{\mu}''}{\bar{\mu}},\\
a_{66} &= -\frac{2\bar{\mu}'}{\bar{\mu}},\\
a_{68} &= -2\left(\gamma-1\right)M^2 Pr D\bar{w}.
\end{aligned}
\tag{1.43}
$$

The seventh row is an identity for q_8, so

$$a_{78} = 1 \tag{1.44}$$

is the only non-zero entry in that row, and finally the eighth row is from equation (1.35), with non-zero entries

$$
\begin{aligned}
a_{83} &= -i\zeta\left(\frac{\bar{\mu}' D\bar{T}}{\bar{\mu}} - J_1\frac{D\bar{T}}{\bar{T}}\right) - R\frac{D\bar{w}}{\bar{\mu}\bar{T}},\\
a_{84} &= \zeta\left(\frac{iR}{\bar{\mu}} - J_1\gamma M^2\bar{K}\right),\\
a_{85} &= \zeta J_1\frac{\bar{K}}{\bar{T}} - \frac{\bar{\mu}' D^2\bar{w}}{\bar{\mu}} - \frac{\bar{\mu}'' D\bar{T} D\bar{w}}{\bar{\mu}},\\
a_{86} &= -\frac{\bar{\mu}' D\bar{w}}{\bar{\mu}},\\
a_{87} &= iR\frac{\bar{K}}{\bar{\mu}\bar{T}} + \alpha^2 + \zeta^2,\\
a_{88} &= -\frac{\bar{\mu}'\bar{T}}{\bar{\mu}}.
\end{aligned}
\tag{1.45}
$$

1.3.1 Boundary Conditions

To close the stability equations, eight boundary conditions are required. Applying the no-slip condition gives three of these

$$q_1(0) = q_3(0) = q_7(0) = 0 \tag{1.46}$$

and a condition for the temperature perturbation is also specified at the wall;

$$\text{either} \begin{cases} q_5(0) = 0 \\ q_6(0) = 0, \end{cases} \tag{1.47}$$

is suitable Reed and Balakumar (1990). The last four conditions are chosen on the assumption that the disturbance is small and constrained within the confines of the boundary layer. Hence the far-field boundary conditions are taken as

$$q_1,\ q_3,\ q_5,\ q_7 \text{ are bounded as } y \to \infty. \tag{1.48}$$

1.3.2 Eigenvalue Problem

The equations are now closed and constitute an eigenvalue problem for the wave parameters α, ζ and ω. In the general eigenvalue problem, these parameters may all be complex with the imaginary parts corresponding to exponential growth or decay of the disturbance. The order of the equations makes solving the general problem extremely difficult.

Instead of attempting the general problem, two different stability problems may be considered. If the wavenumbers α and ζ are taken to be complex and the frequency ω real, the disturbance only grows in space. This is referred to as the spatial stability problem. Conversely the temporal stability problem has the frequency taken to be complex and the wavenumbers real.

A spatial stability analysis is desirable from a transition-prediction standpoint; these results can be integrated along a surface to determine spatial amplification rates, which are empirically linked with boundary-layer transition (Smith and Gamberoni, 1956, Van Ingen, 1956). However the spatial eigenvalue(s) are non-linear and the equations are more difficult to solve numerically.

A temporal stability analysis is much more amenable to analytical and numerical methods owing to the temporal eigenvalues being linear. Early work in boundary-layer stability exclusively considered temporal stability, however as the practicality of spatial stability was understood, a method for using the easier-to-obtain temporal eigenvalues to approximate spatial results was developed by Gaster (1962) for disturbances with small amplification rates.

The work presented focusses on the temporal stability analysis in order to compare with the more rigorous theoretical results available. A spatial analysis, along with determining amplification rates is left as possible future work.

1.3.3 Two-Dimensional Problem and Orientation

If there is no spanwise velocity ($\bar{w} \equiv 0$) and disturbance propagation ($\zeta = 0$), the equations for q_7 and q_8 may be solved independently with the boundary conditions on q_7 and the stability problem is reduced to sixth order. However, even when the boundary layer is two-dimensional, oblique disturbances are still relevant and in some cases are the most unstable (Mack, 1969).

It is more natural, especially for the temporal problem, to consider a rotation such that the stability equations resemble the two-dimensional problem. Taking

$$\bar{\alpha}\bar{u}_k = \alpha\bar{u} + \zeta\bar{w}, \tag{1.49}$$

where $\bar{\alpha}^2 = \alpha^2 + \zeta^2$ is the wavenumber magnitude and $\bar{u}_k$ is the boundary-layer velocity profile parallel to the disturbance, then

$$\bar{K} = \bar{\alpha}\left(\bar{u_k} - c\right), \tag{1.50}$$

where $c = \omega/\bar{\alpha}$ is the wave speed.

1.3.4 Inviscid Stability Analysis

Compressible, flat-plate boundary layers are inviscidly unstable, that is, the largest growth rates occur in the limit of $R \to \infty$. The stability in this limit may be physically interpreted as the stability of the boundary layer at a large streamwise distance along the surface.

In this singular limit, equations (1.33)-(1.36) become

$$\hat{u}\left[\frac{i\bar{K}}{\bar{T}}\right] + \hat{v}\left[\frac{D\bar{u}}{\bar{T}}\right] + \hat{p}\left[i\alpha\right] = 0, \tag{1.51}$$

$$\hat{v}\left[\frac{i\bar{K}}{\bar{T}}\right] + D\hat{p} = 0, \tag{1.52}$$

$$\hat{v}\left[\frac{D\bar{w}}{\bar{T}}\right] + \hat{p}\left[i\zeta\right] + \hat{w}\left[\frac{i\bar{K}}{\bar{T}}\right] = 0, \tag{1.53}$$

$$\hat{v}\left[\frac{D\bar{T}}{\bar{T}}\right] + \hat{p}\left[-i\left(\gamma - 1\right)M^2\bar{K}\right] + \hat{T}\left[\frac{i\bar{K}}{\bar{T}}\right] = 0, \tag{1.54}$$

which give explicit forms for $\hat{u}$, $\hat{w}$ and $\hat{T}$ in terms of $\hat{v}$ and $\hat{p}$. Using these, along with equation (1.32) yields

$$D\hat{v} = \hat{v}\left[\frac{D\bar{K}}{\bar{K}}\right] + \hat{p}\left[\frac{i\bar{T}}{\bar{K}}\left(\alpha^2 + \zeta^2\right) - iM^2\bar{K}\right], \tag{1.55}$$

$$D\hat{p} = \hat{v}\left[-\frac{i\bar{K}}{\bar{T}}\right], \tag{1.56}$$

or in terms of the rotated view

$$D\hat{v}\left[\bar{u}_k - c\right] = \hat{v}\left[D\bar{u}_k\right] + \hat{p}\left[i\bar{\alpha}\left(\bar{T} - M^2\left(\bar{u}_k - c\right)^2\right)\right], \tag{1.57}$$

$$D\hat{p} = \hat{v}\left[\frac{-i\bar{\alpha}\left(\bar{u}_k - c\right)}{\bar{T}}\right]. \tag{1.58}$$

In the inviscid limit the stability problem is reduced to second order, even for the three-dimensional problem. The boundary conditions on $\hat{v}$ of no-slip and far-field boundedness are retained. After a solution is obtained, the other disturbance amplitudes may be determined with

$$\hat{u} = \hat{v}\left[\frac{iD\bar{u}}{\bar{\alpha}\left(\bar{u}_k - c\right)}\right] + \hat{p}\left[-\frac{\alpha\bar{T}}{\bar{\alpha}\left(\bar{u}_k - c\right)}\right], \tag{1.59}$$

$$\hat{w} = \hat{v}\left[\frac{iD\bar{w}}{\bar{\alpha}\left(\bar{u}_k - c\right)}\right] + \hat{p}\left[-\frac{\zeta\bar{T}}{\bar{\alpha}\left(\bar{u}_k - c\right)}\right], \tag{1.60}$$

$$\hat{T} = \hat{v}\left[\frac{iD\bar{T}}{\bar{\alpha}\left(\bar{u}_k - c\right)}\right] + \hat{p}\left[\left(\gamma - 1\right)M^2\bar{T}\right]. \tag{1.61}$$

As an alternative, the stability problem may be written as a single second-order equation in terms of either $\hat{v}$

$$D\left[\frac{\left(\bar{u}_k - c\right)D\hat{v} - D\bar{u}_k\hat{v}}{\bar{T} - M^2\left(\bar{u}_k - c\right)^2}\right] = \tilde{\alpha}^2\frac{\bar{u}_k - c}{\bar{T}}\hat{v}, \tag{1.62}$$

or $\hat{p}$

$$D^2\hat{p} - \frac{2D\bar{u}_k}{\bar{u}_k - c}D\hat{p} - \tilde{\alpha}^2\bar{T}\left(\bar{T} - \left(\bar{u}_k - c\right)^2 M^2\right)\hat{p} = 0. \tag{1.63}$$

In the far-field, i.e. as $y \to \infty$, the boundary-layer velocity and temperature approach 1 and (1.63) becomes

$$D^2\hat{p}_\infty - \tilde{\alpha}^2\left(1 - \left(1 - c\right)^2 M^2\right)\hat{p}_\infty = 0, \tag{1.64}$$

which may be integrated twice to give

$$\hat{p}_\infty \sim \exp\left[\pm\left(\tilde{\alpha}\sqrt{1-(1-c)^2 M^2}\right) y\right], \tag{1.65}$$

and using (1.58) the far-field condition for $\hat{v}$ is

$$\hat{v}_\infty = \pm\frac{i\sqrt{1-(1-c)^2 M^2}}{1-c}\hat{p}_\infty. \tag{1.66}$$

Therefore, in order to have a bounded solution, the exponentially growing solution must be discarded and for a neutral mode ($\Im(c) = 0$) with

$$1-(1-c)^2 M^2 > 0,$$

or

$$1-\frac{1}{M} < c < 1+\frac{1}{M}, \tag{1.67}$$

these are termed by Lees and Lin (1946) as *subsonic* modes, as "the phase velocity of the wavy disturbance in the direction of the freestream and relative to an observer moving with the velocity of the freestream, is below the local velocity of sound." Neutral disturbances outside this range are consequently *supersonic* modes.

Mack (1969) considered the inviscid equations with consideration of the relative Mach number between the disturbance and base flow

$$\bar{M} = \frac{\bar{u}_k - c}{\bar{T}^{1/2}} M. \tag{1.68}$$

When there is a region in the domain where $\bar{M} > 1$, the inviscid equations are hyperbolic (as opposed to elliptic) and there are infinitely many eigenmode solutions for a given wavenumber.

For a neutral mode, it is possible that there is a location in the domain where $\bar{u}_k = c$ and the inviscid equations are singular. Lees and Lin (1946) determined that the singularity at this point was logarithmic in nature and is removable if

$$D\left(\frac{D\bar{u}_k}{\bar{T}}\right) = 0, \tag{1.69}$$

and such points in the boundary layer are called *generalised points of inflection.* This is so named for being analogous to the incompressible theory where the condition is $D^2\bar{u}_k = 0$. Lees and Lin (1946) also showed that if such a point exists in a boundary layer where the disturbance will be subsonic, it is a sufficient condition

for the existence of an unstable wave. Finally, Lees and Lin (1946) also proved the existence of a sonic neutral mode at $\alpha = 0$, $c = 1 - 1/M$.

The inviscid theory is more important for compressible flows as inviscid disturbances are often dominant. For an incompressible, flat-plate boundary layer (Blasius flow) there are no inflection points and there is no inviscid instability. In contrast, a compressible flat-plate boundary layer does contain a (generalised) point of inflection and hence an inviscid instability.

1.3.5 The Critical Layer

The inviscid singularity at locations where $\bar{u}_k = c$ manifests as a critical layer structure in the viscous equations for high R. Lees and Lin (1946) performed a local analysis to determine the structure of this critical layer in terms of a convergent series in powers of $1/\alpha R$, which is taken to be a small parameter. They also considered a WKB-type solution and its connection with the critical layer to analyse the global structure. The importance of this work is in the comparison between this analysis and the inviscid solutions; the physically valid inviscid solutions are those to which the viscous solutions converge. The critical layer is examined in more detail in Chapter 5.1.

1.3.6 Presentation and Interpretation of Stability Analysis

The presentation of compressible stability analysis results is challenging because of the number of parameters involved. A common thread is the focus on neutral disturbances that demarcate the region of instability, the locus of which make up a neutral curve.

The calculation of a neutral curve is especially important for determining the critical Reynolds number; that is the minimum Reynolds number (analogous to streamwise distance) for which there are unstable solutions. This becomes important when determining amplification rates for transition prediction.

The e^N transition prediction method of Smith and Gamberoni (1956) and Van Ingen (1956) uses linear stability results to predict if and when transition will occur. For a wave of constant frequency, the amplitude ratio is calculated by integrating

the constant-frequency (spatial) growth rate with respect to the Reynolds number from the first point of neutral stability. The location where the amplitude ratio reaches a certain value of e^N (often $N = 9$) correlates well with the location of transition. Without knowledge of the receptivity of the boundary-layer to external disturbances, which determines the initial amplitude of the disturbance, this method is empirical and its use must be carefully considered (Reed and Saric, 1996). This method is made more complicated by considering accelerated boundary layers given that the non-dimensional frequency becomes variable with R (Mack, 1984).

Analysis of neutral modes and their nature can bring insight into the physical mechanisms underpinning the propagation of the disturbance. An understanding of these mechanisms at a fundamental level can be useful for developing transition control techniques. A key example of this application is the design of porous coatings for aerodynamic surfaces to absorb energy from unstable acoustic disturbances (Fedorov et al., 2001).

1.4 Thesis Outline

The work presented aims to fill a gap in the literature regarding the stability of compressible boundary layers with velocity overshoot. Many publications have considered the stability of boundary layers with a heated surface and a favourable pressure gradient separately, with results covered in the numerous review papers (i.e. Reed and Saric, 1996). However, none have considered the special case where velocity overshoot occurs.

In Chapter 2, the boundary-layer equations that serve as a base flow for the subsequent stability analysis are discussed in greater detail. Conditions for a similarity solution, the far-field behaviour, numerical solution and general properties of overshoot boundary layers are discussed. The observation of multiple generalised points of inflection and the variable value of the velocity maximum are highlighted and are of key importance to, and motivation for, the stability analysis. As an addendum, the nature of the hypersonic overshoot boundary layer is analytically explored.

In Chapter 3, numerical results from the inviscid stability analysis on overshoot boundary layers are presented. The methodology is explored taking heed of the challenges involved in such an analysis. The results identify a new unstable mode that exists alongside the traditional Mack modes that is intimately connected with the existence of a velocity maximum in the boundary layer. The structure of the new mode within the parameter space is considered.

In Chapter 4, the nature of the new mode is analysed and its existence in the low wavenumber limit is confirmed through an asymptotic analysis. The non-zero wavenumber neutral disturbance associated with the new mode is discussed qualitatively, along with the nature of the new mode's interaction with the Mack modes. Oblique disturbances are considered and the effect of the wave angle on the new mode is investigated.

In Chapter 5, the stability analysis is extended to include viscous effects. The high Reynolds number limit of the viscous stability equations are analysed with consideration for overshoot boundary layers. Numerical results are presented for curves of neutral stability and the nearly-inviscid neutral modes are discussed. Finally, in Chapter 6, the key findings of the thesis are summarised.

Chapter 2

Compressible Boundary-Layer Theory

In this chapter, the boundary-layer equations (1.16) and (1.17) are further analysed. Under idealised conditions these equations permit a self-similar solution that transforms them into ordinary differential equations, useful for the subsequent stability analysis. These conditions are determined and discussed.

Following this the focus is on the behaviour of solutions relating to a boundary layer over a heated surface, which is influenced by a favourable pressure gradient. The existence of a velocity overshoot produced by such a system is demonstrated by considering the far-field asymptotic structure of the solutions.

While analytical progress can be made in some specific cases, it is necessary to be able to numerically solve the boundary-layer equations with a high degree of accuracy for the subsequent stability analysis (Malik, 1990). Techniques for solving these stiff, non-linear equations are explored in this chapter and solutions are presented along with the properties of the boundary layer relevant to the stability analysis. Of particular importance here are the generalised points of inflection, defined in (1.69), that directly affect the inviscid stability. Overshoot boundary layers have additional generalised points of inflection and their evolution within the parameter space, particularly as a function of the Mach number, is explored and highlighted.

Finally, the structure of solutions to the boundary-layer equations are analysed

in the high Mach number (hypersonic) limit. Here the boundary layer develops a thin slip region at the wall with a thickness that depends on the viscosity-temperature law chosen. The analysis will demonstrate that there is a finite ultimate velocity maximum that overshoot boundary layers may attain in this high Mach number limit.

2.1 Conditions for Similar Solution

We attempt to reduce the dimensional boundary-layer equations (1.16) and (1.17) to ordinary differential equations by finding a similarity solution. The independent variables x and Y are transformed to the variables $\xi = \xi(x)$ and $\eta = \eta(x, Y)$, and these will be defined later. Functions Ω, f and g are introduced and defined according to

$$\psi(x, Y) = \Omega(x) f(\xi, \eta),$$
$$u(x, y) = u_e(x) \frac{\partial f}{\partial \eta}(\xi, \eta),$$
$$H(x, y) = H_e g(\xi, \eta),$$

where the subscript e refers to the edge of the boundary layer. The streamwise edge velocity is variable to allow variations due to pressure gradients and the total enthalpy is assumed to be constant at the edge. Now, from the definition of the stream function, equation (1.14),

$$\rho u = \frac{\partial \psi}{\partial Y}$$
$$\rho u_e \frac{\partial f}{\partial \eta} = \Omega \frac{\partial f}{\partial \eta} \frac{\partial \eta}{\partial Y}$$
$$\frac{\partial \eta}{\partial Y} = \frac{\rho u_e}{\Omega},$$

so the variable η is defined as

$$\eta = \frac{u_e(x)}{\Omega(x)} \int_0^Y \rho(Y) \mathrm{d}Y. \tag{2.1}$$

With these transformations, the momentum equation (1.16) becomes

$$(\rho \mu f_{\eta\eta})_\eta + \frac{\Omega \Omega'}{u_e} f f_{\eta\eta} + \frac{u_e' \Omega^2}{u_e^2} f_\eta^2 + \frac{\Omega^2}{\rho u_e^3} \frac{\mathrm{d}p}{\mathrm{d}x} = \frac{\Omega^2}{u_e} \xi' \left(f_\xi f_{\eta\eta} - f_{\xi\eta} f_\eta \right), \tag{2.2}$$

and the energy equation (1.17) becomes

$$\frac{1}{Pr}\left(\rho\mu g_\eta\right)_\eta + \left(1-\frac{1}{Pr}\right)\frac{u_e^2}{H_e}\left(\rho\mu f_\eta f_{\eta\eta}\right)_\eta + \frac{\Omega'\Omega}{u_e} f g_\eta = \frac{\Omega^2}{u_e}\xi'\left(f_\eta g_\xi - f_\xi g_\eta\right), \quad (2.3)$$

where primes denote differentiation with respect to x and subscripts ξ and η refer to partial differentiation with respect to ξ and η respectively. The boundary conditions are now

$$f = f_\eta = 0,\ g = g_w \text{ or } g_\eta = 0 \text{ at } \eta = 0,$$

$$f_\eta \to 1,\ g \to 1 \text{ as } \eta \to \infty.$$

The boundary conditions on g at the surface reflect either the choice of a fixed wall enthalpy or an insulated wall.

2.1.1 Viscosity-Temperature Law

The (dynamic) viscosity of a fluid is a function of its temperature and pressure. With pressure being constant in the boundary layer, the viscosity can then be taken to be a function of temperature only. The relationship between viscosity and temperature for a given fluid is determined experimentally and an empirical model is then used to represent the true relationship. We use

$$\frac{\mu}{T} = C\frac{\mu_e}{T_e},$$

where $C = C(T)$ depends on the model chosen.

The simplest model is the Chapman (or Chapman-Rubesin) Law (Chapman and Rubesin, 1949), which simply takes C to be unity. This model presents as an attractive choice for analysis, however there is uncertainty over the accuracy of quantitative results, and there may be major qualitative differences due to physical phenomena left unsimulated. The Chapman Law model is generally considered sufficiently accurate over small temperature ranges. However, for a compressible, heated-surface boundary layer large temperature ranges are expected, so this model is limited to qualitative analysis only.

The semi-empirical model of Sutherland (1893) is derived from the molecular theory of gases and is more accurate than the linear Chapman Law over a larger

range of temperatures. The Sutherland model gives

$$C = \frac{T+S}{1+S} T^{1/2}, \tag{2.4}$$

where S is the "Sutherland temperature", a value that depends on the chosen fluid and the free-stream temperature. For air a suitable value is $110K$ (Stewartson, 1964) and this value is used throughout this thesis. Malik (1990) uses a similar value of $198.6°R$.

From the equation of state (1.4):

$$T = \frac{p}{R_g \rho}$$

and

$$T_e = \frac{p_e}{R_g \rho_e}.$$

However, since p is constant in the boundary layer, the viscosity-temperature law gives

$$\rho\mu = C\rho_e\mu_e.$$

We now suppose that η is a similarity variable and f and g are functions of η only. The right-hand sides of equations (2.2) and (2.3) are then zero and these equations become

$$(Cf_{\eta\eta})_\eta + \frac{\Omega\Omega'}{\rho_e\mu_e u_e} f f_{\eta\eta} + \frac{u_e'\Omega^2}{\rho_e\mu_e u_e^2}\left(\frac{\rho_e}{\rho} - f_\eta^2\right) = 0, \tag{2.5}$$

$$\frac{1}{Pr}(Cg_\eta)_\eta + \left(1 - \frac{1}{Pr}\right)\frac{u_e^2}{H_e}(Cf_\eta f_{\eta\eta})_\eta + \frac{\Omega'\Omega}{\rho_e\mu_e u_e} f g_\eta = 0, \tag{2.6}$$

where the pressure term in (2.2) has been eliminated by using the value of the velocity in the far-field. In order for the similarity solution to be valid, all components must be at most a function of η. In preparation for this, the equation of state gives

$$\frac{\rho_e}{\rho} = \frac{T}{T_e},$$

or in terms of the internal energy $h = c_p T$ and total enthalpy $H = c_p T + u^2/2$,

$$\frac{\rho_e}{\rho} = \frac{H - \frac{u^2}{2}}{H_e - \frac{u_e^2 f_\eta^2}{2}}.$$

Alternatively, in terms of the similarity variables

$$\frac{\rho_e}{\rho} = \frac{g - \frac{u_e^2}{2H_e} f_\eta^2}{1 - \frac{u_e^2}{2H_e}},$$

which can be written as

$$\frac{\rho_e}{\rho} - f_\eta^2 = \frac{H_e}{H_e - \frac{1}{2}u_e^2}\left(g - f_\eta^2\right) = \frac{H_e}{h_e}\left(g - f_\eta^2\right). \tag{2.7}$$

2.1.2 The First Similarity Condition

In considering equation (2.5), it is observed that for similarity the coefficient

$$\frac{\Omega\Omega'}{\rho_e \mu_e u_e}$$

must be independent of ξ, and must therefore be a constant. This can be set to unity without loss of generality and then

$$\left(\Omega^2\right)' = 2\rho_e \mu_e u_e,$$

hence

$$\Omega^2 = 2\int_0^x \rho_e \mu_e u_e \,\mathrm{d}x.$$

Defining

$$\xi(x) = \int_0^x \rho_e \mu_e u_e \,\mathrm{d}x$$

then

$$\eta(x, Y) = \frac{u_e}{\sqrt{2\xi}} \int_0^Y \rho(Y)\mathrm{d}Y. \tag{2.8}$$

With this definition for η the first similarity condition is thus satisfied. The original transformation of this nature is due to Illingworth (1950), but is often referred to as the Mangler-Levy-Lees (i.e. in Malik, 1990) transformation, which is more generalised.

2.1.3 The Second Similarity Condition

Now, the nature of the coefficient

$$\frac{u_e^2}{H_e},$$

appearing in equation (2.6) is considered. From (1.5) and (1.6)

$$c_p = \frac{R_g \gamma}{\gamma - 1},$$

and for an ideal gas

$$a_e = \sqrt{R_g \gamma T_e},$$

so

$$h_e = c_p T_e = \frac{u_e^2}{(\gamma - 1) M^2}$$

and

$$\frac{u_e^2}{H_e} = \frac{u_e^2}{h_e + \frac{1}{2} u_e^2} = \frac{2k}{1+k},$$

where

$$k = \frac{u_e^2}{2h_e} = \frac{\gamma - 1}{2} M^2.$$

Hence for this similarity condition to be satisfied, both γ and M must be constant; or indeed if $Pr = 1$ the term in (2.6) containing this coefficient is negated. Alternatively, in the limit $M \to \infty$

$$\frac{2k}{1+k} \to 2$$

and hence this similarity condition is met.

2.1.4 The Third Similarity Condition

The final similarity condition is that

$$\frac{u_e' \Omega^2}{\rho_e \mu_e u_e^2} \frac{H_e}{h_e}$$

must be a constant. This is the coefficient in the final term after equation (2.7) has been applied to equation (2.5). First

$$\beta = \frac{u_e' \Omega^2}{\rho_e \mu_e u_e^2} = \frac{2\xi}{u_e} \frac{\mathrm{d}u_e}{\mathrm{d}\xi}$$

is defined and it is noted that

$$\frac{H_e}{h_e} = 1 + k.$$

Differentiating the latter by ξ, noting H_e is a constant, and employing the definition of h_e above,

$$\frac{u_e' \Omega^2}{\rho_e \mu_e u_e^2} \frac{H_e}{h_e} = \frac{2\xi}{u_e} \frac{\mathrm{d}u_e}{\mathrm{d}\xi} \frac{H_e}{h_e} = \beta (1 + k),$$

and for this to be a constant, it must be that

$$u_e = u_0 \xi^{\beta/2},$$

where u_0 is the velocity at the leading edge where $\xi = x = 0$. The physical interpretation of β is that it represents the streamwise variation of the external velocity and is taken to represent acceleration or retardation of the flow for positive and negative values of β respectively.

The β term is analogous to the parameter in the Falkner-Skan family of boundary layers, where the edge velocity $u_e \sim x^m$ and

$$\beta = \frac{2m}{m+1}.$$

2.1.5 Summary

To summarise, when the similarity conditions detailed above hold, the boundary-layer equations admit self-similar solutions which are governed by the equations

$$(Cf'')' + ff'' + \beta\,(1+k)\left(g - f'^2\right) = 0 \tag{2.9a}$$

$$\left(\frac{C}{Pr}g'\right)' + \frac{2k}{1+k}\left(1 - \frac{1}{Pr}\right)(Cf'f'')' + fg' = 0 \tag{2.9b}$$

with boundary conditions

$$f(0) = f'(0) = 0 \tag{2.10}$$

$$f' \to 1 \text{ and } g \to 1 \text{ as } \eta \to \infty \tag{2.11}$$

and either

$$g(0) = g_w, \tag{2.12}$$

where g_w is a specified constant, or

$$g'(0) = 0. \tag{2.13}$$

A true similarity solution exists if the edge velocity has the required power-law variation, and that either Pr is equal to unity or β is zero. The conditions for which a similarity solution exists are rather restrictive. When these conditions are not met, the development of the boundary layer in the streamwise direction departs from the self-similar behaviour and the boundary-layer equations (2.2) and (2.3) must instead be solved. Along with the difficulty of solving this set of non-linear partial differential equations, the leading edge ($x = \xi = 0$) presents a singularity. Stewartson (1964) provides a comprehensive discussion on historical

approximate methods and advocates the value of understanding the properties of similarity solutions before considering more general cases where a full solution of the boundary-layer equations (2.2) and (2.3) is necessary.

As an alternative, Dewey and Gross (1967) reviewed the then-available literature on the accuracy of using the similar solutions as an approximation for non-similar boundary layers. This is accomplished by considering an asymptotic expansion of coefficients that vary with ξ and approximating their effects by assuming these variations are small. The results support the use of a similarity solution.

Here, however, the similar solutions are considered as being representative of the full, non-self-similar flow to provide valuable qualitative cases for analysis. In particular, the overshoot boundary layers that are generated when the surface is heated and there is a favourable pressure gradient are focussed on. In figure 2.1 the velocity profiles of solutions to the boundary-layer equations (2.9) are presented for various parameter values.

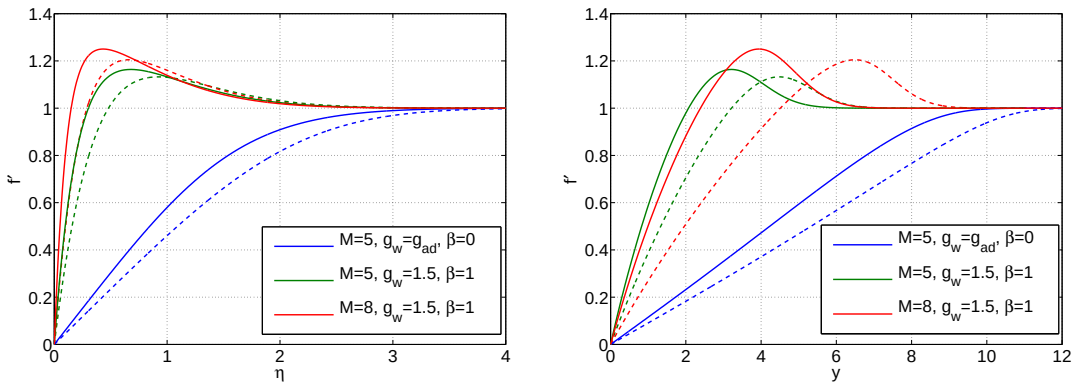

Figure 2.1: Velocity profiles of solutions to the boundary-layer equations with various parameter values, with a Sutherland viscosity-temperature model (solid line) and Chapman Law viscosity-temperature model (dashed line).

2.2 Far-field Asymptotic Behaviour

Here the behaviour of the boundary-layer equations (2.9) for large values of η are examined in order to establish the existence and nature of a velocity overshoot

in a compressible boundary layer with a heated surface and favourable pressure gradient. An analysis for a similar set of boundary-layer equations has been carried out by Reshotko and Beckwith (1958); which is used to motivate and inform the following analysis.

In the limit $\eta \to \infty$, f and g are expanded as $\tilde{f} = f_1 + f_2 + \cdots$ and $\tilde{g} = g_1 + g_2 + \cdots$ respectively, where each term in the series is asymptotically smaller than the previous for large η. These expansions are substituted into the boundary-layer equations (2.9) and leading order terms are retained. From the boundary condition (2.11),

$$f_1' = 1$$

and hence

$$f_1 = \eta - \kappa, \tag{2.14}$$

where κ is a constant. Equation (2.9a) becomes

$$\beta\,(1+k)\,(g_1 - 1) = 0,$$

$$g_1 = 1, \tag{2.15}$$

which is consistent with the enthalpy far-field condition given that $\beta > 0$. Retaining the second-order terms of $\tilde{f}$ and $\tilde{g}$ into (2.9a) and (2.9b) yields

$$f_2''' + (\eta - \kappa + f_2)\,f_2'' + \beta\,(1+k)\left(1 + g_2 - (1 - f_2'))^2\right) = 0$$

$$\frac{1}{Pr}g_2'' + \frac{2k}{1+k}\left(1 - \frac{1}{Pr}\right)\left(f_2''^2 + (1 + f_2')\,f_2'''\right) + (\eta - \kappa + f_2)\,g_2' = 0,$$

and the equations may be linearised, as f_2 and g_2 are taken to be asymptotically small, which yields

$$f_2''' + (\eta - \kappa)\,f_2'' + \beta\,(1+k)\,(g_2 - 2f_2') = 0 \tag{2.16}$$

$$\frac{1}{Pr}g_2'' + \frac{2k}{1+k}\left(1 - \frac{1}{Pr}\right)f_2''' + (\eta - \kappa)\,g_2' = 0. \tag{2.17}$$

First equation (2.17) is solved,

$$\left(g_2' \exp\left[\frac{Pr}{2}\,(\eta - \kappa)^2\right]\right)' = -\frac{2k}{1+k}\,(1 - Pr)\,f_2''',$$

which implies

$$g_2' = -\frac{2k}{1+k}\,(1 - Pr)\,f_2''E(\eta) + A_{G1}E(\eta)$$

and thus

$$g_2 = -\frac{2k}{1+k}\left(1-Pr\right)\int_{\infty}^{\eta} f_2'' E(\eta)\,\mathrm{d}\eta - A_{G1}\sqrt{\frac{\pi}{2Pr}}\mathrm{erfc}\left[-\sqrt{\frac{Pr}{2}}\left(\eta-\kappa\right)\right],$$

where

$$E(\eta) = \exp\left[-\frac{Pr}{2}\left(\eta-\kappa\right)^2\right].$$

and the second constant of integration is chosen to satisfy the boundary condition. This constant is zero when the complementary error function is chosen as the anti-derivative.

As f_2'' is expected to decay exponentially, the term involving the integral of $f_2'' E(\eta)$ is assumed to be asymptotically insignificant in the high-η limit. Now equation (2.16) may be solved, taking the first term in the series expansion of the complementary error function to represent g_2

$$\begin{aligned} f_2''' + \left(\eta-\kappa\right) f_2'' + \beta\left(1+k\right)\left(-2f_2'\right) &= \\ -\beta\left(1+k\right) A_{G1}\sqrt{\frac{2}{Pr\pi}}\left(\eta-\kappa\right)^{-1}\exp\left[-\frac{Pr\left(\eta-\kappa\right)^2}{2}\right], \end{aligned} \tag{2.18}$$

which has homogeneous solution

$$f_{2H}' = A_{F1}\left(\eta-\kappa\right)^{-3}\exp\left[-\frac{\left(\eta-\kappa\right)^2}{2}\right] + A_{F2}\left(\eta-\kappa\right)^2,$$

where $A_{F2} = 0$ is the suitable choice for consistency with the boundary condition. Seeking a particular solution of equation (2.18) in the form

$$f_{2P}' = A_F^*\left(\eta-\kappa\right)^N E(\eta),$$

yields the indicial equation

$$\begin{aligned} &\left(\eta-\kappa\right)^{N+2}\left[A_F^* Pr^2 - A_F^* Pr\right] + \left(\eta-\kappa\right)^N\left[-A_F^* Pr\left(2N+1\right) + A_F^* N - 2\beta\left(1+k\right)A_F^*\right] \\ &+ \left(\eta-\kappa\right)^{N-2}\left[A_F^* N\left(N-1\right)\right] = \left(\eta-\kappa\right)^{-1}\left[-\beta\left(1+k\right)A_{G1}\sqrt{\frac{2}{Pr\pi}}\right]. \end{aligned}$$

The distinguished limit is $N = -3$ and this yields

$$A_F^* = \frac{-\beta\left(1+k\right)}{Pr^2 - Pr}A_{G1}\sqrt{\frac{2}{Pr\pi}}.$$

The solutions for f' and g are

$$\tilde{f}' = 1 + A_F^*\left(\eta-\kappa\right)^{-3}E(\eta) + \cdots \tag{2.19}$$

$$\tilde{g} = 1 + A_{G1}\sqrt{\frac{2}{Pr\pi}}\,(\eta-\kappa)^{-1}\,E(\eta) + \cdots \tag{2.20}$$

and for $Pr < 1$, $\beta > 0$, A_F^* shares the same sign as A_{G1}. This implies that if $\tilde{g}$ approaches unity from above, so does $\tilde{f}'$ and the existence of velocity overshoot is established.

Now, returning to the energy equation (2.9b) in the form

$$g'' + Prfg' = -\frac{2k}{1+k}\left(1-\frac{1}{Pr}\right)(f'f'')', \tag{2.21}$$

noting that it is linear in g. The homogeneous solution for g' is

$$g'_{HG} = C_{G1}\exp\left(-Pr\int_0^\eta f(x)\,\mathrm{d}x\right), \tag{2.22}$$

where x is a dummy variable for integration. A particular solution has the form

$$g'_p = G(\eta)\exp\left(-Pr\int_0^\eta f(x)\,\mathrm{d}x\right), \tag{2.23}$$

and the energy equation gives the form

$$G(\eta) = -\frac{2k}{1+k}\left(1-\frac{1}{Pr}\right)\int_0^\eta (f'f'')'\exp\left(Pr\int_0^x f(x^*)\,\mathrm{d}x^*\right)\mathrm{d}x, \tag{2.24}$$

so

$$g' = [C_{G1} + G(\eta)]\exp\left(-Pr\int_0^\eta f(x)\,\mathrm{d}x\right). \tag{2.25}$$

Now, at $\eta = 0$, $G(\eta) = 0$, hence $g' = C_{G1} < 0$ as the surface is heated and transfers energy to the flow.

As $\eta \to \infty$, $f(\eta) \sim \eta - \kappa$ and from equation (2.19)

$$(f'f'')' = A_F^* Pr^2\,(\eta-\kappa)^{-1}\,E(\eta) + \cdots \tag{2.26}$$

and hence $G(\eta) \to 0$,

$$g' \to C_{G1}E(\eta) < 0 \tag{2.27}$$

and it follows that $g > 1$ and thus $f' > 1$ as $\eta \to \infty$.

In summary, it has been shown that for the boundary-layer equations 2.9 with boundary conditions (2.11) and (2.12) that for an accelerated flow ($\beta > 0$), if the enthalpy g approaches unity in the far-field from above, so does the streamwise velocity f'. If the wall is heated ($g_w > g_{ad}$ and hence $g'(0) < 0$) then g indeed approaches unity in the far-field from above. Hence there must be a velocity overshoot under the conditions of a heated wall and accelerating pressure gradient.

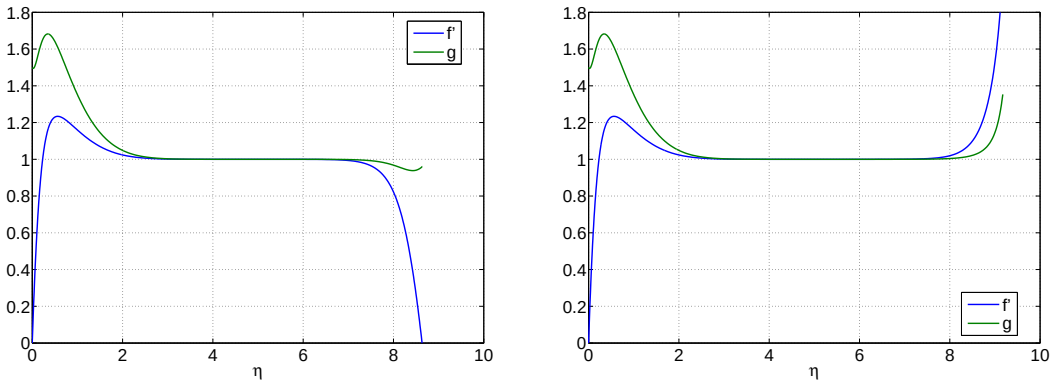

(a) $f''(0) = 7.378805532294611$ (b) $f''(0) = 7.378805532294612$

Figure 2.2: Sensitivity of the initial-value problem solution to shooting parameter $f''(0)$ for $M = 8$, $Pr = 0.7$, $g_w = 1.5$, $\beta = 1.5$ using the Chapman Law, with $g'(0) = -0.553107375046596$

2.3 Numerical Methods

The boundary layer is defined on a semi-infinite domain with the far-field boundary conditions to be satisfied as $\eta \to \infty$. In solving this system numerically, however, the domain must be truncated at some suitably large value of $\eta = \eta_{end}$, where the boundary conditions are applied.

The boundary-layer equations may be solved numerically as an initial-value problem (using a Runge-Kutta method) implementing a shooting method. Instead of using the far-field boundary conditions, the remaining wall conditions $f''(0)$ and $g'(0)$ are specified and iterated upon until the required far-field conditions are met. For simple cases when the momentum and energy equations are decoupled (as in, for example, the incompressible case), this method is most desirable for the low computational cost associated with initial-value methods.

However, in more general cases, the boundary-layer equations are numerically stiff and are difficult to solve as an initial-value problem. This is especially noticeable when there is velocity overshoot, as machine precision may not be enough to specify boundary conditions accurately enough to generate a boundary-layer profile to a sufficient distance from the wall, without rapid divergence from the desired asymptotic approach to the free-stream values.

This difficulty is highlighted by the results presented in Figure 2.2, which shows

two "solutions" obtained using the shooting method for a strongly accelerated, heated-surface boundary layer. With the enthalpy shooting parameter $g'(0)$ held constant at a suitable value, a difference of 10^{-15} in the velocity shooting parameter $f''(0)$ changes the divergence behaviour – the "correct" value lies between these.

In general it is more reliable to employ a boundary-value method where the correct boundary conditions are explicitly specified. The domain is truncated and the free-stream values are applied at the outer edge of the domain. The truncation is chosen to be at a sufficiently large value of η so that the error is to within some appropriate tolerance, here it is set to be 10^{-15}.

The boundary-value method also requires an initial estimate for the solution to iterate upon until a converged solution is achieved. This initial estimate can be produced from the initial-value method for a non-overshoot boundary layer. Then a continuation method is implemented to generate overshoot boundary layers.

The MATLAB functions *bvp4c* and *bvp5c* are employed to generate numerical solutions. The solvers use collocation and are 4th-order and 5th-order accurate respectively. The solvers differ in how they control errors, with the former controlling the residual and the latter directly controlling the error. When the boundary-layer equations are near-singular (i.e. large M), *bvp4c* converges whereas *bvp5c* does not, even when using a converged *bvp4c* solution as an initial guess.

The ability to calculate accurate solutions of the boundary-layer equations is very important for the subsequent stability analysis, which may be very sensitive to small changes in the basic state (for a discussion of this issue see Malik, 1990).

After the equations have been solved in the similarity co-ordinate η, the solution may be converted to the wall-normal boundary-layer co-ordinate Y by integrating

$$\frac{\mathrm{d}Y}{\mathrm{d}\eta} = T = (1+k)g - kf'^2$$

and appropriately scaling the η-derivative terms.

2.4 Properties of the Overshoot Boundary Layer

In this section properties of the boundary layer are presented that are of interest in both boundary-layer theory and for the stability analysis. There are three

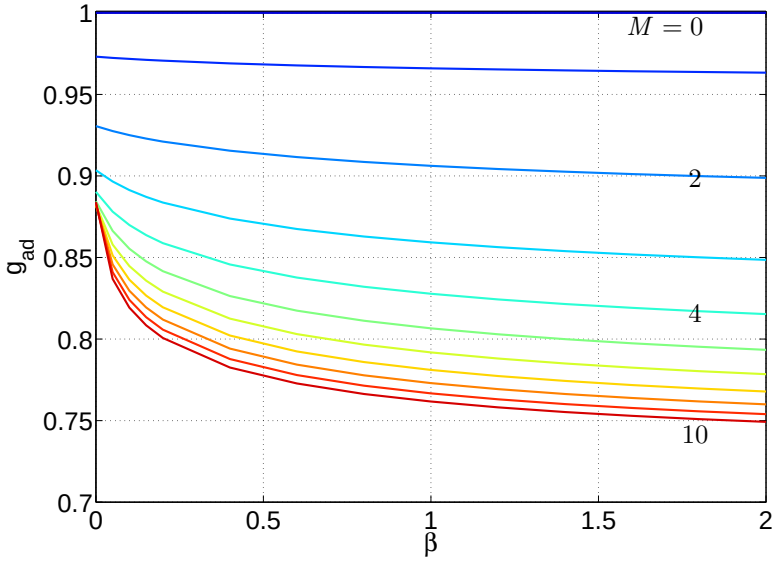

Figure 2.3: Adiabatic wall enthalpy versus pressure gradient parameter for various Mach numbers.

key parameters that affect the boundary-layer solution, the Mach number M, the pressure gradient parameter β and the wall enthalpy g_w. In addition, the choice of Prandtl number Pr and viscosity-temperature relationship are dependent on the fluid modelled and also have a significant effect, but for the results presented $Pr = 0.7$ and the Sutherland Law viscosity-temperature relationship is used.

Data is presented for $M \in [0, 10]$, $\beta \in [0, 2]$ and $g_w \in [g_{ad}, 2]$, where g_{ad} is the value of g_w when the surface is insulated; the adiabatic wall enthalpy. In Figure 2.3 the values of g_{ad} are plotted, and demonstrates that for a compressible boundary layer ($M > 0$) the adiabatic wall enthalpy is lower than the free-stream enthalpy and this effect is amplified with an increasingly favourable pressure gradient.

The skin friction,

$$\tau_w = \left(\mu \frac{\partial u}{\partial y}\right)_{y=0}$$

is a key parameter in aerodynamic surface design for calculating the overall friction drag on a body. In figure 2.4 the variation of the skin friction, non-dimensionalised by the edge values, within the parameter space is illustrated. For slightly favourable pressure gradients, an increase in wall enthalpy lowers the skin friction, but above a critical value of β the skin friction increases with wall enthalpy. This behaviour is

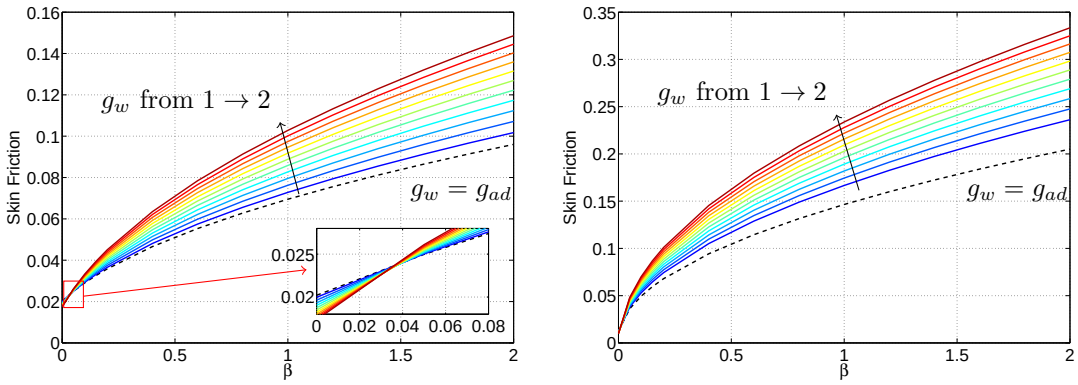

(a) $M = 2$ (b) $M = 10$

Figure 2.4: Skin friction versus pressure gradient parameter for various wall enthalpies at different Mach numbers.

evident in the inset of figure 2.4a. This critical value of β decreases with increasing Mach number.

The heat transfer at the wall,

$$K_w = \left(\kappa \frac{\partial T}{\partial y}\right)_{y=0}$$

is of interest for surface material selection and is plotted in figure 2.5. Negative values indicate energy being transferred from the wall to the boundary layer. As expected, a higher wall enthalpy results in higher energy transfer. Higher rates of acceleration also correlate to an increase in heat transfer, possibly due to convection, and a higher Mach number increases wall temperature dramatically and so it has a strong positive effect on this energy transfer.

In figure 2.6 the variability of the velocity maximum is plotted. The presence of a velocity maximum is a feature of overshoot boundary layers and is important as it is related to a new mode of inviscid stability to be discussed in the chapters 3 and 4. An interesting feature is that the data suggests that even for an adiabatic wall, there appears to be a velocity maximum when there is any favourable pressure gradient. This is proposed to be because $g_{ad} > Pr$ and hence the ultimate maximum velocity in the $M \to \infty$ limit (as determined in section 2.5) is greater than unity.

Another property of the compressible boundary layer important to inviscid sta-

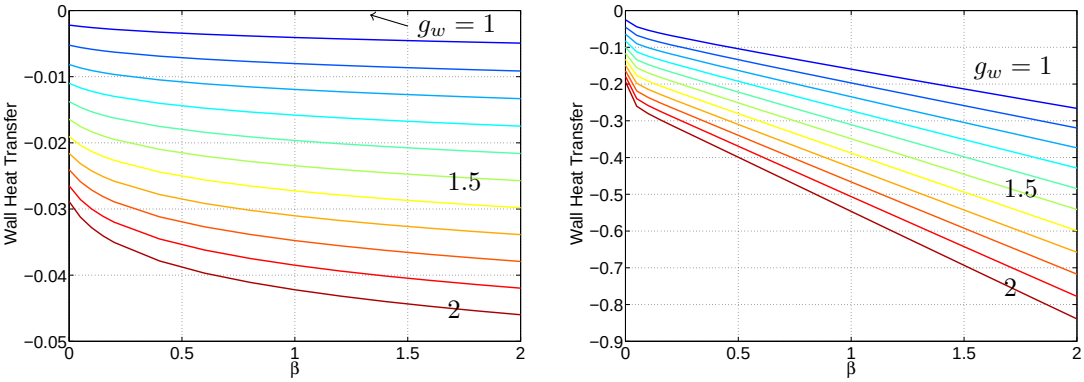

(a) $M = 2$ (b) $M = 10$

Figure 2.5: Wall heat transfer versus pressure gradient parameter for various wall enthalpies at different Mach numbers.

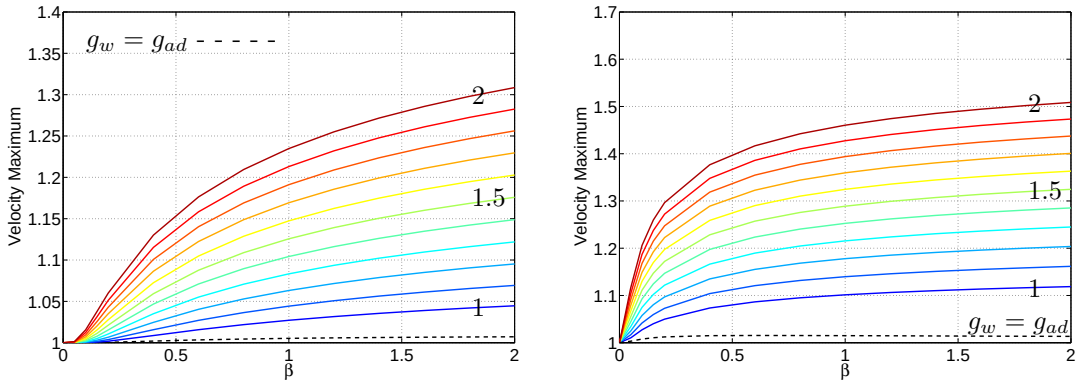

(a) $M = 4$ (b) $M = 10$

Figure 2.6: Velocity maximum versus pressure gradient parameter for various wall enthalpies at different Mach numbers

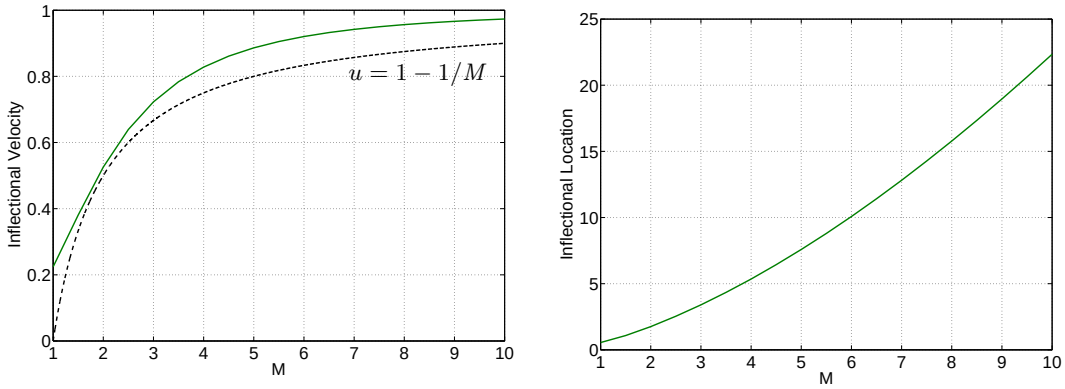

Figure 2.7: Velocity (plotted with sonic velocity $1 - 1/M$) and location of generalised points of inflection for boundary layers with an insulated wall and no pressure gradient.

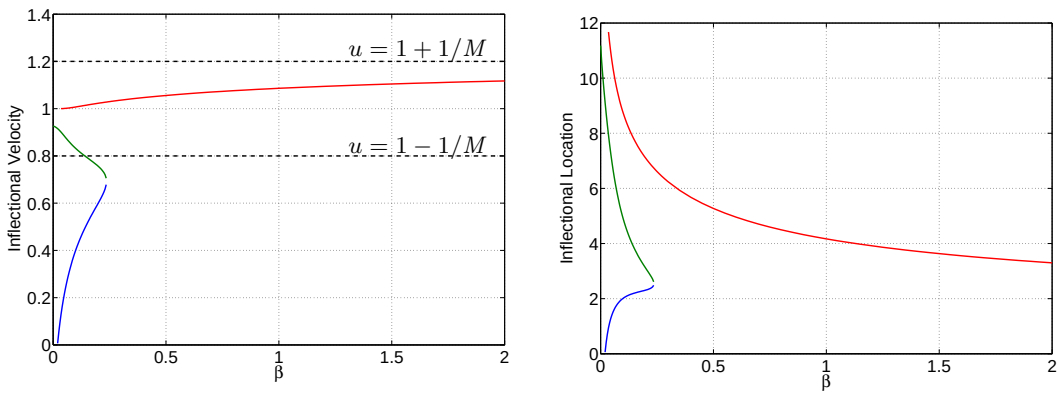

Figure 2.8: Velocity (plotted with sonic velocities $1 \pm 1/M$) and location of generalised points of inflection for boundary layers with $M = 5$, $g_w = 1.5$ and variable β.

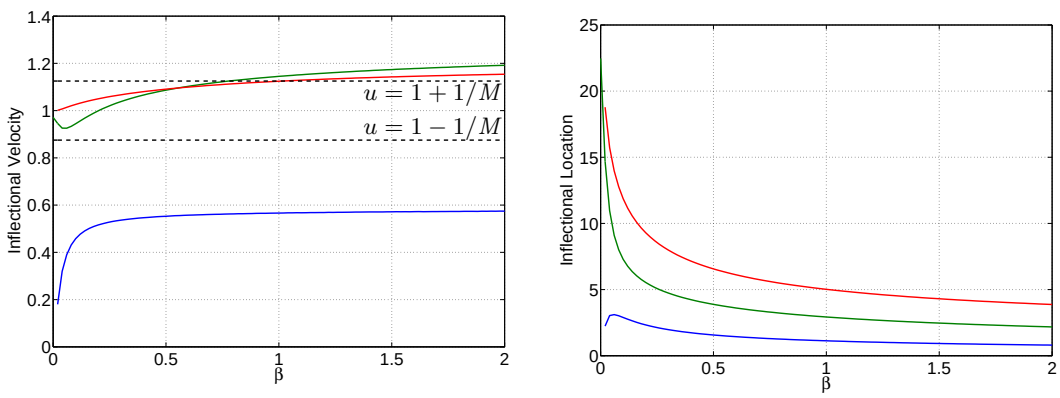

Figure 2.9: Velocity (plotted with sonic velocities $1 \pm 1/M$) and location of generalised points of inflection for boundary layers with $M = 8$, $g_w = 1.5$ and variable β.

bility is the generalised points of inflection, defined by equation (1.69). In figure 2.7, the velocity at, and location of, generalised points of inflection are plotted for a compressible, flat-plate boundary layer (which does not exhibit any velocity overshoot). There is only one generalised point of inflection and its velocity is always subsonic relative to the flow, defined by equation (1.67).

In figures 2.8 and 2.9, compressible boundary layers with a heated surface and variable pressure gradient are explored. For these boundary layers, a generalised point of inflection always exists on the free-stream side of the velocity maximum, and hence corresponds to a velocity greater than unity. There may also be another pair of points, depending on whether the local maximum of $(\rho u')'$ lies above or below the axis $(\rho u')' = 0$. The turning point in figure 2.8 at $\beta \approx 0.24$ is an illustration of the local maximum moving below the axis. The inflectional velocities are plotted alongside the sonic velocities at $1 \pm 1/M$. These values are borders that demarcate the change in nature of infinitesimal neutral disturbances with a wavespeed equal to the inflectional velocity. Between these lines the disturbances are "subsonic" and it is these disturbances that are the focus of most of the prevailing stability theory and subsequently the main focus of the following work.

2.5 Hypersonic ($M \to \infty$) Limit

In this limit the nature of the boundary-layer equations provide an exact similarity solution, however they also become singular. This opens up the possibility of an analytic solution, which could be of practical use when the Mach number is large (but not necessarily infinite). As the Mach number increases, the presence of shock waves and other hypersonic effects are expected to have a significant impact, however these equations are likely to hold in at least some part of the boundary layer (Smith and Brown, 1990).

2.5.1 Chapman Law Viscosity-Temperature Model

First the case where viscosity is proportional to the temperature is investigated. Recalling that there is a favourable pressure gradient ($\beta > 0$),

$$\epsilon = [\beta\,(1+k)]^{-1} \sim O(M^{-2})$$

is a small parameter, $2k/(1+k) \to 2$. In this case the boundary-layer equations (2.9a) and (2.9b) become

$$\epsilon f''' + \epsilon f f'' + g - f'^2 = 0 \tag{2.28}$$

$$g'' + 2\,(Pr-1)\left(f''^2 + f' f'''\right) + Pr f g' = 0. \tag{2.29}$$

The equations are singular in the limit of $\epsilon \to 0$. The "outer" solutions when ϵ is set to zero, f_o and g_o, satisfy

$$g_o = f_o'^2 \tag{2.30}$$

$$f_o' f_o''' + f_o''^2 + f_o f_o' f_o'' = 0. \tag{2.31}$$

The outer solutions may satisfy the far-field boundary conditions but the wall boundary conditions are not compatible with the outer solution. It is conjectured that a (mathematical) boundary layer exists near $\eta = 0$. To explore this, consider the behaviour of (2.28) and (2.29) as $\eta \to 0$ by seeking solutions of the form

$$f \sim \eta^a\,(A_0 + A_1\eta + \cdots)\,,$$

$$g \sim g_w + \eta^b\,(B_0 + B_1\eta + \cdots)\,,$$

where $a > 1$ (so that f' conforms to the no-slip boundary condition) and $b > 0$. Substitution into equations (2.28) and (2.29) yields a dominant balance for which the suitable choice is $a = 3$ and $b = 4$. The coefficients may be evaluated by solving in powers of η, yielding A_i and B_i ($i = 1, 2, 3, \ldots$), where

$$A_0 = -\frac{g_w}{6\epsilon}, \quad A_1 = A_2 = A_3 = 0, \quad A_4 = \frac{3g_w^2 Pr - 2g_w^2\epsilon}{2520\epsilon^3}, \quad \cdots$$

$$B_0 = \frac{g_w^2\,(1-Pr)}{4\epsilon^2}, \quad B_1 = B_2 = B_3 = 0,$$

$$B_4 = \frac{42g_w^3\left(Pr^2-1\right) + g_w^3\,(28+15Pr)\,(1-Pr)\,\epsilon}{5040\epsilon^4}, \quad \cdots.$$

In the limit $\epsilon \to 0$ power series for f and g may be written as

$$f \sim O(\epsilon^{-1})\eta^3 + O(\epsilon^{-3})\eta^7 + O(\epsilon^{-5})\eta^{11} + \cdots$$

$$g \sim g_w + O(\epsilon^{-2})\eta^4 + O(\epsilon^{-4})\eta^8 + O(\epsilon^{-6})\eta^{12} + \cdots,$$

which suggests that there is a boundary layer of size $O(\epsilon^{1/2})$ in which $g \sim O(1)$ and $f \sim O(\epsilon^{1/2})$. With $z = \eta/\epsilon^{1/2}$, $f = \epsilon^{1/2}\tilde{f}(z) + \cdots$ and $g = \tilde{g}(z) + \cdots$, at leading order in powers of ϵ the boundary-layer equations are

$$\tilde{f}_{zzz} + \tilde{g} - \tilde{f}_z^2 = 0 \tag{2.32}$$

$$\tilde{g}_{zz} + 2\,(Pr - 1)\left(\tilde{f}_{zz}^2 + \tilde{f}_z\tilde{f}_{zzz}\right) = 0. \tag{2.33}$$

Equation (2.33) may be integrated twice to give a form for $\tilde{g}$,

$$\tilde{g} = C_1 z + C_2 + (1 - Pr)\,\tilde{f}_z^2, \tag{2.34}$$

where C_1 and C_2 are constants of integration. As $\tilde{f}_z$ represents the (scaled) streamwise velocity and must be zero at $z = 0$, then $C_2 = g_w$ and $C_1 = g_z|_{z=0}$. Bounded behaviour as $z \to \infty$ is required to match the outer solution (and hence the boundary conditions) so it is necessary that $C_1 \equiv 0$. Using this form for $\tilde{g}$ in (2.32),

$$\tilde{f}_{zzz} - Pr\tilde{f}_z^2 = -g_w. \tag{2.35}$$

The solution to (2.35) may be expressed in terms of Weierstrass Elliptic functions (Abramowitz and Stegun, 1966), however these are not suitable for matching with the boundary conditions due to their periodicity and singular nature. Instead, the equation is solved numerically as an initial value problem for the scaled streamwise velocity $\tilde{f}_z$ with no-slip at the wall ($\tilde{f}_z = 0$ at $z = 0$), using the wall shear ($\tilde{f}_{zz}$ at $z = 0$) as a shooting parameter. A bounded solution appears to exist for a specific value of the wall shear, whereby the solution approaches a constant value as $z \to \infty$.

To investigate, let $\tilde{f} \sim f_m + U_m z + H(z)$ as $z \to \infty$, so that $\tilde{f}_z \sim U_m + H'(z)$, where f_m and U_m are constants and $H(z) \ll z$. With this substitution, equation (2.35) becomes, after linearising about $H'(z)$

$$H''' - 2PrU_m H' = -g_w + PrU_m^2,$$

which can be integrated to give

$$H' = \frac{-g_w + U_m^2 Pr}{2U_m Pr} + C_1 \exp(\sqrt{2U_m Pr}z) + C_2 \exp(-\sqrt{2U_m Pr}z),$$

where C_1 and C_2 are constants of integration. To constrain $H'(z) \ll 1$ as $z \to \infty$ it must be that $C_1 = 0$ and $-g_w + U_m^2 Pr = 0$. This defines the ultimate velocity, and hence the ultimate enthalpy (from equation 2.34) in the wall critical layer as

$$U_m = \sqrt{\frac{g_w}{Pr}},$$

$$g_m = \lim_{z\to\infty} \tilde{g} = g_w + (1 - Pr)U_m^2 = \frac{g_w}{Pr}.$$

Now, to find an expression for the wall shear, equation (2.35) is multiplied by $\tilde{f}_z z$, and integrated to give

$$\frac{1}{2}\tilde{f}_{zz}^2 - \frac{Pr}{3}\tilde{f}_z^3 = -g_w \tilde{f}_z + C_3. \tag{2.36}$$

At $z = 0$ this becomes

$$\frac{1}{2}\tilde{f}_{zz}(0)^2 = C_3. \tag{2.37}$$

Now, if $\tilde{f}_{zz} \to 0$ as $z \to \infty$, then in this limit (2.36) becomes

$$-\frac{Pr}{3}\left(\frac{g_w}{Pr}\right)^{3/2} = -g_w\sqrt{\frac{g_w}{Pr}} + \frac{1}{2}\left(\tilde{f}_{zz}(0)\right)^2, \tag{2.38}$$

hence

$$\tilde{f}_{zz}(0) = \pm\frac{2}{\sqrt{3}}\frac{g_w^{3/4}}{Pr^{1/4}} \tag{2.39}$$

and the inner solution is closed by choosing the positive solution as $\tilde{f}_z > 0$ is required.

In terms of the macroscopic variables, the solution as $z \to \infty$, $\tilde{f} \to f_m + U_m z + H(z)$, becomes

$$f \to \epsilon^{\frac{1}{2}} f_m + U_m \eta + H(\epsilon^{-\frac{1}{2}}\eta),$$

which is in a suitable form for matching with the outer solution. Given this, seek a solution to the outer equation (2.31) as $\eta \to 0$ in the form of $f_o = U_m\eta + \Omega(\eta)$, where $\Omega(\eta) \ll \eta$, such that $f_o' = U_m + \Omega'(\eta)$. Linearising the resulting equation (as $\Omega(\eta) \ll \eta$ and $\eta \to 0$) yields

$$\Omega''' + U_m \eta \Omega'' = 0,$$

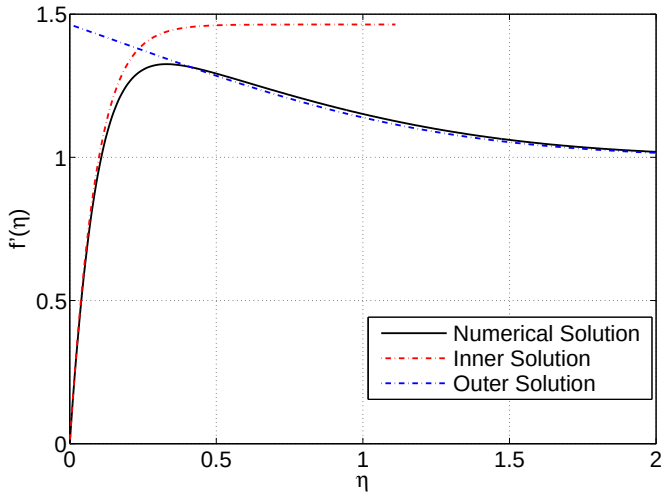

Figure 2.10: Numerical solution for an overshoot boundary layer with $M = 20$, $g_w = 1.5$ and $\beta = 1$ ($\epsilon \approx 0.012$) and leading-order terms of the power series expansion.

which has the solution, as $U_m > 0$,

$$\Omega'(\eta) = F_2 + F_1\sqrt{\frac{\pi}{2U_m}}\,\mathrm{erf}\left(\sqrt{\frac{U_m}{2}}\eta\right),$$

where F_1 and F_2 are constants of integration. The constant F_2 must be zero to conform to the small magnitude assumption as $\eta \to 0$. Thus

$$\Omega(\eta) = F_3 + F_1\sqrt{\frac{\pi}{2U_m}}\left[\sqrt{\frac{2}{\pi U_m}}\exp\left(-\frac{U_m}{2}\eta^2\right) + \eta\,\mathrm{erf}\left(\sqrt{\frac{U_m}{2}}\eta\right)\right]$$

and

$$F_3 = -\frac{F_1}{U_m},$$

thus

$$\Omega\left(\eta\right) = F_1\left[-\frac{1}{U_m}\left(1 - \exp\left(-\frac{U_m}{2}\eta^2\right)\right) + \sqrt{\frac{\pi}{2U_m}}\eta\,\mathrm{erf}\left(\sqrt{\frac{U_m}{2}}\eta\right)\right]. \tag{2.40}$$

The problem is closed by choosing F_1 such that the far-field boundary condition is satisfied. The correct value can be found numerically using a shooting method. An analytic solution for $f''(0)$ is not readily obtainable. Once equation (2.31) has been solved, g may be determined by using equation (2.30). An example solution for a Mach-20 boundary layer is plotted in figure 2.10.

2.5.2 Sutherland Law Viscosity-Temperature Model

With $C(\eta)$ unspecified, and ϵ defined as in section 2.5.1 the boundary-layer equations are

$$\epsilon\left(Cf''\right)' + \epsilon f f'' + g - f'^2 = 0 \tag{2.41}$$

$$\left(Cg'\right)' + 2\left(Pr - 1\right)\left(Cf'f''\right)' + Prfg' = 0, \tag{2.42}$$

and the process is similar to the Chapman Law analysis. The outer equations are

$$g_o = f_o'^2 \tag{2.43}$$

$$\left(Cf_o'f_o''\right)' + f_o f_o' f_o'' = 0, \tag{2.44}$$

which are again unable to satisfy the boundary conditions at $\eta = 0$. Before taking a power series solution for f and g as $\eta \to 0$, consider the nature of C. Near the wall, the temperature $T \sim \epsilon^{-1}\left(g - f'^2\right)$ and from equation (2.4)

$$\begin{aligned} \lim_{T\to\infty} C &= (1+S)T^{-1/2} \\ &= \epsilon^{-1/2}(1+S)\left(g - f'^2\right). \end{aligned} \tag{2.45}$$

The series expansions for f and g are therefore the same; $a = 3$ and $\beta = 4$ again, but now

$$A_0 = -\frac{g_w^{3/2}}{6(1+S)\epsilon^{3/2}}, \quad A_1 = A_2 = A_3 = 0, \quad A_4 = \frac{g_w^{7/2}(21Pr - 4\epsilon)}{5040(1+S)^3\epsilon^{9/2}},$$

$$B_0 = -\frac{(Pr-1)g_w^3}{4(1+S)^2\epsilon^3}, \quad B_1 = B_2 = B_3 = 0,$$

$$B_4 = \frac{(Pr-1)g_w^5(147Pr - (15Pr+28)\epsilon)}{5040(1+S)^4\epsilon^6},$$

and continuing reveals that with the Sutherland Law, there is a wall layer of size $O(\epsilon^{3/4})$, in which $g \sim O(1)$ and $f \sim O(\epsilon^{3/4})$. Taking $\hat{z} = \epsilon^{-3/4}\eta$, expand

$$\begin{aligned} C &\sim \epsilon^{1/2}\left(\frac{1+S}{\sqrt{g_w}} + O(\eta^4)\right) \\ &\sim \epsilon^{1/2}\left(\frac{1+S}{\sqrt{g_w}} + O(\epsilon^{5/2}\hat{z}^4)\right) \end{aligned}$$

as T is large. With $f = \epsilon^{3/4}\hat{f}(\hat{z}) + \cdots$ and $g = \hat{g}(\hat{z}) + \cdots$, at leading order the boundary-layer equations become

$$S^*\hat{f}_{\hat{z}\hat{z}\hat{z}} + \hat{g} - \hat{f}_{\hat{z}}^2 = 0 \tag{2.46}$$

$$S^*\hat{g}_{\hat{z}\hat{z}} + 2(Pr-1)S^*\left(\hat{f}_{\hat{z}}\hat{f}_{\hat{z}\hat{z}}\right)_{\hat{z}} = 0, \tag{2.47}$$

where

$$S^* = \frac{1+S}{\sqrt{g_w}}.$$

These equations differ from equations (2.32) and (2.33) only by their constant coefficients. However, again

$$\hat{f}_{\hat{z}} \to \sqrt{\frac{g_w}{Pr}}$$

and

$$\hat{g} \to \frac{g_w}{Pr}$$

as $\hat{z} \to \infty$.

In the outer region, temperature $T_o \equiv g_o = f_o'^2$, and as before seek a solution as $\eta \to 0$ in the form $f_o = U_m\eta + \hat{\Omega}(\eta)$, where $\hat{\Omega}(\eta) \ll \eta$. Using the full expression in equation (2.4) for C and linearising about $\hat{\Omega}$

$$C = \frac{(1+S)U_m}{U_m^2+S} - \frac{2(1+S)U_m^2}{(U_m^2+S)^2}\hat{\Omega} + \frac{1+S}{U_m^2+S}\hat{\Omega}' + \cdots$$

and the linearised outer equations simplify to

$$\hat{\Omega}''' + \frac{U_m^2+S}{1+S}\eta\hat{\Omega}'' = 0,$$

which again differs from the Chapman Law by the form of the constant coefficient.

The only qualitative difference in the choice of viscosity-temperature law for the hypersonic overshoot boundary layer appears to be the size of the wall layer; this in turn will change the surface friction. The ultimate velocity maximum however remains unchanged.

2.6 Summary

The boundary-layer equations (2.9a) and (2.9b) admit a velocity overshoot when the surface is heated and an accelerating pressure gradient is applied and the existence of such behaviour has been demonstrated numerically and analytically. In the large Mach number limit the boundary layer has a two-layered structure and an analytic solution has been found. As opposed to flat-plate boundary layers,

overshoot boundary layers can possess multiple generalised points of inflection; these are a condition for an inviscid instability and so the stability structure is affected. In the following chapters, the inviscid and viscous stability structure of the overshoot boundary layer is investigated.

Chapter 3

Inviscid Stability Numerical Results

With the stability of overshoot boundary layers unknown a priori, it is reasonable to first investigate their inviscid stability for a number of reasons: Firstly, compressible boundary layers are often most unstable in the inviscid limit. Secondly, there are fewer stability parameters and considerations regarding the fluid model to make. Thirdly, the lower order of the stability equations allows a greater coverage of the parameter space in a shorter time. Finally, the multiple generalised points of inflection in overshoot boundary layers are expected to modify the inviscid stability.

In the following sections numerical stability results for a number of boundary layers are presented to give an overview of the stability behaviour encountered. The cases considered are summarised in table 3.1. The descriptors "moderate", "high", and "extreme" with regards to overshoot refer to cases where $\bar{u}_{max}$ and all values of $\bar{u}_c$ are subsonic ($1 - 1/M < c < 1 + 1/M$), only values of $\bar{u}_c$ are subsonic and both $\bar{u}_{max}$ and all values of $\bar{u}_c$ are supersonic, respectively. Results are presented for streamwise two-dimensional disturbances; oblique two-dimensional disturbances are briefly considered in chapter 4.

Table 3.1: Table of boundary-layer cases used for analysis.

Case	M	g_w	β	$\bar{u}_{max}$	$\bar{u}_c$ (*)	Description
1	4	g_{ad}	0	1	0.8289	Flat-plate boundary layer
1a	4	0.9	0.1	1.000004	0.7962	Incipient overshoot
2	7	g_{ad}	0	1	0.9430	Flat-plate boundary layer
3	8	1.2	0.4	1.103	1.009, 1.052	Moderate overshoot
3a	8	1.2	0.38	1.100	1.005, 1.050	Modified case 3
4	8	1.3	0.3	1.111	1.006, 1.051	Moderate overshoot
4a	8	1.3	0.32	1.115	1.011, 1.053	Modified case 4
4b	8	1.3	0.28	1.106	1.001, 1.049	Modified case 4
4c	8	1.3	0.25	1.098	0.9934, 1.045	Modified case 4
5	7	1.5	1	1.226	1.086, 1.113	High overshoot
6	10	1.5	0.7	1.266	1.124, 1.194	Extreme overshoot
7	3	2.3	2	1.311	1.146	Low Mach number

*Inflectional velocities less than $1 - 1/M$ are not quoted.

3.1 Computational Considerations

The reduction of order in the stability equations, obtained by taking the inviscid assumption (see section 1.3.4), introduces a number of challenges to the analysis. First, note that the sign of $\Im(c)$ is ambiguous; for a given (complex) eigenvalue c with an associated eigenfunction $\hat{v}$, the complex conjugate of c is also an eigenvalue with the eigenfunction being the complex conjugate of $\hat{v}$. For neutral modes (c real), the inviscid stability equations contain a singularity if and where $\bar{u} = c$; this singularity cannot be avoided when the domain lies entirely upon the real axis.

For the case of no velocity overshoot, both of these issues may be addressed after analysis of the critical layer (Lees and Lin, 1946), from which it can be argued that a valid integration contour must pass sufficiently far below the singularity in the complex plane (Mack, 1969). For unstable disturbances the singularity is above the real axis and for damped disturbances it is below.

Previous analysis of the critical point singularity assumes that at the critical point, $D\bar{u} > 0$. This is not necessarily the case for boundary layers with velocity overshoot. For real values of c between 1 and the velocity maximum $\bar{u}_{max}$, there are

two such points where $\bar{u} = c$ and these have opposite signs of $D\bar{u}$. If at the critical point $D\bar{u} < 0$, instead the integration contour must pass sufficiently far above the critical point in the complex plane. In addition, for unstable and damped disturbances the singularity is now below and above the real axis respectively. The presence of two singularities presents the possibility whereby the regions in which the inviscid solutions are invalid overlap in such a way that there is no valid integration contour linking the surface to the freestream. Further details of the validity of the inviscid solutions are outlined in section 5.1.

3.2 Method of Numerical Solution

For numerical solution of the inviscid stability equations (1.57) and (1.58) are solved subject to the boundary conditions $\hat{v}(0) = 0$ and $\hat{v}$ bounded as $y \to \infty$.

Eigenvalues are determined using a local search method. For a given α and an estimated eigenvalue c, the stability equations are solved as an initial value problem over a truncated domain. The freestream is taken to be located at a finite value of $y = y_{end}$ (chosen to be sufficiently larger than the boundary-layer thickness) where the freestream conditions are applied. The eigenfunctions may be arbitrarily scaled, so without loss of generality the initial values are taken as; from equation (1.65)

$$\hat{p}_{end} = \exp\left[-\left(\alpha\sqrt{1-(1-c)^2 M^2}\right) y_{end}\right],$$

and from equation (1.57)

$$\hat{v}_{end} = \frac{i\sqrt{1-(1-c)^2 M^2}}{(1-c)}\hat{p}_{end}$$

and the stability equations are integrated towards $y = 0$ using the fourth-order Runge-Kutta method. The eigenvalue is accepted if the value of $\hat{v}(0)$ is close to zero within a specified tolerance. Newton's method is applied to the error in the boundary condition $\hat{v}(0)$ to converge on eigenvalues.

As the eigenvalues and eigenfunctions are complex, the convergence regions are fractal in nature. In figure 3.1 the convergence regions of two eigenvalues at the

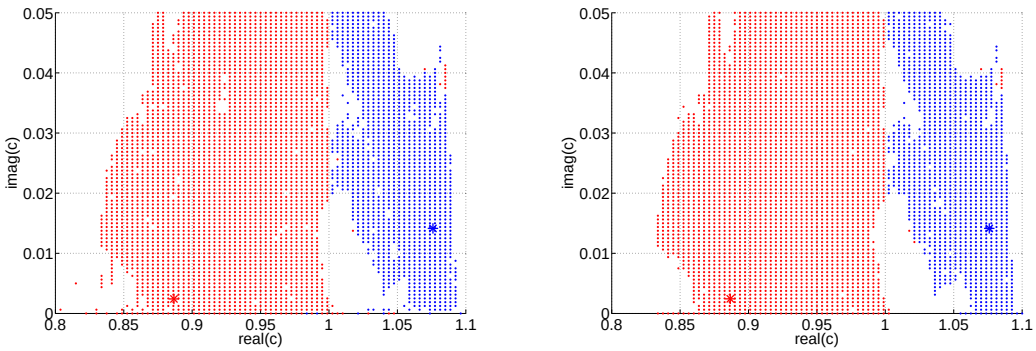

(a) $N = 500$ (b) $N = 1500$

Figure 3.1: Local eigenvalue search convergence diagram for boundary-layer case 3 at $\alpha = 0.05$.

same wavenumber is illustrated by testing at a discrete set of starting values. The eigenvalues are located at the stars and the dots indicate initial guesses that converge to an eigenvalue; the colour of the dots referring to the eigenvalue converged to. Locales without a dot indicate failure of the local search method. While most initial guesses near to each eigenvalue converge, there are points nearby which fail to converge. With a larger number of integration points convergence improves. The borders of the convergence regions are irregular and the pockets of convergence to the red eigenvalue near the top-right of the figures are further indications of the fractal nature of the convergence regions.

In the case of figure 3.1, the eigenvalues converge rapidly. However, this is not always true. In figure 3.2 two nearby eigenvalues exist but one is highly dominant. At even higher wavenumbers it becomes successively more difficult to converge to the blue eigenvalue.

Once an eigenvalue is found, a family of eigenvalues may be traced out by parametric continuation in α. A small change in α is made and another local search is undertaken using the previous value of c. Once a number of eigenvalues have been found, polynomial extrapolation methods are implemented to provide a better estimate of c for subsequent values of α. At each stage, the eigenvalues are scrutinised to ensure they are of the same family by limiting the drift of c from the initial guess, and by comparing eigenfunctions. Upon detection of an anomaly the α-step is reduced to ensure continuity.

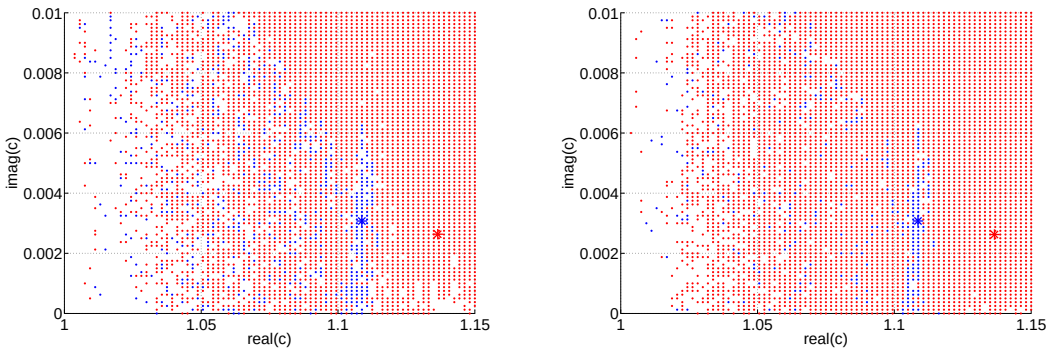

(a) $N = 500$ (b) $N = 1500$

Figure 3.2: Local eigenvalue search convergence diagram for boundary-layer case 5 at $\alpha = 1.08$.

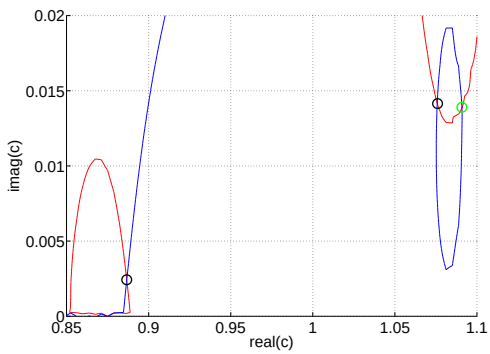

Figure 3.3: Contours of error in boundary-value for guessed eigenvalue c for boundary-layer case 3 at $\alpha = 0.05$.

There are no natural global eigenvalue search methods available for the inviscid stability equations given the non-linearity of the eigenvalue c, hence it is difficult to determine if all eigenvalues and their families have been found. In lieu of a global search, for a given boundary layer and value of α, the boundary condition errors, $\hat{v}(0)$, are determined for a large number of (complex) guessed eigenvalues c and contours of $\Re(\hat{v}(0)) = 0$ and $\Im(\hat{v}(0)) = 0$ are plotted. Intersections of these contours indicate the possible location of an eigenvalue. In figure 3.3 one such set of contours is plotted. The black circles indicate true eigenvalues and the green circle is not an eigenvalue. At the green circle, and near the real axis ($\Im(c) \approx 0$), the contour lines correspond to singularities where error is large but a sign change occurs (i.e. a pole), and hence do not represent true eigenvalues.

In order to avoid passing close to a singularity, before each integration of the stability equations is performed, the location of singularities in complex y-space are determined using the approximation

$$y_c \approx y_r + \frac{\Im(c)i}{D\bar{u}(y_r)},$$

where y_r are the point(s) where $\bar{u} = \Re(c)$. For guessed eigenvalues with $\Im(c) > 0$ (unstable disturbance), the singularity is ignored unless $\Im(y_c) < 0.01$. For such "near singularities" and for cases where $\Im(c) \leq 0$, the integration contour is indented below (or above in the case of $D\bar{u}(y_r) < 0$) the singularity with a clearance of 0.01 in the complex plane. Additional integration points are allocated in these regions and the boundary-layer profiles in the complex plane are calculated through Taylor series expansions. The contour indentation is not strictly necessary for unstable disturbances with a small growth rate, however this aids continuity when calculating eigenvalue families passing a neutral point. The eigenfunctions are only valid on the real y-axis, however the eigenvalues are still valid. This method was originally developed for the incompressible problem and is discussed in detail by Mack (1969). In the interest of minimising errors associated with the Taylor series expansions, calculations of highly damped modes are not presented.

3.3 Classical Inviscid Eigenvalue Modes

Lees and Lin (1946) identified the upstream family (a continuous set) of eigenvalues, which commences at $\alpha = 0$, $c = 1 - 1/M$. Following this eigenvalue as α is increased, $\Re(c)$ increases and $\Im(c)$ remains positive (and hence this family is unstable) until $\Re(c)$ reaches the value of the streamwise velocity within the boundary layer at a generalised point of inflection (inflectional velocity), where it becomes neutral and subsequently damped. This is the classical "first mode" instability, where a "mode" refers to a set of eigenvalues near a local maximum in the growth rate. The upstream family is the only family of eigenvalues when M is small enough such that the relative Mach number (as defined in equation 1.68) $\bar{M} < 1$ everywhere; in this case, the inviscid stability equations are elliptic and only one set of eigenvalues exist (Reed and Saric, 1996).

Mack (1969) recognised the possibility of the additional eigensolutions, termed higher modes or "Mack modes". Mack also identified the downstream families, for which the nth commences at $\alpha = \alpha_{dn}$, $c = 1 + 1/M$ and $\alpha_{d1} = 0$. The mode identity can be confirmed by examining the eigenfunctions; the mode number is the number of zeros in the pressure perturbation plus one. For each of these downstream families, as α increases $\Re(c)$ decreases but $\Im(c)$ remains zero until $\Re(c)$ becomes 1. After this value of α, $\Im(c)$ is positive until $\Re(c)$ reaches the inflectional velocity, when it becomes neutral and subsequently damped.

A portion of the eigenvalue diagram for a non-overshoot boundary layer (case 1) is presented in figure 3.4. The blue curve corresponds to the upstream family and contains the first mode, after which it becomes damped as it passes the value of the streamwise velocity at the generalised point of inflection. The green curve is the first downstream family and contains the second mode when it becomes unstable. Higher modes (contained in the second and subsequent downstream families) are omitted as they do not contain significant regions of instability.

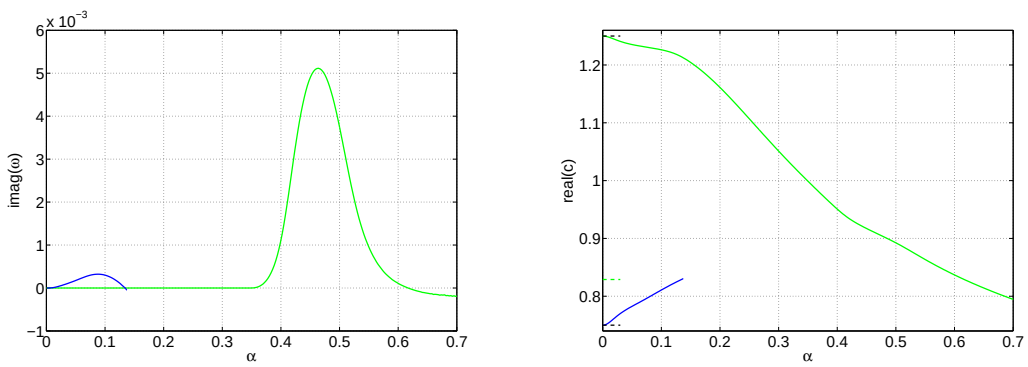

(a) Growth rate vs wavenumber

(b) Disturbance wavespeed vs wavenumber, with inflectional velocity (– – –) and sonic velocities (– – –)

Figure 3.4: Eigenvalue diagram for boundary-layer case 1 ($M = 4$, $g_w = g_{ad}$, $\beta = 0$) with upstream family (blue) and first downstream family (green).

In figure 3.5 an eigenvalue diagram for a higher Mach number non-overshoot boundary layer (case 2) is presented. As the Mach number is increased, the first mode unstable zone broadens and the second mode unstable zone moves to lower wavenumbers and eventually the two unstable zones merge. Furthermore, the

higher-order modes become more prominent. Mode 3 has a small unstable zone at around $\alpha = 0.45$ (not shown) with a maximum value of $\Im(c)$ of about 0.001. The first downstream family (not shown) contains an insignificantly small second mode instability. The reader is referred to Mack (1987) for a more detailed discussion on the inviscid stability behaviour of non-overshoot boundary layers.

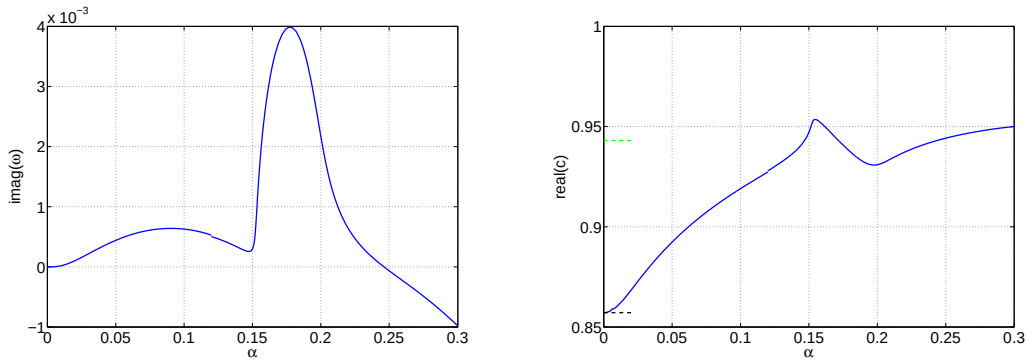

(a) Growth rate vs wavenumber

(b) Disturbance wavespeed vs wavenumber, with inflectional velocity (– – –) and upstream sonic velocity (– – –)

Figure 3.5: Eigenvalue diagram for boundary-layer case 2 ($M = 7$, $g_w = g_{ad}$, $\beta = 0$) with upstream family (blue).

3.4 Overshoot Boundary Layers

The overshoot boundary layers, as outlined in Chapter 2, are the result of a heated surface and a favourable pressure gradient. The physical changes to the boundary layer, even at a very low level, results in large changes to the stability behaviour. In figure 3.6, an eigenvalue diagram for a boundary layer with a very small overshoot (case 1a) is presented. In contrast to case 1, the first mode is significantly damped. The second mode is also slightly damped but is unstable over a larger range of wavenumbers. These effects are due to the reduction of the inflectional velocity to a value closer to $1 - 1/M$.

When a moderate amount of overshoot (approximately 10%) is introduced, there are further changes to the inviscid stability of a qualitative nature. In figure 3.7, the eigenvalue diagram for a boundary layer with moderate overshoot is presented.

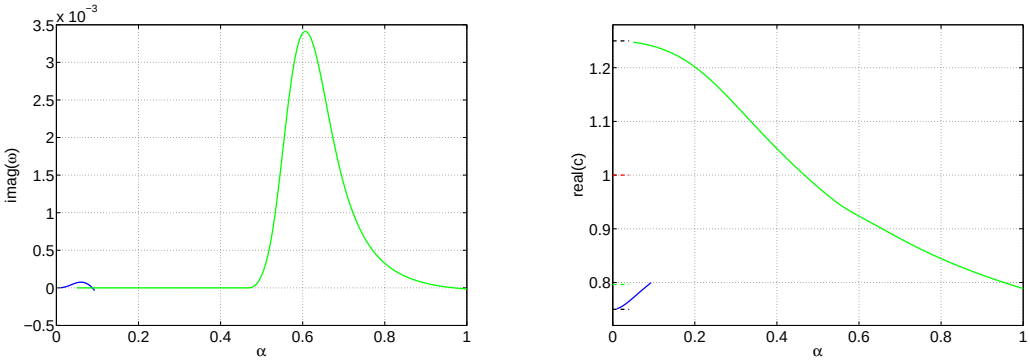

(a) Growth rate vs wavenumber

(b) Disturbance wavespeed vs wavenumber, with inflectional velocity (– – –), sonic velocities (– – –) and maximum velocity (– – –)

Figure 3.6: Eigenvalue diagram for boundary-layer case 1a ($M = 4$, $g_w = 0.9$, $\beta = 0.1$) with upstream family (blue) and first downstream family (green).

The upstream family (blue) contains the first, second and third modes and becomes neutral at one of the inflectional velocities. In addition to this family there is a new family of eigenvalues (red), appearing to originate at $\alpha = 0$, $c = \bar{u}_{max}$. It contains a significant region of instability and becomes neutral at a value of c between the two inflectional velocities, which is remarkable. This non-inflectional neutral wavespeed will be referred to as c_m. The downstream family (green) contains minor second and third mode instabilities but these, particularly the minor second mode, are considerably stronger than those in non-overshoot boundary layers. Interestingly, instead of the downstream family becoming unstable once c has decreased to unity, this now occurs as c passes $\bar{u}_{max}$.

Next boundary-layer cases 4a, 4, 4b and 4c (see table 3.1) are presented to illustrate the interaction between the new mode and the existing higher modes. In case 4a (figure 3.8), the upstream family contains the first, second and third modes and the new family contains just the new mode. In case 4 (figure 3.9), the pressure gradient parameter β has been decreased slightly, the wavenumber range of the new mode has expanded and the first mode has diminished slightly, almost detaching from the second and third modes. By case 4b (figure 3.10), the first mode has detached sufficiently that there are two distinct unstable zones. The first mode

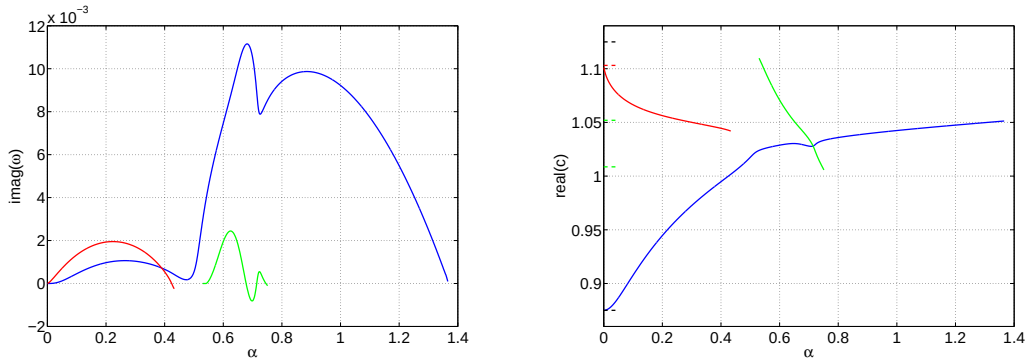

(a) Growth rate vs wavenumber

(b) Disturbance wavespeed vs wavenumber, with inflectional velocity (– – –), sonic velocities (– – –) and maximum velocity (– – –)

Figure 3.7: Eigenvalue diagram for boundary-layer case 3 ($M = 8$, $g_w = 1.2$, $\beta = 0.4$) with upstream family (blue), downstream family (green) and new family (red).

is neutralised at an inflectional velocity, and the second mode commences at a neutral mode with a non-inflectional wavespeed (not equal to c_m). After a further reduction in β to case 4c (figure 3.11), the detachment of the first mode is complete and the new mode has expanded enough such that the new family now contains the second and third modes.

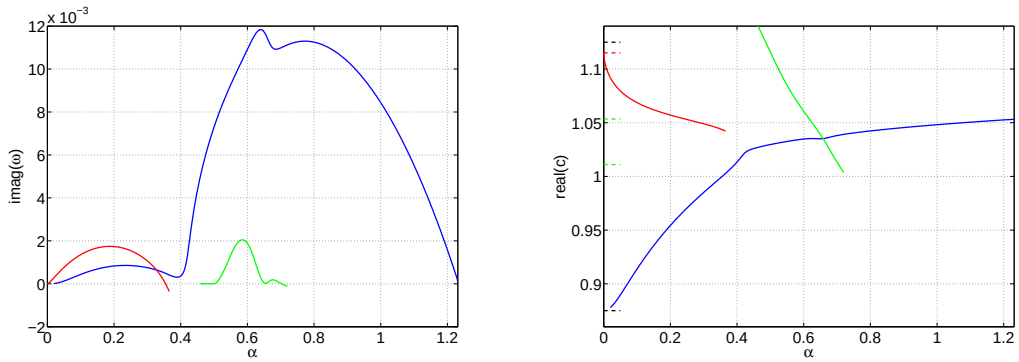

(a) Growth rate vs wavenumber

(b) Disturbance wavespeed vs wavenumber, with inflectional velocity (– – –), sonic velocities (– – –) and maximum velocity (– – –)

Figure 3.8: Eigenvalue diagram for boundary-layer case 4a ($M = 7$, $g_w = 1.3$, $\beta = 0.32$) with upstream family (blue), downstream family (green) and new family (red).

In boundary-layer case 5, the overshoot has been increased to the point that

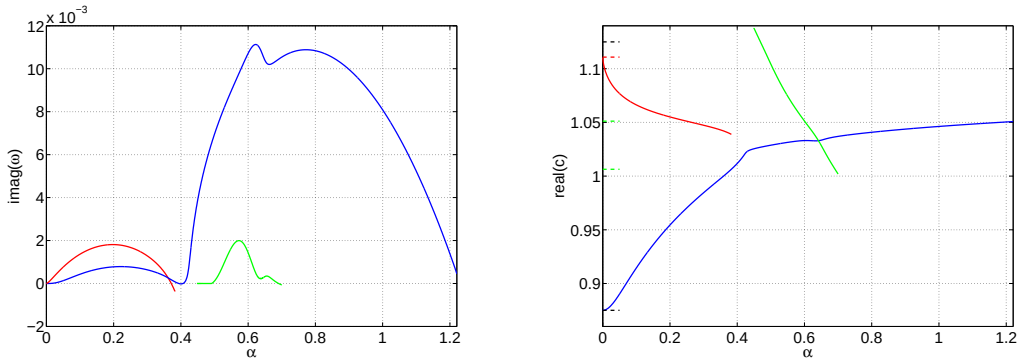

(a) Growth rate vs wavenumber

(b) Disturbance wavespeed vs wavenumber, with inflectional velocity (– – –), sonic velocities (– – –) and maximum velocity (– – –)

Figure 3.9: Eigenvalue diagram for boundary-layer case 4 ($M = 7$, $g_w = 1.3$, $\beta = 0.3$) with upstream family (blue), downstream family (green) and new family (red).

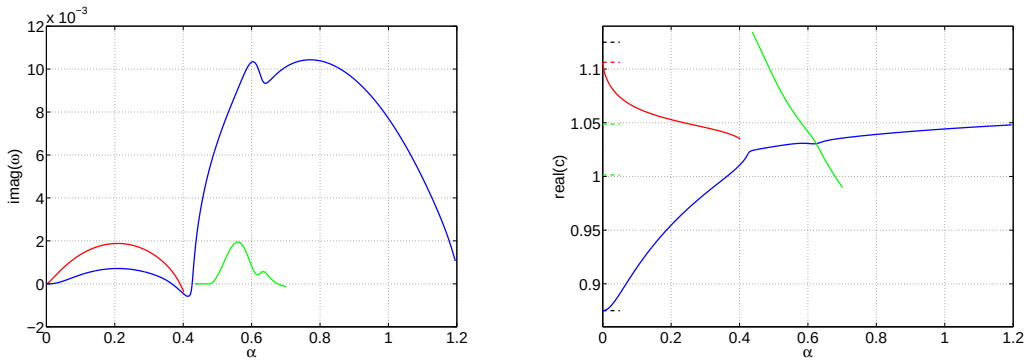

(a) Growth rate vs wavenumber

(b) Disturbance wavespeed vs wavenumber, with inflectional velocity (– – –), sonic velocities (– – –) and maximum velocity (– – –)

Figure 3.10: Eigenvalue diagram for boundary-layer case 4b ($M = 7$, $g_w = 1.3$, $\beta = 0.28$) with upstream family (blue), downstream family (green) and new family (red).

the maximum velocity is higher than the sonic velocity $1 + 1/M$. This diminishes the new mode, which now commences at $\alpha = 0$, $c = 1 + 1/M$, replacing the first downstream family. This initial wavespeed is considerably closer to c_m, which still lies between the two inflectional velocities. The green curve consists of the second downstream family, which becomes unstable at the (now supersonic) $c = \bar{u}_{max}$, contains a minor second and major third mode instabilities and is stabilised at a

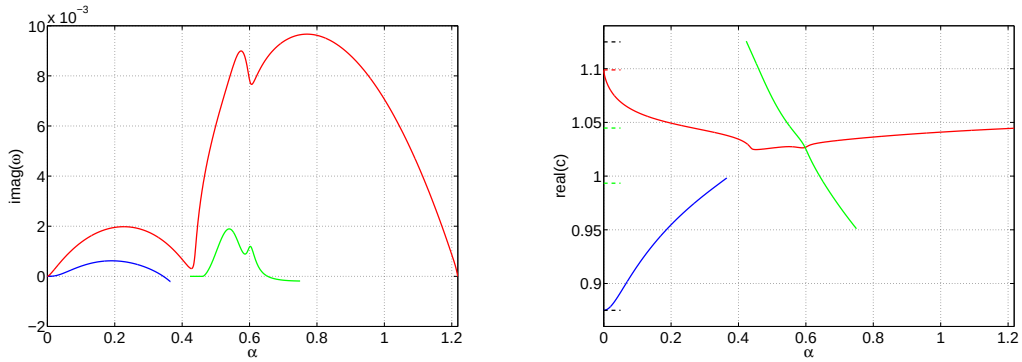

(a) Growth rate vs wavenumber

(b) Disturbance wavespeed vs wavenumber, with inflectional velocity (– – –), sonic velocities (– – –) and maximum velocity (– – –)

Figure 3.11: Eigenvalue diagram for boundary-layer case 4c ($M = 7$, $g_w = 1.3$, $\beta = 0.25$) with upstream family (blue), downstream family (green) and new family (red).

non-inflectional wavespeed close to c_m.

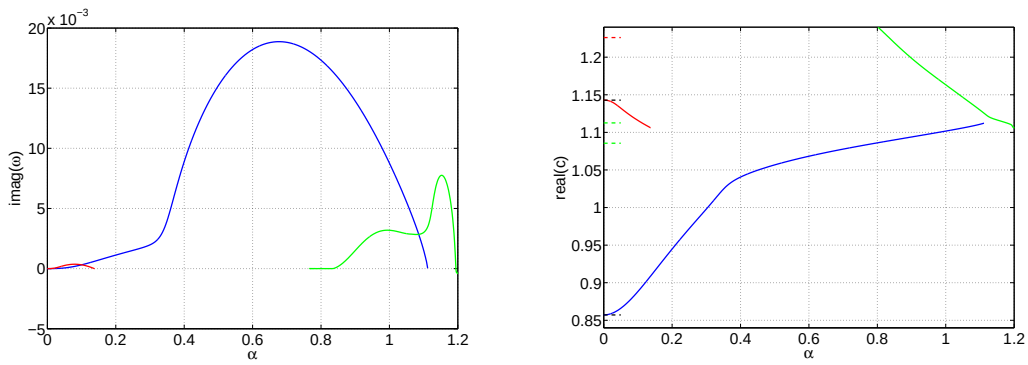

(a) Growth rate vs wavenumber

(b) Disturbance wavespeed vs wavenumber, with inflectional velocity (– – –), sonic velocities (– – –) and maximum velocity (– – –)

Figure 3.12: Eigenvalue diagram for boundary-layer case 5 ($M = 7$, $g_w = 1.5$, $\beta = 1$) with upstream family (blue), downstream family (green) and new family (red).

In boundary-layer case 6, the overshoot is further increased to the point that the inflectional velocities (and presumably c_m) is increased beyond $1 + 1/M$. The upstream family now contains the first, second and third mode instabilities and becomes neutral at a supersonic wavespeed that is non-inflectional. The new mode is no longer detected. The second downstream family is completely supersonic in

nature and as in case 5, is stabilised at a non-inflectional wavespeed.

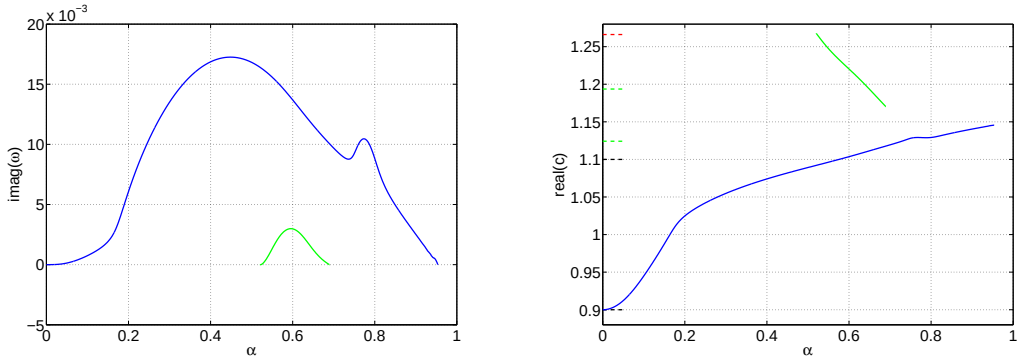

(a) Growth rate vs wavenumber

(b) Disturbance wavespeed vs wavenumber, with inflectional velocity (– – –), sonic velocities (– – –) and maximum velocity (– – –)

Figure 3.13: Eigenvalue diagram for boundary-layer case 6 ($M = 10$, $g_w = 1.5$, $\beta = 0.7$) with upstream family (blue), downstream family (green) and new family (red).

In all the cases considered above, the maximum growth rate of the new mode is small relative to that of the second and third modes. As a final example, figure 3.14 illustrates the eigenvalues of boundary-layer case 7, where the new mode has the highest growth rate. As the Mach number is lower in this case, the second mode is not as prominent and belongs to the new family. Also of interest here is that the upstream family contains no unstable solutions; the first mode is completely stabilised. Crucially, this boundary layer has only one generalised point of inflection. This inflectional velocity does not correspond to any of the neutral modes; the second mode becomes neutral at a non-inflectional velocity, possibly c_m.

3.5 Maximum Growth Rate of New Mode

A new unstable inviscid mode has been identified in all of the overshoot boundary layers considered in the previous section. When the velocity overshoot is very small this mode is not detected. As the overshoot increases the mode becomes more prominent and ultimately disappears after the overshoot has increased sufficiently such that the non-inflectional neutral wavespeed c_m becomes supersonic. Using boundary-layer case 4 as a base, the effect of the boundary-layer parameters M

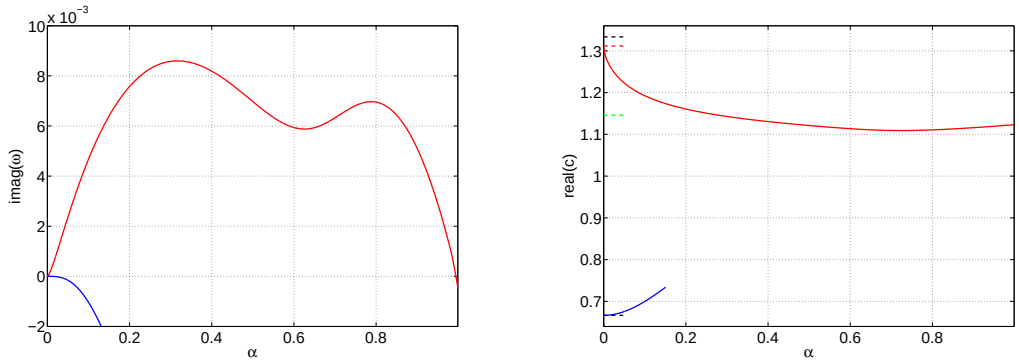

(a) Growth rate vs wavenumber

(b) Disturbance wavespeed vs wavenumber, with inflectional velocity (– – –), sonic velocities (– – –) and maximum velocity (– – –)

Figure 3.14: Eigenvalue diagram for boundary-layer case 7 ($M = 3$, $g_w = 2.3$, $\beta = 2$) with upstream family (blue) and new family (red).

(figure 3.15), β (figure 3.16) and g_w (figure 3.17) on the maximum growth rate of the new mode, and the wavenumber at which the maximum occurs, is presented.

The increase of each parameter corresponds to an increase in the amount of overshoot. At large parameter values, an increase corresponds to a decrease in the maximum growth rate and the movement of the location of the maximum closer to $\alpha = 0$. At small parameter values, a decrease corresponds to a lower maximum growth rate and an increase in the corresponding wavenumber. The exception with is the pressure gradient parameter, for which the boundary layer is very sensitive at low values (see section 2.4).

3.6 Summary

The introduction of velocity overshoot into the boundary layer causes changes of a quantitative and qualitative nature to the stability characteristics. A number of new types of neutral mode have been identified along with another set of low-wavenumber unstable modes that can co-exist with the first mode.

The singular nature of the inviscid stability equations require that these numerical results must be scrutinised analytically, or by confirming that the results presented are indeed the high Reynolds number limit of the viscous stability results.

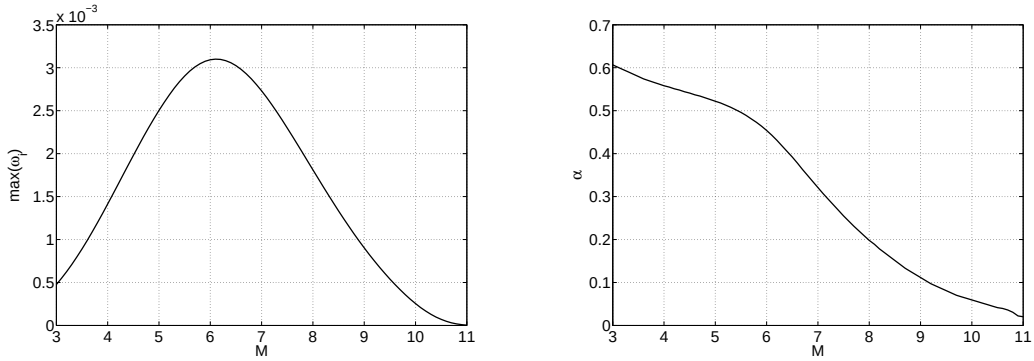

(a) Maximum growth rate vs Mach number

(b) Wavenumber at maximum growth rate vs Mach number

Figure 3.15: Maximum growth rate for boundary-layer case 4 for various Mach numbers ($g_w = 1.3$, $\beta = 0.3$).

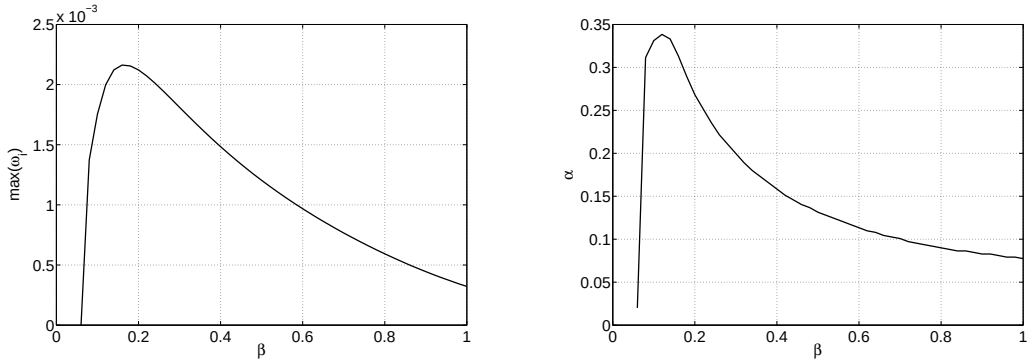

(a) Maximum growth rate vs pressure gradient parameter

(b) Wavenumber at maximum growth rate vs

Figure 3.16: Maximum growth rate for boundary-layer case 4 for various pressure gradient parameters ($M = 8$, $g_w = 1.3$).

These are accomplished in the subsequent chapters.

The new unstable mode could be important in the transition process in overshoot boundary layers as its growth rate can exceed those of the traditional modes.

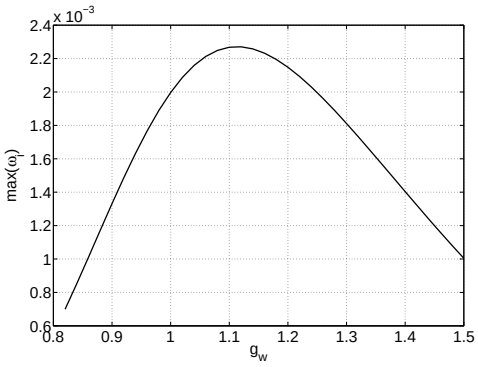

(a) Maximum growth rate vs enthalpy

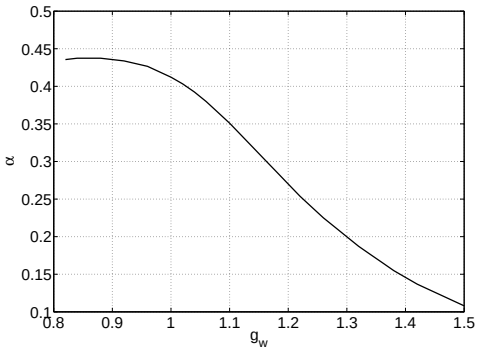

(b) Wavenumber at maximum growth rate vs wall enthalpy

Figure 3.17: Maximum growth rate for boundary-layer case 4 for various variable wall enthalpies ($M = 8, \beta = 0.3$).

Chapter 4

Inviscid Stability Analysis and Discussion

The inviscid stability analysis presented in the previous chapter uncovers some interesting results for overshoot boundary layers. In this chapter a local analysis around the singular point at $\bar{u} = c$ is performed, and in particular the case where $c = \bar{u}_{max} > 1$, a case unique to overshoot boundary layers. The low-wavenumber neutral mode associated with the new unstable mode presented in Chapter 3 is examined and an analytic (i.e. asymptotic) solution is developed in the low-wavenumber limit. This result is the key outcome of work published in Tunney et al. (2015). The validity of the inflectional and new non-inflectional neutral modes are discussed. The nature of these neutral modes change when the Mach number is sufficiently large and this behaviour is examined in detail. Finally, velocity overshoot modifies the oblique-wave stability of the traditional modes; this is analysed and in addition, the growth rates of the oblique new mode are discussed.

4.1 Local Analysis of the Singular Point at $\bar{u} = c$

The Rayleigh equation, described by equations (1.57) and (1.58), is singular at the point $y = y_c$ where $\bar{u} = c$. For neutral modes ($\Im(c) = 0$), y_c lies on the real axis. In order to explore the critical layer structure of the neutral eigenmodes two cases are considered; when the critical layer is not located at the position of the velocity

maximum and the case when it occurs precisely at the location of the velocity maximum.

4.1.1 Case 1: $c \neq \bar{u}_{max}$

In order to develop a solution it is first noted that since $Y \equiv y - y_c = 0$ is a regular singluar point of equation (1.62), the expansion for $\hat{v}$ about $Y = 0$ is of the form

$$\hat{v} = a_0 Y^n + a_1 Y^{n+1} + \cdots. \tag{4.1}$$

Substitution of this expansion into (1.62) yields, at leading order in powers of Y, the indicial equation

$$\bar{T}_c D\bar{u}_c n\,(n-1)\,a_0 = 0; \tag{4.2}$$

here a subscript c denotes a quantity evaluated at the critical point. As $\bar{T} > 0$ everywhere and $D\bar{u}_c \neq 0$, the choice $n = 1$ yields a solution of the form of a regular series expansion in powers of Y:

$$\hat{v}_A = a_0 Y + a_1 Y^2 + a_2 Y^3 + \cdots \tag{4.3}$$

where the first two coefficients are given by

$$a_1 = \frac{1}{2}\left(\frac{D^2\bar{u}_c}{D\bar{u}_c}\right) a_0, \quad a_2 = \frac{1}{6}\left(\alpha^2 + \frac{D^3\bar{u}_c}{D\bar{u}_c}\right) a_0.$$

Standard theory on the local solution of ordinary differential equations then guarantees that there is a second linearly independent solution on the form

$$\hat{v}_B = \hat{v}_A \log Y + b_0 + b_1 Y + b_2 Y^2 + \cdots. \tag{4.4}$$

Substituting this expression into equation (1.62) it is found that a_0 and b_0 are related via the expression

$$a_0 = b_0 \frac{\bar{T}_c}{D\bar{u}_c}\left[D\left(\frac{D\bar{u}}{\bar{T}}\right)\right]_c. \tag{4.5}$$

This expansion can be carried to higher order, allowing for the determination of b_2, b_3 etc. to be determined in terms of the leading order terms b_0 and b_1. These results are not presented here. If the condition

$$\left[D\left(\frac{D\bar{u}}{\bar{T}}\right)\right]_c = 0, \tag{4.6}$$

is satisfied then, from equation (4.5), $a_0 = 0$ and so $a_k \equiv 0$, for all $k \geq 1$ and the logarithmic singularity in the second linearly dependent solution (4.4) is removed. This condition, when satisfied, also ensures that the Wronskian is continuous across the critical layer (Lees and Lin, 1946). The presence of such a *generalised inflection point* is a sufficient condition for the existence of a neutral, subsonic, inviscid disturbance with wavenumber $\alpha = \alpha_{sn} > 0$, and ensures that this is adjacent to unstable eigenvalues at $\alpha < \alpha_{sn}$ using the notation introduced Mack (1987) for neutral wavenumbers.

4.1.2 Case 2: $c = \bar{u}_{max}$

Suppose now that the neutral mode is such that $c = \bar{u}_{max}$. Since the streamwise velocity has a maximum at this point, $D\bar{u}_c = 0$ and the point $Y = 0$ is still a regular singular point. With the expansion for $\hat{v}$ as before, the indicial equation is now given by

$$D^2\bar{u}_c\bar{T}_c^2\,(n+1)\,(n-2)\,\hat{a}_0 = 0, \tag{4.7}$$

with two possible solutions $n = -1$ and $n = 2$ (noting that $D^2\bar{u}_c \neq 0$). The $n = 2$ case yields the solution

$$\hat{v}_A = \hat{a}_0 Y^2 + \hat{a}_1 Y^3 + \cdots$$

where

$$\hat{a}_1 = \frac{1}{3}\left(\frac{D^3\bar{u}_c}{D^2\bar{u}_c}\right)\hat{a}_0, \tag{4.8}$$

$$\hat{a}_2 = \left(\frac{1}{10}\alpha^2 + \frac{1}{12}\frac{D^4\bar{u}_c}{D^2\bar{u}_c}\right)\hat{a}_0. \tag{4.9}$$

A second linearly independent solution can be written as

$$\hat{v}_B = \hat{v}_A \log Y + \hat{b}_0 Y^{-1} + \hat{b}_1 + \hat{b}_2 Y + \cdots \tag{4.10}$$

which, when substituted into the compressible Rayleigh equation and upon equating orders of Y, yields

$$\hat{a}_0 = \hat{b}_0\left[-\frac{1}{2}\alpha^2 + \frac{3}{2}\frac{D^2\bar{T}_c}{\bar{T}_c} - \frac{3}{2}\frac{D^3\bar{u}_c D\bar{T}_c}{D^2\bar{u}_c\bar{T}_c} - \frac{5}{12}\frac{D^4\bar{u}_c}{D^2\bar{u}_c} + \frac{2}{3}\frac{\left(D^3\bar{u}_c\right)^2}{\left(D^2\bar{u}_c\right)^2}\right]. \tag{4.11}$$

The difference between this case and the previous generalised inflection point case, is now evident. In order to remove the logarithmic term, the term in the brackets

in equation (4.11) must necessarily be zero, thus serving to (possibly) determine the neutral wavenumber α_c. However, in this case the second linearly independent solution, given by equation (4.10), still possesses an algebraic singularity.

When the boundary layer does not have a velocity overshoot, $\bar{u}_{max}$ is unity and occurs in the freestream. In this case all the velocity derivatives are zero and the above analysis is not applicable. Such a neutral mode does exist in the classical theory and is adjacent to the higher mode solutions discovered by Mack (1969).

4.2 The New Low-Wavenumber Neutral Mode

Lees and Lin (1946) developed series solutions for equation (1.62), valid in the small wavenumber limit, in powers of α^2 of the form $\hat{v} = C_1\hat{v}_1 + C_2\hat{v}_2$, where $\hat{v}_1$ and $\hat{v}_2$ represent the two linearly independent solutions, given by

$$\begin{aligned} \hat{v}_1 &= (\bar{u} - c)\left(I + \alpha^2 \int_0^y I \frac{(\bar{u} - c)^2}{\bar{T}} \mathrm{d}y^* + O(\alpha^4)\right) \\ \hat{v}_2 &= (\bar{u} - c)\left(1 + \alpha^2 \int_0^y \frac{(\bar{u} - c)^2}{\bar{T}} \mathrm{d}y^* + O(\alpha^4)\right), \end{aligned} \tag{4.12}$$

where

$$I = \int_0^y \left[\frac{\bar{T}}{(\bar{u} - c)^2} - M^2\right] \mathrm{d}y^*, \tag{4.13}$$

and C_1 and C_2 are arbitrary constants. Provided that $c \neq 0$, in the limit $\alpha \to 0$, C_2 must be zero in order to satisfy the wall boundary condition. In order to satisfy the boundedness condition as $y \to \infty$, the integral I must approach a constant in this limit. Thus the integrand appearing in equation (4.13) must tend to zero as $y \to \infty$. Noting that both $\bar{T}$ and $\bar{u}$ tend to unity as $y \to \infty$, $M^2(1 - c)^2 = 1$. Hence the neutral wavespeed is given by

$$c = c_0 = 1 \pm \frac{1}{M}.$$

These neutral mode solutions are termed *sonic modes*, since in this case the disturbance travels downstream or upstream respectively at the local speed of sound.

The numerical solutions presented in chapter 3 suggest that there is another neutral mode present as $\alpha \to 0$, for which $c \to \bar{u}_{max}$. In general, $\bar{u}_{max} \neq 1 + 1/M$

so $\hat{v}_1$ will not necessarily be bounded, violating the freestream boundary condition. This immediately suggests that each of the two linearly independent solutions will play a different role in different regions of the flow. The wall boundary condition forces the choice of the $\hat{v}_1$ solution whereas the boundedness condition forces the choice of the $\hat{v}_2$ solution. Thus, in the small α limit, the solution structure proposed is

$$\hat{v} \sim \begin{cases} \hat{v}_1 \sim (\bar{u} - c)\, I & y < y_c \\ V & y \text{ near } y_c \\ \hat{v}_2 \sim (\bar{u} - c) & y > y_c, \end{cases} \tag{4.14}$$

where y_c is the position of the velocity maximum and V is an unknown function which will be determined with asymptotic analysis.

To investigate this behaviour for small α, write $c = \bar{u}_{max} + \alpha^m c_1$, where c_1 may be complex, and introduce a new scaled co-ordinate $z = (y - y_c)/\delta$, where $\delta = \alpha^n$ and $n > 0$. Expanding all flow quantities in a Taylor series about $y = y_c$, equation (1.62) can be written as

$$\begin{aligned} &\frac{\mathrm{d}}{\mathrm{d}z}\left\{\left[\frac{\frac{1}{2}\lambda z^2 + \frac{1}{6}D^3\bar{u}_c\alpha^n z^3 - \alpha^{m-2n}c_1 + O\left(\alpha^{2n}\right)}{\bar{T}_c + D\bar{T}_c\alpha^n z + O\left(\alpha^{2n}\right)}\right]\frac{\mathrm{d}\hat{v}}{\mathrm{d}z} - \right. \\ &\left.\left[\frac{\lambda z + \frac{1}{2}D^3\bar{u}_c\alpha^n z^2 + O\left(\alpha^{2n}\right)}{\bar{T}_c + D\bar{T}_c\alpha^n z + O\left(\alpha^{2n}\right)}\right]\hat{v}\right\} = O\left(\alpha^{2+\frac{2}{n}}\right) \end{aligned} \tag{4.15}$$

where a subscript c indicates a quantity evaluated at y_c and for convenience $\lambda = D^2\bar{u}_c$ has been defined. A simple dominant balance argument serves to determine that $m = 2n$. Analysis of the numerical results strongly suggests that $m = 2/3$, and hence $n = 1/3$. However m, and hence n, must be determined *a posteriori* by matching the solution across the various distinguished asymptotic layers that arise in the flow. To proceed, the solution can be split into three regions defined as:

Region L: $0 < y \ll y_c$, in which the solution must satisfy the boundary condition $\hat{v}(0) = 0$,

Region I: $|y - y_c| \sim O(\delta)$, in which the solution must match with region L and region R which is defined as

Region R: $y_c \ll y < \infty$, in which the solution must be bounded.

4.2.1 Leading Order, $O(\alpha^0)$, solution

Region L

In this region, let $\hat{v} = \hat{v}_L$ and note that the boundary condition to be satisfied is $\hat{v}_L(0) = 0$. In this region, the stability equation (1.62) can be written as

$$D\left\{\frac{(\bar{u} - \bar{u}_{max} - \delta^2 c_1) D\hat{v}_L - (D\bar{u})\hat{v}_L}{\bar{T} - M^2(\bar{u} - \bar{u}_{max} - \delta^2 c_1)^2}\right\} = \frac{\bar{u} - \bar{u}_{max} - \delta^2 c_1}{\bar{T}}\delta^6 \hat{v}_L. \tag{4.16}$$

The expansion

$$\hat{v}_L = \delta^L (v_{L0} + \ldots)$$

is made, where the amplitude δ^L will be determined relative to the amplitude in the regions I and R. At leading order in powers of δ, equation (4.16) has the general solution

$$v_{L0} = A_1(\bar{u} - \bar{u}_{max}) I_L + A_2(\bar{u} - \bar{u}_{max}), \tag{4.17}$$

where

$$I_L = \int_0^y \left[\frac{\bar{T}}{(\bar{u} - \bar{u}_{max})^2} - M^2\right] \mathrm{d}y,$$

and A_1 and A_2 are constants of integration. In order to satisfy the wall boundary condition $\hat{v}_L(0) = 0$, A_2 must be zero as $\bar{u} - \bar{u}_{max} \neq 0$ at $y = 0$. Taking the limit $y \to y_c^-$,

$$\hat{v}_L = \delta^L A_1 \left[-\frac{2\bar{T}_c}{3\lambda}(y - y_c)^{-1} + \left(\frac{4}{9}\frac{D^3 \bar{u}_c \bar{T}_c}{\lambda^2} - \frac{D\bar{T}_c}{\lambda}\right) + O(y - y_c)\right] + \cdots \tag{4.18}$$

This is now in a suitable form to match with the solution in Region I.

Region I

In this region $|y - y_c| \sim O(\delta)$. Defining $z = (y - y_c)/\delta$ and setting $\hat{v} = \hat{v}_I$ where

$$\hat{v}_I = \delta^I (v_{I0} + \cdots),$$

equation (4.15) yields, at leading order,

$$\frac{\mathrm{d}}{\mathrm{d}z}\left\{\left(\frac{1}{2}\lambda z^2 - c_1\right)\frac{\mathrm{d}v_{I0}}{\mathrm{d}z} - \lambda z v_{I0}\right\} \equiv \mathscr{L}_I\left\{v_{I0}\right\} = 0,$$

where the differential operator $\mathscr{L}_I$ has been introduced for later reference. The general solution for v_{I0} is given by

$$v_{I0} = B_1\left[\left(z^2+\Gamma\right)\arctan\left(\frac{z}{\sqrt{\Gamma}}\right) + z\sqrt{\Gamma}\right] + B_2\left[z^2+\Gamma\right], \tag{4.19}$$

where $\Gamma = -2c_1/\lambda$. To match with the solution (4.18) in region L the limiting form of (4.19) is considered as $z \to -\infty$,

$$v_{I0} \sim \left[-\frac{\pi}{2}B_1 + B_2\right]z^2 + \left[-\frac{\pi}{2}\Gamma B_1 + \Gamma B_2\right] + \left[-B_1\frac{2\Gamma^{3/2}}{3}\right]z^{-1} + \cdots. \tag{4.20}$$

By setting

$$B_2 = \frac{\pi}{2}B_1$$

the z^2 and constant terms in (4.20) are identically zero, thus allowing a match with the leading order behaviour of v_{L0}. This yields

$$\delta^L A_1\left(-\frac{2\bar{T}_c}{3\lambda}\right) = \delta^{I+1}B_1\left(-\frac{2\Gamma^{3/2}}{3}\right), \tag{4.21}$$

serving to determine the relative amplitude of the normal velocity in the two layers, and relating A_1 and B_1 via

$$B_1 = \frac{\bar{T}_c}{\lambda\Gamma^{3/2}}A_1. \tag{4.22}$$

With this expression, in the limit $z \to \infty$,

$$v_{I0} = \frac{A_1\pi\bar{T}_c}{\lambda\Gamma^{3/2}}z^2 + \frac{A_1\pi\bar{T}_c}{\lambda\Gamma^{1/2}} - \frac{2A_1\bar{T}_c}{3\lambda}z^{-1} + \ldots, \tag{4.23}$$

which will be used to match the solution in region R.

Region R

In a similar fashion to the analysis of region L, set $v_R = \delta^R v_{R0}$, and at leading order a general solution of (4.16) is obtained of the form

$$v_{R0} = C_1(\bar{u} - \bar{u}_{max})I_R + C_2(\bar{u} - \bar{u}_{max}), \tag{4.24}$$

where I_R denotes the integral

$$I_R = \int_y^\infty \left[\frac{\bar{T}}{(\bar{u} - \bar{u}_{max})^2} - M^2 \right] \mathrm{d}y.$$

The leading-term expansion of v_{R0} as $y \to y_c^+$ must match the leading term in the v_{I0} expansion as $z \to +\infty$. Noting that $(\bar{u} - \bar{u}_{max})\, I_R \sim O((y - y_c)^{-1})$ as $y \to y_c^+$, C_1 must be zero to match with the region I solution. Thus, the leading order behaviour of $\hat{v}_R$ as $y \to y_c^+$ is therefore

$$\hat{v}_R = \frac{1}{2}\delta^R C_2 \lambda\, (y - y_c)^2 + \ldots, \tag{4.25}$$

which will match with (4.23) if $\hat{v}_R \sim O\left(\delta^{I-2}\right)$ (i.e $R = I - 2$) and

$$C_2 = \frac{2\pi \bar{T}_c}{\lambda^2 \Gamma^{3/2}} A_1 \tag{4.26}$$

is chosen. From (4.24)

$$\hat{v}_R \sim \delta^R C_2 (1 - \bar{u}_{max}) + \ldots \quad \text{as} \quad y \to \infty, \tag{4.27}$$

where the condition that $\bar{u} \to 1$ as $y \to \infty$ is used.

To close the problem the far-field boundary condition (1.66) must be addressed. In order to consider this far-field region, a new stretched coordinate $\bar{y} = \delta^3 y$ is defined; at this scale the right-hand side of (1.62) enters at leading order. Taking the free stream values of the streamwise velocity and temperature, (1.66) reduces to

$$\frac{\mathrm{d}^2 \hat{v}_F}{\mathrm{d}\bar{y}^2} = \left(1 - M^2 \left(1 - \bar{u}_{max}\right)^2\right) \hat{v}_F, \tag{4.28}$$

which has a bounded solution (for a subsonic disturbance) given by

$$\hat{v}_F = F \exp\left(-\Omega \bar{y}\right), \tag{4.29}$$

where $\Omega^2 = 1 - M^2 \left(1 - \bar{u}_{max}\right)^2$. In the limit $\bar{y} \to 0$

$$\hat{v}_F \to F \left(1 - \Omega \bar{y} + \frac{\Omega^2}{2} \bar{y}^2 + \ldots\right), \tag{4.30}$$

and the solution will match with region R if

$$F = C_2 (1 - \bar{u}_{max}) \equiv A_1 \frac{2\pi \bar{T}_c}{\lambda^2 \Gamma^{3/2}} (1 - \bar{u}_{max}). \tag{4.31}$$

This constitutes an entire solution for $\hat{v}_F$. Since the equation for $\hat{v}$ is linear, without loss of generality, it is possible to take $\hat{v}_F \sim O(1)$, which then serves to determine the relative magnitudes of the disturbance amplitude in regions L, I and R. Hence $\hat{v}_R \sim O(1)$, $\hat{v}_I \sim O(\delta^2)$ and $\hat{v}_L \sim O(\delta^3)$.

The leading-order approximation for $\hat{v}$ in all regions is

$$\hat{v} \approx A_1 \begin{cases} \delta^3 (\bar{u} - \bar{u}_{max}) I_L & \text{for} \quad 0 < y < y_c, \\ \delta^2 \dfrac{\bar{T}_c}{\lambda \Gamma^{3/2}} \left[(z^2 + \Gamma) \left(\arctan \dfrac{z}{\sqrt{\Gamma}} + \dfrac{\pi}{2} \right) + z\sqrt{\Gamma} \right] & \text{for} \quad |y - y_c| \sim O(\delta), \\ \dfrac{2\pi \bar{T}_c}{\lambda^2 \Gamma^{3/2}} (\bar{u} - \bar{u}_{max}) & \text{for} \quad y > y_c. \end{cases} \tag{4.32}$$

Subsequent terms to the leading order solution are determined by first considering region I, where the series expansion terms of v_{L0} as $y \to y_c^-$ suggests that a suitable expansion for $\hat{v}_I$ is

$$\hat{v}_I = \delta^2 \left(v_{I0} + \delta v_{I1} + \delta^2 v_{I2} + \delta^3 \ln \delta \, v_{I3l} + \delta^3 v_{I3} + \ldots \right).$$

At $O(\delta^3)$, equation (4.15) yields

$$\mathscr{L}_I \{v_{I1}\} = D\bar{T}_c z - \frac{1}{6} D^3 \bar{u}_c z^6 \frac{\mathrm{d}}{\mathrm{d}z} \left(\frac{v_{I0}}{z^3} \right), \tag{4.33}$$

where the differential operator $\mathscr{L}_I$ was defined earlier. This equation admits the general solution

$$v_{I1} = \frac{2}{\lambda} B_4 \left(z^2 + \Gamma \right) - D\bar{T}_c B_3 + \frac{2}{3} \frac{D^3 \bar{u}_c \bar{T}_c^2}{\Gamma^{3/2}} A_1 z^3 \left(\arctan \frac{z}{\sqrt{\Gamma}} + \frac{\pi}{2} \right). \tag{4.34}$$

As $z \to -\infty$

$$v_{I1} \to \left[\frac{2}{\lambda} \left(B_4 - \frac{1}{6} \frac{A_1 D^3 \bar{u}_c \bar{T}_c}{\lambda \Gamma} \right) \right] z^2 + O\left(z^0\right). \tag{4.35}$$

In order to match with $\hat{v}_L$ the $O(z^2)$ term must vanish, serving to determine the constant B_4. The next term in this series expansion is now

$$v_{I1} \to \left[-B_3 \frac{D\bar{T}_c}{\lambda} + \frac{4}{9} \frac{A_1 D^3 \bar{u}_c \bar{T}_c}{\lambda^2} \right] z^0 + O\left(z^{-2}\right).$$

The z^0 term represents $\delta^3 (y - y_c)^0$ and can match to the second term of v_{L0} in (4.18), which serves to determine the other integration constant B_3. Subsequent terms in the v_{I1} series expansion as $z \to -\infty$ need to be matched with subsequent correction terms in $\hat{v}_L$.

As $z \to +\infty$,

$$v_{I1} \to \left[\frac{\pi}{3}\frac{A_1 D^3 \bar{u}_c \bar{T}_c}{\Gamma^{3/2}\lambda^2}\right] z^3 + O\left(z^0\right), \tag{4.36}$$

where the z^3 term represents $\delta^0 \left(y - y_c\right)^3$ and matches trivially to the $\left(y - y_c\right)^3$ term of v_{R0}. The z^0 term is $O\left(\delta^3\right)$ in region R and suggests that a correction term of this magnitude is required in the expansion of $\hat{v}_R$.

Region L

The largest unmatched terms of $\hat{v}_I$ as $z \to -\infty$ are the z^{-3} term in v_{I0} and the z^{-2} term in v_{I1}, both of which are $O(\delta^3)$ in region L. Letting

$$\hat{v}_L = \delta^3 \left(v_{L0} + \delta^2 v_{L1} + \ldots\right) \tag{4.37}$$

and substituting into (4.16) gives, at $O(\delta^3)$

$$D\left\{\mathscr{L}_O\left\{v_{L1}\right\} - \frac{c_1}{\left(\bar{u} - \bar{u}_{max}\right)^2 DI_L} Dv_{L0} - \frac{2M^2 c_1}{\left(\bar{u} - \bar{u}_{max}\right) DI_L}\mathscr{L}_O\left\{v_{L0}\right\}\right\} = 0, \tag{4.38}$$

where

$$\mathscr{L}_O\left\{v\right\} = \frac{\left(\bar{u} - \bar{u}_{max}\right) Dv - \left(D\bar{u}\right) v}{\bar{T} - M^2\left(\bar{u} - \bar{u}_{max}\right)^2} = D\left(\frac{v}{\bar{u} - \bar{u}_{max}}\right)\left(DI_L\right)^{-1}. \tag{4.39}$$

Solving for v_{L1} yields the general solution

$$\frac{v_{L1}}{\left(\bar{u} - \bar{u}_{max}\right)} = A_3 I_L + A_4 + A_1 c_1 \int_0^y \left[\frac{D\bar{u} I_L}{\left(\bar{u} - \bar{u}_{max}\right)^2} + \frac{DI_L}{\left(\bar{u} - \bar{u}_{max}\right)} + \frac{2M^2}{\left(\bar{u} - \bar{u}_{max}\right)}\right] \mathrm{d}y, \tag{4.40}$$

where A_3 and A_4 are constants of integration. In order to satisfy the wall boundary condition the constant A_4 must be chosen to be zero. The two leading terms in the expansion as $y \to y_c^-$ match identically without additional constraints. The other integration constant A_3 appears in the $(y - y_c)^{-1}$ term of the expansion as $y \to y_c^-$, which is of size $\delta^2 z^{-1}$ in Region I and hence needs to be matched with a z^{-1} term in v_{I2}, which is yet to be determined.

Region R ($y \gg y_c$)

The largest unmatched term of $\hat{v}_I$ as $z \to +\infty$ is the z^0 term in v_{I0}, which is $O\left(\delta^2\right)$ in Region R. Extending the series to

$$\hat{v}_R = v_{R0} + \delta^2 v_{R1} + \delta^3 v_{R2} + \cdots \tag{4.41}$$

an equation similar to that of v_{L1} is obtained, for v_{R1}

$$D\left\{\mathscr{L}_O\left\{v_{R1}\right\} - \frac{c_1}{\left(\bar{u}-\bar{u}_{max}\right)^2 DI_R} Dv_{R0} - \frac{2M^2 c_1}{\left(\bar{u}-\bar{u}_{max}\right) DI_R}\mathscr{L}_O\left\{v_{R0}\right\}\right\} = 0. \quad (4.42)$$

This has the general solution

$$v_{R1} = C_3\left(\bar{u}-\bar{u}_{max}\right) I_R + C_4\left(\bar{u}-\bar{u}_{max}\right) - C_2 c_1, \quad (4.43)$$

where the constant C_3 must be zero to ensure the largest term is of the correct form to match with v_{I1}. As was the case with v_{L1}, the other constant of integration C_4 cannot be determined without reference to v_{I2}.

4.2.2 The Second-Order Correction

Region I

At $O\left(\delta^2\right)$, equation (4.15) yields

$$\mathscr{L}_I\left\{v_{I2}\right\} = B_5\frac{1}{2}D^2\bar{T}_c z^2 - \frac{1}{6}D^3\bar{u}_c z^6\frac{\mathrm{d}}{\mathrm{d}z}\left(\frac{v_{I1}}{z^3}\right) - \frac{1}{24}D^4\bar{u}_c z^8\frac{\mathrm{d}}{\mathrm{d}z}\left(\frac{v_{I0}}{z^4}\right). \quad (4.44)$$

As $z \to -\infty$, the largest terms of v_{I2} are z^2, z^1 and z^{-1}, which in region L are $O(\delta^0)$, $O(\delta)$ and $O(\delta^3)$ respectively. The z^2 has no corresponding term to match to in region L and so must vanish, thus serving to determine one constant of integration. The other constant is set by matching the z^1 term with v_{L0}. The z^{-1} term is matched with the $\left(y-y_c\right)^{-1}$ term in v_{L1}, which yields $A_3 = 0$.

As $z \to +\infty$, v_{I2} has a z^4 term, a z^2 term and lower order terms. The z^4 term is $O(\delta^0)$ and matches trivially with v_{R0}. The z^2 term is $O(\delta^2)$ and matching with the $\left(y-y_c\right)^2$ term in v_{R1} serves to determine C_4

$$C_4 = A_1\frac{\pi}{12\lambda^4\sqrt{\Gamma}}\left(5D^3\bar{u}_c^2\bar{T}_c - 12\lambda D^3\bar{u}_c D\bar{T}_c + 12\lambda^2 D^2\bar{T}_c - 3\lambda D^4\bar{u}_c\bar{T}_c\right). \quad (4.45)$$

Region R

In order to determine the eigenvalue correction term c_1, the solution for v_{R2} is required. The equation and solution is the same as that for v_{R0}

$$v_{R2} = C_5\left(\bar{u}-\bar{u}_{max}\right) I_R + C_6\left(\bar{u}-\bar{u}_{max}\right), \quad (4.46)$$

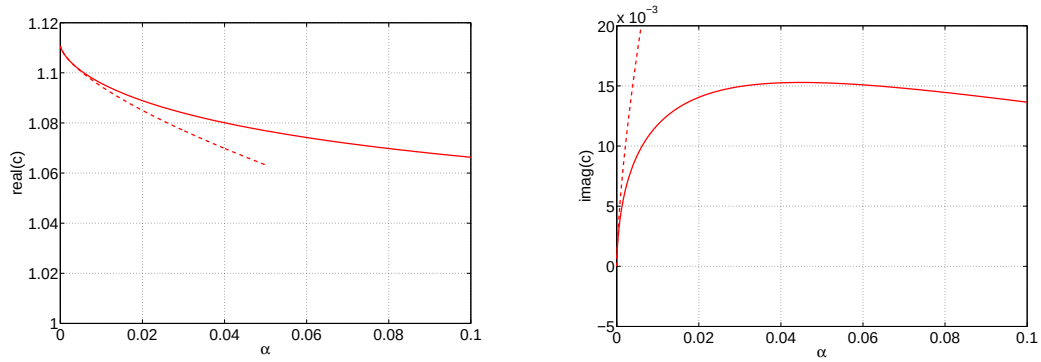

(a) Real part (b) Imaginary part

Figure 4.1: Approximation for low wavenumber correction (dashed line) compared with numerical eigenvalues (solid) of the new unstable mode for boundary-layer case 4 ($M = 8$, $g_w = 1.3$, $\beta = 1.3$.

however unlike v_{R0} the first term is kept, as it can be matched with the z^{-1} term in v_{I0}, and in fact $C_5 \equiv A_1$. As $y \to \infty$

$$v_{R2} \to \left(\frac{1}{(1 - \bar{u}_{max})^2} - M^2 \right) y. \tag{4.47}$$

This term, when matched with the $\bar{y}$ term of $\hat{v}_F$, serves to determine c_1

$$c_1^3 = -\frac{\pi^2 \bar{T}_c^2 (1 - \bar{u}_{max})^6}{2\lambda^3 \left(1 - M^2 (1 - \bar{u}_{max})^2\right)}. \tag{4.48}$$

Provided that the maximum boundary-layer velocity is subsonic (in a Lees-Lin sense), the right-hand side of equation (4.48) is always positive and the solutions for c_1 consist of a positive real solution, and a complex conjugate pair whose real component is negative. It is this complex conjugate pair that corresponds to the new family of unstable modes. The nature of the inviscid stability equations is such that both the true inviscid eigenvalue and its conjugate are valid eigenvalues; the correct eigenvalue can only be determined by the high-R limit of the viscous stability equations. In figure 4.1 the approximation $c = \bar{u}_{max} + \alpha^{2/3} c_1$ is plotted against numerically determined eigenvalues for comparison.

In the case where the maximum boundary-layer velocity is supersonic (greater than $1 + 1/M$), the right-hand side of equation (4.48) is now positive and any adjacent unstable modes have an increasing real wavespeed, thus becoming more supersonic. There is no numerical evidence of corresponding unstable modes exist-

ing. As the maximum boundary-layer velocity becomes supersonic, the numerical solutions suggest the behaviour of the new low-wavenumber mode changes from approaching $c = \bar{u}_{max}$ to approaching $c = 1+1/M$. The right hand side of equation (4.48) has an algebraic singularity when $\bar{u}_{max}$ passes $1+1/M$, so there may be some additional behaviour as this occurs that is not accounted for in the above analysis, perhaps when $D\bar{u}_c$ is small but becomes asymptotically important. This could facilitate the transfer of the new low-wavenumber mode at $c = \bar{u}_{max}$ to the already well-established (i.e. Mack, 1969) low-wavenumber neutral mode with $c = 1+1/M$.

4.3 Inflectional Neutral Mode

For non-overshoot boundary layers, a generalised point of inflection (1.69) in the boundary layer acts to remove the singularity at a critical point located precisely at the same point. Consequently, a neutral mode solution with a wavespeed equal to the velocity at the generalised point of inflection (inflectional velocity) exists and serves to neutralise the unstable modes for a discrete series of wavenumbers (Mack, 1969).

The velocity profiles of overshoot boundary layers are not monotonic, so for neutral wavespeeds between unity and the velocity maximum, there are two critical points where $\bar{u} = c$, on either side of the velocity maximum. In figures 2.8 and 2.9 it was demonstrated that it is possible for generalised points of inflection to occur at points where the inflectional velocity is greater than unity. For such a neutral wavespeed there are two critical points, but only one of these is regularised by the generalised point of inflection. At the other critical point, the inviscid eigenfunction contains a singularity. In figure 4.2 the location of the generalised points of inflection for boundary-layer case 4 are presented, along with the location of critical layers for the corresponding wavespeeds – in both cases the inflectional velocity is greater than unity.

Despite the presence of a singularity, there appears to be no noticeable qualitative change in behaviour of the neutral-mode solutions as the boundary-layer parameters are varied to move a generalised point of inflection into the overshoot

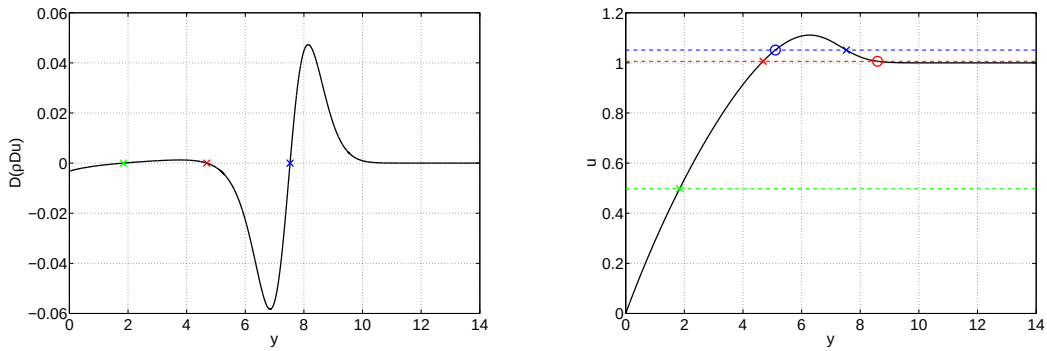

(a) Distribution of $D(\bar{\rho}D\bar{u})$

(b) Boundary-layer velocity profile

Figure 4.2: Location of inflectional critical points (crosses) and non-inflectional critical points (circles) for boundary-layer case 4

region. For example, the boundary layers used to generate the data for figures 3.10 and 3.11 span a case where the inflectional velocity decreases from above to below unity. In both cases this inflectional velocity is associated with the neutralisation of the first downstream family. In addition, these boundary layers have another inflectional point at which the streamwise velocity is greater than unity and this corresponds with the neutralisation of the third mode.

At the second, non-inflectional critical point, the eigenfunctions contain a singularity and the solution is necessarily viscous there. The employment of a complex contour around critical points (inflectional or not) in the inviscid numerical calculations ensures that this singularity is not encountered, but it remains to examine the viscous calculations to ensure that such neutral modes are indeed valid in the large-R limit. This is accomplished in Chapter 5.

As the Mach number increases for an overshoot boundary layer, the inflectional velocities surpass the downstream sonic velocity $1 + 1/M$ and are thus supersonic. A similar case is observed by Mack (1987) for cooled-wall boundary layers where the inflectional velocities decrease below $1 - 1/M$. In this scenario, the inflectional neutral modes cease to exist and the second mode remains unstable to an (unknown) upper wavenumber limit, albeit with monotonically decreasing amplification rates. In the present scenario, this is not the case and the higher modes still appear to be neutralised, but at a supersonic, non-inflectional velocity. The nu-

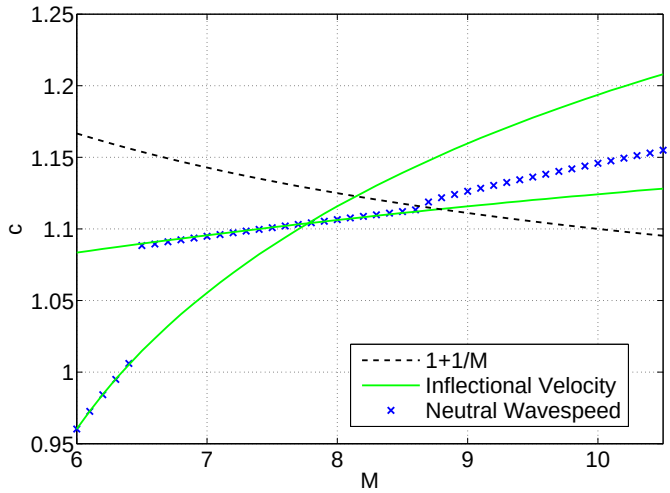

Figure 4.3: Neutral wavespeed of upstream family as compared to inflectional velocities for boundary-layer case 6 with variable Mach number ($g_w = 1.5$, $\beta = 0.7$).

merical methods employed here are unable to determine damped eigenvalues past the neutral point, but it is possible to get arbitrarily close to this neutral point.

In figure 4.3 the wavespeed at the neutral point is plotted along with the inflectional velocities and the sonic velocity $1 + 1/M$. At $M = 6.5$ and below, the upstream family contains only the first mode and is neutralised at the lower inflectional velocity. At higher Mach numbers, the upstream family picks up the second mode and becomes neutral at a higher inflectional velocity. As this inflectional velocity increases beyond $1 + 1/M$, there is a clear change in behaviour and the neutral wavespeed no longer corresponds to the value of the streamwise velocity at the generalised point of inflection.

4.4 The Non-Inflectional Neutral Mode

The new low-wavenumber neutral mode analysed in section 4.2 marks the beginning of a set of unstable-mode solutions that are neutralised at a wavespeed not corresponding to any of the inflectional velocities. This can be seen in figure 3.7 where the neutral wavespeed for the new mode is clearly between the two inflectional velocities. This non-inflectional neutral wavespeed been referred to elsewhere

in this thesis as c_m. Like the inflectional velocities, the value of c_m appears to be set by the properties of the boundary layer; it varies smoothly with small parameter changes and in some cases (i.e. figure 3.12) corresponds to neutral modes at multiple wavenumbers. It always has a value greater than unity and hence this neutral mode has two, non-inflectional critical points. This neutral mode (and indeed the whole unstable region) disappears when c_m becomes supersonic.

While a comprehensive analysis has not been undertaken it is postulated that as $D(\bar{\rho}D\bar{u})$ has opposite signs at the two critical points, and because the sign of this quantity at critical points corresponds with energy gain and loss (Lees and Lin, 1946) this neutral mode corresponds to a case where the net energy gain over the two critical points is zero.

4.5 Stabilisation of First Mode

In figure 3.14 the upstream low-wavenumber neutral mode has no neighbouring unstable solutions, so the first mode is completely stabilised. In the non-overshoot boundary layer case, the first mode becomes stable at the single inflectional velocity. Velocity overshoot has the potential to add additional generalised points of inflection, and modify their location and velocity.

With reference to figures 2.8 and 2.9 where M and g_w are held constant and β is increased from zero; the point of inflection responsible for neutralisation of the first-mode is represented by the green curve. Depending on the boundary-layer parameters, this generalised point of inflection may disappear (former case), or not (latter case). In figure 4.4 the neutral wavespeed of the first-mode disturbance is plotted along with the inflectional velocities for the former case. In this case for all β values, the upstream family contains only the first-mode disturbance. As β is increased, the neutral wavespeed follows the inflectional velocity. As the upstream family commences at $\alpha = 0$, $c = 1-1/M$, the reduction in the inflectional velocity reduces the neutral wavenumber (and consequently, the maximum growth rate) until the inflectional velocity decreases below $1 - 1/M$. After this occurs at $\beta \approx 0.15$ there are no unstable first mode solutions.

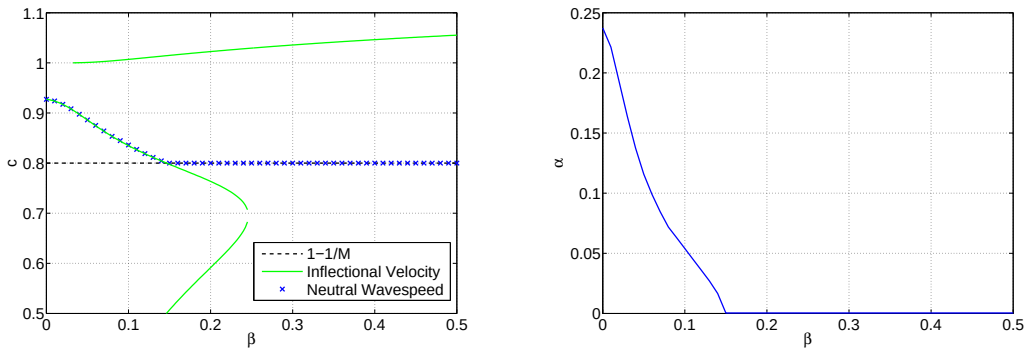

(a) Neutral wavespeed

(b) Neutral wavenumber

Figure 4.4: Neutral modes of first-mode disturbance for boundary-layers with $M = 5$, $g_w = 1.5$ and variable β.

4.6 Oblique Two-Dimensional Disturbances

In this section, inviscid disturbances propagating at an angle to the base boundary-layer flow (oblique disturbances) are considered. For flat-plate, non-overshoot boundary layers, the first mode is most unstable for oblique disturbances, whereas the second and higher modes are most unstable as two-dimensional disturbances (Mack, 1969).

4.6.1 First-Mode and Higher-Mode Disturbances

In terms of a wave travelling at angle ψ to the boundary layer, the upstream zero-wavenumber neutral mode has a wavespeed of $\cos\psi - 1/M$ and the first mode has a neutral wavespeed of $c_{s1}\cos\psi$, where c_{s1} is the inflectional velocity associated with the first mode (see the green curve in figures 2.7-2.9). The range of real wavespeeds the disturbance may attain has a width of $\cos\psi(c_s - 1) + 1/M$. When c_{s1} is less than unity (as is always the case for the non-overshoot case), this width increases with increasing ψ and corresponds to higher growth rates which diminish as ψ approaches 90° where the growth rate is zero at this point.

When c_{s1} is greater than unity, the range of wavespeeds decreases with increasing ψ, and the first mode disturbance is expected to be most unstable as a two-dimensional disturbance. However, cases where c_{s1} is greater than unity have

high Mach numbers and the first mode merges with the higher modes before it reaches its maximum growth rate; no changes to the first-mode growth rate are apparent. The second mode is dominant here and the strong reduction in growth rate with increasing ψ would be expected to have an overall stabilising effect.

When c_{s1} does not exist (i.e. in boundary-layer case 7) the first mode is completely stabilised to both two-dimensional (as in figure 3.14) and oblique disturbances.

4.6.2 New-Mode Disturbances

The zero-wavenumber new neutral mode is first considered. For an oblique disturbance, the maximum boundary-layer velocity in the direction of the disturbance is $\bar{u}_{max}\cos\psi$ and the downstream sonic velocity is $\cos\psi + 1/M$. The maximum velocity is subsonic for an oblique disturbance if

$$\bar{u}_{max} < 1 + \frac{1}{M\cos\psi},$$

thus even if the maximum velocity is supersonic for two-dimensional disturbances, sufficiently oblique disturbances may be subsonic.

The new mode is stabilised at the neutral wavespeed $c_m\cos\psi$ where c_m is a property of the boundary layer and is not affected by the disturbance angle ψ. For cases where the maximum velocity is subsonic, the new mode has the oblique disturbance character of the higher modes and hence could be expected to be most unstable as a two-dimensional disturbance. However, this is not the case. In figure 4.5 numerical solutions are presented for a typical boundary layer with moderate overshoot. The maximal growth rate occurs at $\psi \approx 30°$, although it is less than 5% higher than the two-dimensional maximum growth rate.

When the maximum velocity is supersonic and the zero-wavenumber new mode has a wavespeed equal to the downstream sonic velocity, the characteristics of the oblique disturbance is expected to match that of the first mode; for which oblique modes are most unstable. Figure 4.6 illustrates that this is indeed the case, and the maximal growth rate at $\psi \approx 60°$ is a factor of four larger than the two-dimensional maximum growth rate.

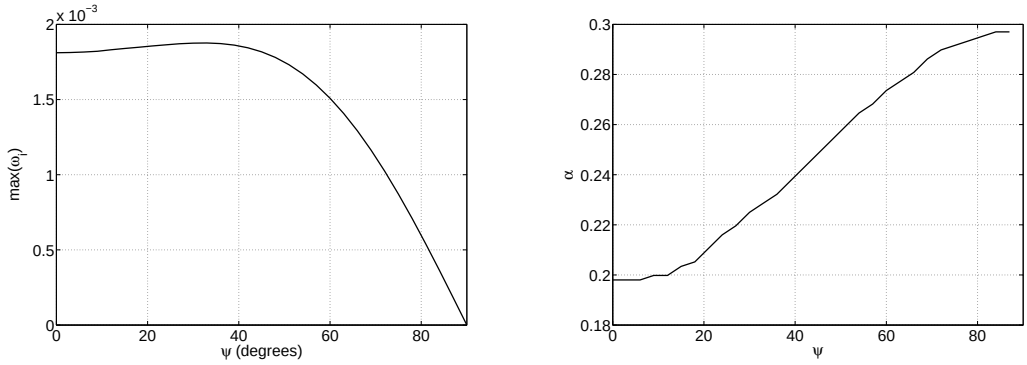

(a) Maximum growth rate (b) Wavenumber at maximum growth rate

Figure 4.5: Maximum growth rates for oblique new-mode disturbances for boundary-layer case 4 ($M = 8$, $g_w = 1.3$, $\beta = 0.3$).

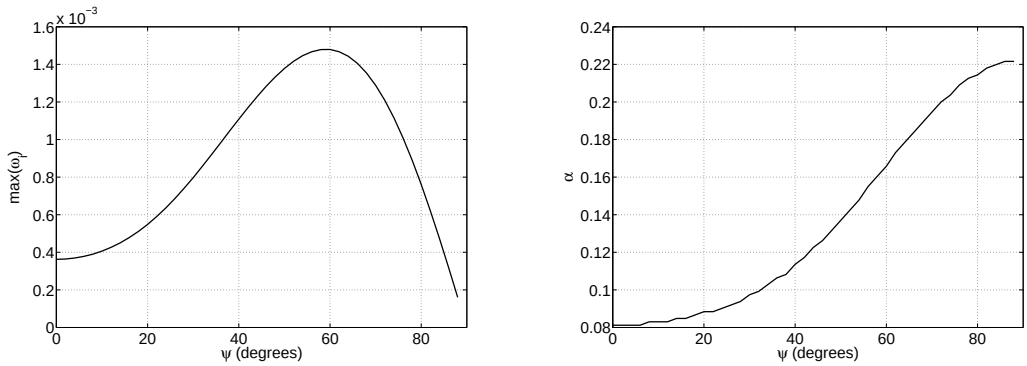

(a) Maximum growth rate (b) Wavenumber at maximum growth rate

Figure 4.6: Maximum growth rates for oblique new-mode disturbances for boundary-layer case 5 ($M = 7$, $g_w = 1.5$, $\beta = 1$).

4.7 Summary

In this chapter the numerical inviscid stability results of chapter 3 have been examined and discussed. The existence of a new low-wavenumber subsonic neutral mode associated with a new unstable region is established analytically. The finite-wavenumber neutral mode that closes the new mode's unstable region has two critical layers and is non-inflectional. A possible physical explanation for this behaviour is suggested. The consequences of velocity overshoot for the classical inflectional neutral mode are discussed, including the cases where there are two critical layers. When the Mach number is increased, these neutral mode disturbances may become supersonic relative to the freestream and this changes their nature. It is possible for the classical first-mode disturbance to be damped at all wavenumbers for certain overshoot boundary layers.

Chapter 5

Viscous Analysis of Overshoot Boundary Layers

The inviscid analysis presented in Chapter 4 provides a number of interesting paths for further investigation. Given the singular nature of the inviscid stability problem and the ambiguous sign of the imaginary part of the temporal eigenvalue c, it is reasonable to proceed by considering the extension of the results so far to include the effect of viscosity and so further establish that the validity of the inviscid solutions presented. As well as providing confirmation of the inviscid results, viscous stability results can be applied to transition-prediction algorithms.

5.1 Large Reynolds Number Analysis

The viscous stability equations (1.37) are singular in the large R limit. For a neutral disturbance the inviscid equations are singular at points where $\bar{u} = c$, unless this also occurs at a generalised point of inflection defined by (1.69). In this section linearly independent solutions to the viscous stability equations in the large R limit are established and the two that provide an appropriate match with the inviscid solutions are identified. The conditions under which the corresponding viscous solutions match with the inviscid solutions are demonstrated. This analysis is motivated by the work of Lees and Lin (1946) and is extended to cover the conditions of the non-monotonic boundary-layer profiles that are of interest here.

Concentration here is on the two-dimensional case ($\bar{w} \equiv 0$ and $\zeta = 0$), although it can be extended to oblique disturbances using the relations (1.49) and (1.50). The small parameter $\epsilon = (\alpha R)^{-n}$ is taken, where n is positive and will be determined a posteriori. The viscous stability equations are transformed to the co-ordinate $z = \epsilon^{-1}(y - y_c)$ to examine the structure of the critical layer and the following equations are obtained,

$$\begin{aligned}\mathfrak{D}^2\hat{u} = &\left[i\epsilon^{\left(2-\frac{1}{n}\right)}\frac{\bar{u}-c}{\bar{T}} + \epsilon^2\alpha^2\right]\hat{u} - \epsilon\frac{D\bar{T}}{T}\mathfrak{D}\hat{u} + \left[\epsilon^{\left(2-\frac{1}{n}\right)}\frac{D\bar{u}}{\alpha\bar{T}^2} - 2\epsilon^2 i\alpha\frac{D\bar{T}}{\bar{T}}\right]\hat{v} \\ &+ \left[\epsilon^{\left(2-\frac{1}{n}\right)}\frac{i}{\bar{T}} - \epsilon^2\alpha^2\gamma M^2(\bar{u}-c)\right]\hat{p} + \epsilon^2\left[\alpha^2\frac{\bar{u}-c}{\bar{T}} - \frac{D^2\bar{u}}{\bar{T}}\right]\hat{T} - \epsilon\frac{D\bar{u}}{\bar{T}}\mathfrak{D}\hat{T},\end{aligned} \tag{5.1}$$

$$\mathfrak{D}\hat{v} = -\epsilon i\alpha\hat{u} + \epsilon\frac{D\bar{T}}{T}\hat{v} - \epsilon i\alpha\gamma M^2(\bar{u}-c)\hat{p} + \epsilon i\alpha\frac{\bar{u}-c}{\bar{T}}\hat{T}, \tag{5.2}$$

$$\begin{aligned}\mathfrak{D}\hat{p} = &-4\epsilon i\alpha\frac{D\bar{T}}{T}\chi\hat{u} - i\alpha\chi\mathfrak{D}\hat{u} - \left[\epsilon^{\left(1-\frac{1}{n}\right)}i\alpha\frac{\bar{u}-c}{\bar{T}^2}\chi + \epsilon\alpha^2\chi - \epsilon\frac{2\left(D\bar{T}\right)^2}{\bar{T}^2} - \epsilon\frac{2D^2\bar{T}}{\bar{T}}\chi\right]\hat{v} \\ &- \epsilon i\alpha\gamma M^2\chi\left[\frac{4(\bar{u}-c)D\bar{T}}{\bar{T}} + 2D\bar{u}\right]\hat{p} \\ &+ \epsilon i\alpha\chi\left[\frac{3D\bar{u}}{\bar{T}} + \frac{2(\bar{u}-c)D\bar{T}}{\bar{T}^2}\right]\hat{T} + \left[i\alpha\frac{2(\bar{u}-c)}{\bar{T}}\chi\right]\mathfrak{D}\hat{T},\end{aligned} \tag{5.3}$$

$$\begin{aligned}\mathfrak{D}^2\hat{T} = &-2\epsilon Pr(\gamma-1)M^2D\bar{u}\mathfrak{D}\hat{u} + \left[\epsilon^{\left(2-\frac{1}{n}\right)}\left(\frac{Pr}{\alpha}\frac{D\bar{T}}{\bar{T}^2}\right) - 2\epsilon^2 i\alpha Pr(\gamma-1)M^2D\bar{u}\right]\hat{v} \\ &- \epsilon^{\left(2-\frac{1}{n}\right)}iPr(\gamma-1)M^2\frac{\bar{u}-c}{\bar{T}}\hat{p} \\ &+ \left[\epsilon^{\left(2-\frac{1}{n}\right)}iPr\frac{\bar{u}-c}{\bar{T}^2} + \epsilon^2\left(Pr(\gamma-1)M^2\frac{D\bar{u}^2}{\bar{T}} - \frac{D^2\bar{T}}{\bar{T}^2}\right)\right]\hat{T} - \epsilon\frac{2}{\bar{T}}\mathfrak{D}\hat{T},\end{aligned} \tag{5.4}$$

where $\mathfrak{D}$ denotes differentiation with respect to z. The correct choice of n depends on the nature of the critical point; if $c = \bar{u}_{max}$ then $D\bar{u}_c$ is zero and the behaviour is different. These cases are considered separately in the following sections.

5.1.1 Case 1: $c \neq \bar{u}_{max}$

In this case, $(\bar{u} - c) \sim O(\epsilon)$, $\chi \sim O\left(\epsilon^{1/n}\right)$ and $n = \frac{1}{3}$ is found to be the correct choice from as the distinguished limit using a dominant-balance argument. In

seeking power-series solutions of the form

$$\hat{u} \sim \epsilon^{-1}\left(u_0 + (\epsilon \ln \epsilon) u_{1L} + \epsilon u_1 + \ldots\right)$$

$$\hat{v} \sim v_0 + (\epsilon \ln \epsilon) v_{1L} + \epsilon v_1 + \ldots$$

$$\hat{p} \sim p_0 + (\epsilon \ln \epsilon) p_{1L} + \epsilon p_1 + \ldots$$

$$\hat{T} \sim \epsilon^{-1}\left(T_0 + (\epsilon \ln \epsilon) T_{1L} + \epsilon T_1 + \ldots\right),$$

then from equations (5.1)-(5.4) the leading-order equations are

$$\mathfrak{D}^3 u_0 - i\alpha z \frac{D\bar{u}_c}{T_c} \mathfrak{D} u_0 = 0, \tag{5.5}$$

$$\mathfrak{D} v_0 + i\alpha u_0 = 0, \tag{5.6}$$

$$\mathfrak{D} p_0 = 0, \tag{5.7}$$

$$\mathfrak{D}^2 T_0 - i\alpha Pr \frac{D\bar{u}_c}{\bar{T}_c^2} z T_0 = Pr \frac{D\bar{T}_c}{\bar{T}_c^2} v_0. \tag{5.8}$$

Using equation (5.6) in equation (5.5) an Airy equation for $\mathfrak{D}^2 v_0$ is obtained and a set of linearly independent solutions must be chosen that are numerically satisfactory (using the terminology of Miller, 1950) on both sides of the turning point. For the case of a neutral disturbance, $D\bar{u}_c$ is real and suitable solutions for $D\bar{u}_c \gtrless 0$ are

$$\mathfrak{D}^2 v_0 = C_1 \mathrm{Ai}\left(K_u z\right) + C_2 \mathrm{Ai}\left(K_u z e^{\pm \frac{2\pi i}{3}}\right) \tag{5.9}$$

where C_1, C_2 are integration constants,

$$K_u = \left(\frac{i\alpha D\bar{u}_c}{\bar{T}_c^2}\right)^{\frac{1}{3}}$$

and have arguments

$$\arg K_u = \pm \frac{\pi}{6}$$

depending on whether $D\bar{u}_c \gtrless 0$. These comprise of 4 of the 6 linearly-independent solutions for v_0, which are denoted

$$v_0^{(A)} = z$$

$$v_0^{(B)} = 1$$

$$v_0^{(C)} = \int_{\infty}^{z} \int_{\infty}^{z^*} \mathrm{Ai}\left(K_u z'\right)\ \mathrm{d}z'\ \mathrm{d}z^*$$

$$v_0^{(D)} = \int_{-\infty}^{z} \int_{-\infty}^{z^*} \mathrm{Ai}\left(K_u z' e^{\pm\frac{2\pi i}{3}}\right)\ \mathrm{d}z'\ \mathrm{d}z^*.$$

The remaining two linearly-independent solutions, $v_0^{(E)}$ and $v_0^{(F)}$ are zero and correspond to the homogeneous solutions of equation (5.8). Recalling the inviscid solutions from section 4.1.2, the linearly-independent inviscid solutions are

$$v_I^{(A)} = z + \epsilon \frac{1}{2} \frac{D^2 \bar{u}_c}{D\bar{u}_c} z^2 + \cdots, \tag{5.10}$$

$$v_I^{(B)} = 1 + \epsilon \frac{\bar{T}_c}{D\bar{u}_c} D\left(\frac{D\bar{u}}{\bar{T}}\right)_c z\left(\ln z + \ln \epsilon\right) + \cdots, \tag{5.11}$$

which match (to leading order) with the corresponding (A) and (B) viscous solutions. From (5.6) and (5.7), $u_0^{(A)} = 1$, $u_0^{(B)} = 0$, $p_0^{(A)} = 0$ and $p_0^{(B)} = 1$. Equation (5.8) is less trivial and requires finding particular solutions. The first gives $T_0^{(A)} = 1$. The second can be written as

$$\frac{\mathrm{d}^2 T_0^{(B)}}{\mathrm{d}{z_T}^2} - z_T T_0^{(B)} = v_0^*, \tag{5.12}$$

where $z_T = K_T z$,

$$K_T = \left(i\alpha Pr \frac{D\bar{u}_c}{\bar{T}_c}\right)^{\frac{1}{3}}$$

has the same argument as K_u, and v_0^* is a constant. The particular solution is determined using a variation of parameters approach

$$\frac{T_0^{(B)}}{v_0^* \pi} = -\mathrm{Ai}\left(z_T\right) \int_{-\infty}^{z_T} \mathrm{Ai}\left(t e^{\pm\frac{2\pi i}{3}}\right)\ \mathrm{d}t + \mathrm{Ai}\left(z_T e^{\pm\frac{2\pi i}{3}}\right) \int_{\infty}^{z_T} \mathrm{Ai}\left(t\right)\ \mathrm{d}t, \tag{5.13}$$

with the two solutions corresponding to the cases $D\bar{u}_c \gtrless 0$. Using series representations for large $|z_T|$, given that $|\arg K_u| < \pi/3$,

$$T_0^{(B)} \sim \frac{1}{z_T} + O\left(z_T^{-7/4}\right)$$

as $z \to \pm\infty$.

Now the matching of the next order terms in the viscous series expansion are considered. At the next order $O(\epsilon \ln \epsilon)$ the equations are of the same form as equations (5.5)-(5.8) and

$$v_{1L}^{(A)} = 1$$

$$v_{1L}^{(B)} = z$$

correspond to the inviscid solutions. At order $O(\epsilon)$ the equations for u_1 and v_1 are

$$\begin{aligned}\mathfrak{D}^3 u_1 - i\alpha \frac{D\bar{u}_c}{D\bar{T}_c^2} z\mathfrak{D}u_1 = &-\frac{D\bar{T}_c}{\bar{T}_c}\mathfrak{D}^2 u_0 + \frac{D^2\bar{u}_c T_c - 2D\bar{u}_c D\bar{T}_c}{\bar{T}_c^3} v_0 \\ &+ \frac{\alpha\left(T_c D^2\bar{u}_c - 4D\bar{u}_c D\bar{T}_c\right)}{\bar{T}_c^2} z\mathfrak{D}v_0 \\ &+ \frac{D^2\bar{u}_c\bar{T}_c - 4D\bar{u}_c D\bar{T}_c}{2\bar{T}_c^3} z^2\mathfrak{D}^2 v_0 - i\alpha\frac{D\bar{T}_c}{\bar{T}_c^2} p_0 - \frac{D\bar{u}_c}{\bar{T}_c}\mathfrak{D}^2 T_0,\end{aligned} \tag{5.14}$$

$$\mathfrak{D}v_1 + i\alpha u_1 = \frac{D\bar{T}_c}{\bar{T}_c} v_0 + i\alpha\frac{D\bar{u}_c}{\bar{T}_c} zT_0. \tag{5.15}$$

The first solution corresponds to the particular solution of

$$\mathfrak{D}^3 u_1^{(A)} - i\alpha\frac{D\bar{u}_c}{D\bar{T}_c^2} z\mathfrak{D}u_1^{(A)} = u_1^* z, \tag{5.16}$$

where u_1^* is a constant. This is qualitatively the same as the equation for $T_0^{(A)}$ and gives $\mathfrak{D}u_1^{(A)} = 1$, or $u_1^{(A)} = z$. Equation (5.15) then gives $v_1^{(A)} = z^2$ which is of an appropriate form to match with the $O(\epsilon)$ term of $v_I^{(A)}$. The second solution corresponds to, after using (5.8) to replace $\mathfrak{D}^2 T_0$, a particular solution of

$$\mathfrak{D}^3 u_1^{(B)} + i\alpha\mathfrak{D}u_1^{(B)} = v_0^c + T_0^* zT_0, \tag{5.17}$$

where v_0^c and T_0^* are constants. As $|z| \to \infty$, $T_0^{(B)} \sim 1/z$ and hence

$$\mathfrak{D}u_1^{(B)} \sim T_0^{(B)}, \tag{5.18}$$

$$\mathfrak{D}v_1^{(B)} \sim \ln z + O(1), \tag{5.19}$$

and $v_1^{(B)}$ has the required $z\ln z$ behaviour to match with $v_I^{(B)}$ as $|z| \to \infty$.

Global Analysis

The above approach covers the region where $|y - y_c| \sim O((\alpha R)^{-1/3})$. Now the effect of a high Reynolds number on the global structure of the viscous solutions is considered by seeking solutions of the WKBJ type. The small parameter $\epsilon = (\alpha R)^{-1/2}$ is chosen and the outer expansions are

$$\hat{u} \sim \exp\left[\frac{1}{\epsilon}\left(S_{u0}(y) + \epsilon S_{u1}(y) + \dots\right)\right],$$

$$\hat{v} \sim \exp\left[\frac{1}{\epsilon}\left(\epsilon S_{v1}(y) + \dots\right)\right],$$
$$\hat{p} \sim \exp\left[\frac{1}{\epsilon}\left(\epsilon S_{p1}(y) + \dots\right)\right],$$
$$\hat{T} \sim \exp\left[\frac{1}{\epsilon}\left(S_{T0}(y) + \epsilon S_{T1}(y) + \dots\right)\right].$$

Here $S_{v0}(y)$ and $S_{p0}(y)$ have been taken to be zero; the first outer approximations for $\hat{v}$ and $\hat{p}$ are the two inviscid solutions when $\epsilon = 0$. The remaining four first approximations are of the form

$$(\bar{u} - c)^{-5/4} \exp\left[\pm (\alpha R)^{1/2} \int_{y_c}^{y} \left(\frac{i}{\bar{\mu}\bar{T}}(\bar{u} - c)\right)^{\frac{1}{2}} \mathrm{d}y^*\right], \tag{5.20}$$

$$(\bar{u} - c)^{-5/4} \exp\left[\pm (\alpha R)^{1/2} \int_{y_c}^{y} \left(\frac{iPr}{\bar{\mu}\bar{T}}(\bar{u} - c)\right)^{\frac{1}{2}} \mathrm{d}y^*\right]. \tag{5.21}$$

By taking the approximation $\bar{u} - c = D\bar{u}_c(y - y_c)$ the integral

$$I(y) = \int_{y_c}^{y} \left(\frac{i}{\bar{\mu}\bar{T}}(\bar{u} - c)\right)^{\frac{1}{2}} \mathrm{d}y^* \sim (iD\bar{u}_c)^{\frac{1}{2}} (y - y_c)^{\frac{3}{2}}$$

is multiple valued and hence may only apply over an open sector in $(y - y_c)$ space of angle $4\pi/3$. In considering the connection of the global WKBJ solutions with the local critical layer solution, the sectors chosen are

$$-\frac{7\pi}{6} < \arg(y - y_c) < \frac{\pi}{6} \quad \text{for } D\bar{u}_c > 0,$$
$$-\frac{\pi}{6} < \arg(y - y_c) < \frac{7\pi}{6} \quad \text{for } D\bar{u}_c < 0,$$

so that the Airy equation solutions chosen in the critical layer are a dominant-recessive pair. Now, $I(y)$ has anti-Stokes lines at

$$\arg(y - y_c) = \left(-\frac{7\pi}{6}, -\frac{\pi}{2}, \frac{\pi}{6}\right) \quad \text{for } D\bar{u}_c > 0,$$
$$\arg(y - y_c) = \left(-\frac{\pi}{6}, \frac{\pi}{2}, \frac{5\pi}{6}\right) \quad \text{for } D\bar{u}_c < 0,$$

and it is easy to show that between these rays within the validity region of $y - y_c$, $\exp[\pm I(y)]$ form a dominant-recessive pair.

The connection between the validity regions (in terms of ϵ) for the WKBJ and critical layer solutions (the so-called overlap region) is not examined here but the

reader is referred to Drazin (2004) for analysis of the incompressible case with $D\bar{u}_c > 0$. Drazin shows that the two solutions can be made identical in an overlap region $\epsilon \ll |y - y_c| \ll \epsilon^{3/5}$ and the WKBJ and critical layer solutions apply for $|y - y_c|$ greater and smaller than this range respectively. The compressible case is qualitatively similar to the incompressible case.

If $|y - y_c|$ is outside of this validity region, the above WKBJ solutions are not valid and hence the selection of inviscid solutions are not valid as outer solutions to the viscous problem. Additionally, the critical layer solutions when $|y - y_c|$ is small will also not match. Hence, the inviscid equations will not globally match with the viscous solutions even at very high values of R. This is termed by Lees and Lin (1946) as an *inner viscous region.*

When $\Im(c)$ is small, if y_r is the point on the real axis where $\bar{u} = \Re(c)$, then

$$y_c \approx y_r + \frac{\Im(c)i}{D\bar{u}(y_r)}.$$

For $D\bar{u}(y_r) > 0$, y_c is above the real axis for amplified disturbances, and below the real axis for damped disturbances. With small $|\Im(c)|$, $\arg(D\bar{u}_c)$ is very close to 0 and the choice of local and global solutions and hence regions of validity are still applicable. Hence for damped disturbances, part of the real axis will be in the inner viscous region. Because of this, the solution of the inviscid equations must follow a contour below the critical point in a manner that fully avoids the inner viscous region. For the case where $D\bar{u}(y_r) < 0$, y_c is below the real axis for amplified disturbances, and above the real axis for damped disturbances. By the same argument, part of the real axis will be in the inner viscous region for damped disturbances and the contour must pass above the critical point in the correct manner. Figure 5.1 illustrates valid integration paths for unstable and damped mode with a small $|\Im(c)|$ when $D\bar{u}(y_r) > 0$ and there is only one critical layer.

While this has not been investigated in detail it is interesting to consider damped disturbances with values of $\Re(c)$ near $\bar{u}_{max}$ and greater than unity: It may be possible that the inner viscous regions from the two critical points overlap in such a way that there is no possible contour in the complex plane between the wall and freestream over which the inviscid model is valid. This would require further inves-

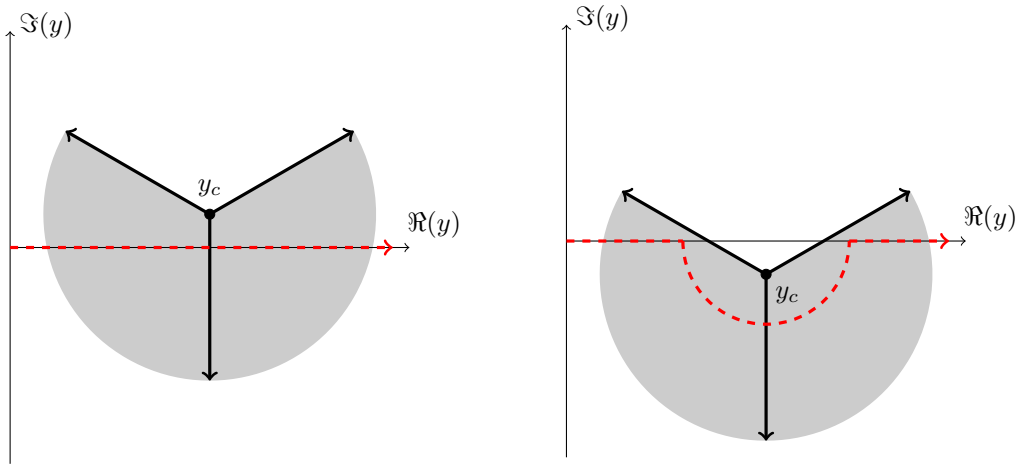

(a) Unstable mode (b) Damped mode

Figure 5.1: Validity region of WKBJ global solutions (shaded region) and suitable inviscid integration path (red dashed line) for the case of $D\bar{u}(y_r) > 0$ and there is one critical layer.

tigation of the inner viscous region taking into account higher-order approximations for the Stokes lines.

5.1.2 Case 2: $c = \bar{u}_{max}$

Here, $(\bar{u} - c) \sim O(\epsilon^2)$, $D\bar{u} \sim O(\epsilon)$, and $\chi \sim O\left(\epsilon^{1/n}\right)$ and the correct choice is now $n = \frac{1}{4}$. Seeking a solution similar to that for Case 1, from equation (5.1) the expansions

$$\begin{aligned}
\hat{u} =& u_0\epsilon + O(\epsilon^2)\\
\hat{v} =& v_0\epsilon^2 + O(\epsilon^3)\\
\hat{p} =& p_0\epsilon^3 + O(\epsilon^4)\\
\hat{T} =& T_0 + O(\epsilon)
\end{aligned}$$

are taken and the equations for the (non-trivial) leading-order viscous corrections are

$$\mathfrak{D}^2 u_0 = \frac{i}{2}\frac{D^2\bar{u}_c}{\bar{T}_c}z^2 u_0 + \frac{D^2\bar{u}_c}{\alpha T_c^2}z v_0 + \frac{i}{\bar{T}_c}p_0, \tag{5.22a}$$

$$\mathfrak{D} v_0 = -i\alpha u_0, \tag{5.22b}$$

$$\mathfrak{D} p_0 = 0, \tag{5.22c}$$

$$\mathfrak{D}^2 T_0 = \frac{Pr}{\alpha}\frac{D\bar{T}_c}{\bar{T}_c^2}v_0 + \frac{iPr}{2}\frac{D^2\bar{u}_c}{\bar{T}_c^2}z^2 T_0. \tag{5.22d}$$

Differentiating equation (5.22b) twice by z, and substituting in equation (5.22a) gives

$$\frac{\mathrm{d}^3 v_0}{\mathrm{d}\zeta^3} - \frac{\zeta^2}{2}\frac{\mathrm{d}v_0}{\mathrm{d}\zeta} + \zeta v_0 = \frac{\alpha}{T_c}\left(\frac{iD^2\bar{u}_c}{\bar{T}_c^2}\right)^{-\frac{3}{4}} p_0, \tag{5.23}$$

or

$$\frac{\mathrm{d}^3 v_0}{\mathrm{d}\zeta^3} + \frac{v_0^2}{2}\frac{\mathrm{d}}{\mathrm{d}\zeta}\left(\frac{\zeta^2}{v_0}\right) = \frac{\alpha}{T_c}\left(\frac{iD^2\bar{u}_c}{\bar{T}_c^2}\right)^{-\frac{3}{4}} p_0 = P_0, \tag{5.24}$$

where the right-hand side is a constant term, and

$$\zeta = \left(\frac{iD^2\bar{u}_c}{\bar{T}_c^2}\right)^{\frac{1}{4}} z$$

is defined. One solution is

$$v_0 = C_0\zeta^2, \tag{5.25}$$

where C_0 is a constant. This can be matched with the $\hat{v}_A$ inviscid solution of section 4.1.2. The other solutions are found by searching for solutions of the form

$$v_0 = \zeta^2 \int_0^\zeta x^{-3} V(x)\,\mathrm{d}x, \tag{5.26}$$

where V is to be determined. By rescaling $\eta = 2^{1/4}\zeta$, equation (5.24) reduces to an inhomogeneous version of the parabolic cylinder equation,

$$\frac{\mathrm{d}^2 V}{\mathrm{d}\eta^2} - \frac{\eta^2}{4}V = 2^{-3/4}P_0\eta. \tag{5.27}$$

Two additional linearly-independent solutions for V can be chosen as Whittaker functions $D_\nu(k_1\eta)$ and $D_\nu(k_2\eta)$ with $\nu = -\frac{1}{2}$, where k_1 and k_2 are complex numbers of unit magnitude with arguments that differ by either $\frac{\pi}{4}$ or $\frac{\pi}{2}$.

Neither of these yield the correct behaviour as $z \to \infty$ required to match with the second inviscid solution $\hat{v}_B$, which has dominant behaviour of $(y - y_c)^{-1}$. However, the particular solution generated by a variation of parameters approach does demonstrate the correct character for matching.

Global Analysis

The WKBJ solutions are of the same form as (5.20) and (5.21), however, as $\bar{u} - c \approx D^2\bar{u}_c(y - y_c)^2$ now,

$$I(y) \sim \left(iD^2\bar{u}_c\right)^{\frac{1}{2}}(y - y_c)^2$$

and the solutions may now only apply over an open sector in $(y - y_c)$ space of angle π. Thus it would be impossible for these solutions to be valid on the real axis on both sides of the critical point.

The important consequence is that there can be no true inviscid neutral modes with $c = \bar{u}_{max}$ in overshoot boundary layers (for finite wavenumbers). As this is the wavespeed at which an unmerged higher mode is expected to first become unstable (replacing the traditional $c = 1$ neutral mode), this observation may provide an explanation as to why unmerged higher modes are not observed in the inviscid results presented in Chapter 3.

5.2 Numerical Methods

The higher order of the viscous stability problem over the inviscid stability problem increases the computational time required for solution. However, this is offset by the absence of many of the issues outlined in section 3.1. The methodology implemented to numerically solve the viscous stability problem follows closely that of Malik (1990), who considered different methods for solving the eigenvalue problem including the 4th-order compact difference scheme (4CD) and the single-domain spectral collocation method (SDSP) which are used here. These methods afford both global and local eigenvalue searches.

The 4CD method is advantageous as it can be implemented over any arbitrary grid so that points may be clustered as necessary to increase the resolution around critical layers, however it suffers from a lower rate of convergence than the SDSP method. Conversely, the SDSP method implements Chebyshev nodes which must be clustered at the edges of the domain. This is advantageous for cases with a low M, where the generalised points of inflection, and hence the critical layers, are located near the surface and thus where points are clustered. However, for the eigenvalues of interest here, this is not the case and the SDSP method requires a substantial number of points. Nevertheless, often the SDSP method is still faster for moderate values of R and for determining eigenvalues that are not near-neutral. For larger values of R the performance of the SDSP method is no longer satisfactory,

Table 5.1: Converged amplified-mode eigenvalues c for various step sizes and methods for boundary-layer case 3 with $R = 5000$, $\alpha = 0.2$

N	Real part (4CD)	Imag. part (4CD)	Real part (SDSP)	Imag. part (SDSP)
1000	0.943676	0.002151	0.943675	0.002150
800	0.943676	0.002152	0.943675	0.002150
600	0.943678	0.002155	0.943675	0.002150
400	0.943683	0.002169	0.943675	0.002150
200	0.943745	0.002214	0.943675	0.002150
100	0.944589	0.002755	0.943675	0.002150
80	0.943350	0.002445	0.943675	0.002149
60	0.937444	0.003510	0.943671	0.002150
40	Diverged		0.943612	0.002059

especially for near-neutral modes where the critical layer is thin; a high resolution is required for consistent solutions.

While computationally expensive, a global eigenvalue search is valuable for finding all eigenvalues. This approach has the disadvantage is that a large number of spurious eigenvalues are also generated. Many of these have large magnitudes and disregarding these is easily accomplished without additional analysis. However, there are often spurious eigenvalues generated close to $c = 1$ and these can be eliminated by parsing these eigenvalues with a local search.

5.2.1 Eigenvalue Accuracy

In tables 5.1 and 5.2 some eigenvalues for each local method with differing numbers of grid points (N) are presented. The starting value for each computation is the $N = 1000$ converged eigenvalue. The first table is a moderate-R amplified-mode case with no significant critical layer. The SDSP method is clearly superior here, achieving convergence to 10^{-6} with only 60 nodes. The second table presents data for a large R near-neutral disturbance when there is a critical layer. The 4CD method is considerably better converged at lower values of N.

Table 5.2: Converged near-neutral eigenvalues c for various step sizes and methods for boundary-layer case 3 with $R = 10000$, $\alpha = 0.4$

N	Real part (4CD)	Imag. part (4CD)	Real part (SDSP)	Imag. part (SDSP)
1000	1.042136	0.000807	1.042135	0.0008086
800	1.042136	0.000806	1.042135	0.0008086
600	1.042137	0.000804	1.042135	0.0008086
400	1.042136	0.000797	1.042135	0.0008086
200	1.042135	0.000807	1.042135	0.0008086
100	1.042121	0.000834	1.042723	0.0008629
80	1.042136	0.000739	1.044425	-0.001340
60	1.042239	0.000667	1.174574	-0.015029
40	Diverged		1.174584	-0.015023

5.2.2 Eigenvalue Convergence

The suitability of the numerical method must also consider the convergence region of the eigenvalues. As the (complex) eigenvalues are locally solved through use of a Newton-Raphson method, the borders of the convergence regions are fractal in nature. A small convergence region can lead to the failure of the method, or a need to overly-refine continuation methods used in the functions that track eigenvalue families or neutral curves.

In figure 5.2 convergence diagrams are presented for a case where there are two eigenvalues near each other. Local searches were initiated from a grid of starting eigenvalue guesses and the colours refer to the corresponding eigenvalue (at the stars). Other points tested either diverged or converged to a different eigenvalue. In this case, the convergence of the 4CD method is more irregular, but in both cases the fractal nature of the convergence regions is notable in the small exclaves of convergence for each eigenvalue. This is particularly notable in the top-left and bottom-right of figure 5.2b.

In figure 5.3 convergence diagrams are presented for an eigenvalue near the upper-branch inflectional neutral mode for boundary-layer case 3. There are strong critical layers forming here and the local eigenvalue search is very sensitive to the

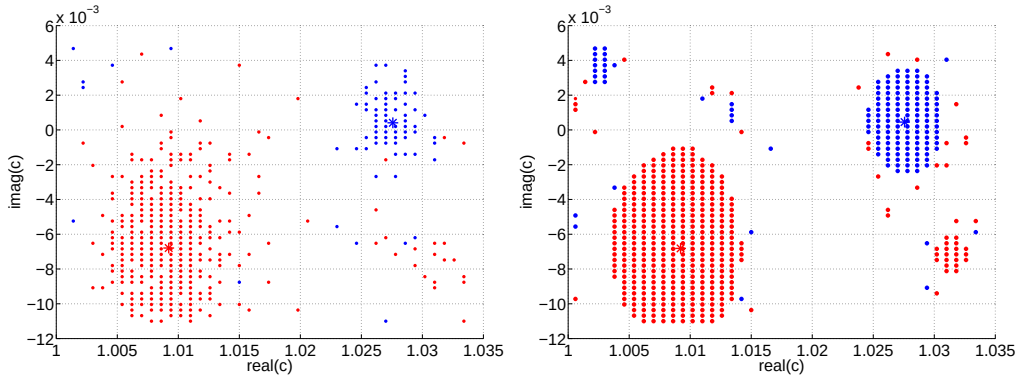

(a) 4CD, $N = 150$ (b) SDSP, $N = 150$

Figure 5.2: Convergence diagrams for boundary-layer case 3 at $R = 1700$, $\alpha = 0.5$.

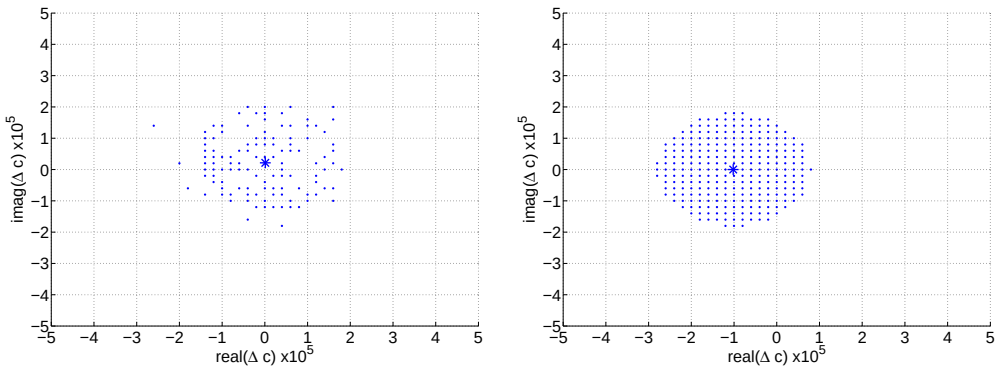

(a) 4CD, $N = 150$ (b) SDSP, $N = 200$

Figure 5.3: Convergence diagrams for boundary-layer case 3 at $R = 10000$, $\alpha = 1.3$. Δc is the difference between the starting value and the true eigenvalue, $c = 1.049414 + 0.001576206i$.

initial guess. At $N = 150$ the convergence region for the 4CD method is small and irregular. For the same number of nodes the SDSP method will not converge to this eigenvalue for any starting point tested. For $N = 200$ however, the SDSP method has a similarly sized convergence region and is more regular, however the real part of the eigenvalue found is in slight error.

The convergence regions can be unpredictable and demonstrate that considerable care must be taken when selecting a suitable method and number of nodes for a particular set of stability calculations.

5.2.3 Computational Expenditure

In table 5.3 computation times are presented for each of the methods. The duration for the local methods are quoted per ten matrix inversions and do not necessarily represent the time taken for an eigenvalue to converge. The performance of the SDSP method is superior in general; although the matrices are dense, they are of order $5N$ as opposed to the 4CD method, which has tri-diagonal matrices of order $8N$. The global method consists of the generalised eigenvalue solution routine and the purification of eigenvalues through filtering and parsing.

Table 5.3: Computation time (seconds) for various step sizes and methods.

N	Local (4CD)*	Local (SDSP)*	Global (SDSP)
60	0.226	0.207	1.205
100	0.559	0.560	4.037
150	1.314	1.136	14.71
200	2.428	1.987	36.84
250	4.213	3.178	81.74
300	6.707	5.029	126.6
500	25.67	19.55	661.0
1000	175.1	120.2	-

*Time per 10 inversions.

5.2.4 Functions

To facilitate some of the functions discussed below, the Reynolds number R is scaled (usually by a factor of 20000) to define suitable geometric angles (ϕ) and lengths (L) in the α-R plane. These are defined as

$$\phi = \arctan \frac{\Delta R}{R_{scale} \Delta \alpha} \tag{5.28}$$

$$L = \sqrt{\left(\frac{\Delta R}{R_{scale}}\right)^2 + (\Delta \alpha)^2} \tag{5.29}$$

Eigenvalue Tracking

This function is the same as the corresponding inviscid function discussed in section 3.2, but with a constant value of R.

Neutral Mode Search

This function searches for neutral modes in the α-R plane given a starting guesses for (α, R) and c and a reference point (α_r, R_r). This reference point is actually defined by supplying the move length L and angle ϕ in the scaled α-R plane to get to the starting point from the reference point. This is most convenient for determining neutral curves (see below). A neutral mode is searched for along an arc with the reference point as the centre using a Newton-Raphson method to find a zero of $\Im(c)$.

Various measures are implemented to ensure that the method is stable and does not jump to another eigenvalue family, breaking the continuation. The angular change for each iteration is bounded to avoid large movements in the α-R plane, and the bound on the angular change is randomised between 0.015π and 0.02π to avoid limit cycles. A history of each iteration is stored so that the best estimate for c can be made after each iteration to aid convergence. Convergence is obtained if either $|\Im(c)| < 10^{-10}$ or if a sign change of $\Im(c)$ is detected over $\Delta\phi < 10^{-8}\pi$.

The neutral mode search fails if either convergence isn't achieved within 15 iterations, the local eigenvalue search fails to converge, the wavespeed $\Re(c)$ differs from the original guess by 0.005 or more, or a local extrema in $\Im(c)$ is detected.

Neutral Curve Determination

The neutral curve function requires a high-R neutral eigenvalue as a starting point, along with an initial movement length L. A second neutral point is found by running the neutral mode search with a move of L in the direction $\phi = \pi$ (i.e. horizontally left in the α-R plane) with the same c. Successive moves are made using polynomial extrapolation techniques to predict the next location (with correct move length L) and associated eigenvalue guess. If either the neutral mode search

function fails, the difference in ϕ between successive moves is greater than $\pi/6$, or either α or R are negative the result is not accepted and L is decreased. If L has been decreased and five consecutive, successful moves take place, L is increased again. This ensures sufficient resolution of the neutral curve near areas of high curvature. Computation is stopped when R exceeds the starting value (success) or if L has been decreased below 10^{-10} (failure).

5.3 Curves of Neutral Stability

In this section curves of neutral stability are presented for the boundary layers of interest. These neutral curves demarcate regions of instability in the parameter space. Given the high dimensionality of the parameter space, the results are presented by considering individual boundary-layer cases where the parameters M, β, g_w are chosen and the neutral curves are presented in projections of α-R and α-c space. The crosses indicate a common point in both projections. The parameter values of the boundary-layer cases considered are the same as those quoted in table 3.1.

First, neutral curves for boundary-layer case 1, a compressible, flat-plate boundary layer with no velocity overshoot is presented. In the first case (figure 5.4) there are two distinct neutral curves that correspond to the first and second mode disturbances respectively. The lower branch of the first mode corresponds to the inviscid upstream sonic mode and its upper branch corresponds to the (first) inflectional mode. The lower branch of the second mode corresponds to non-inflectional ($c = 1$) inviscid neutral mode and its upper branch corresponds to the inflectional mode at a higher wavenumber. Higher modes also present neutral curves however these are negligible at this Mach number; they demarcate unstable disturbances with small growth rates, and feature only at very large values of R. These higher mode neutral curves, when not merged, have similar lower branch and upper branch behaviour to the second mode but occur at higher wavenumbers.

In figure 5.5, the Mach number is increased and the first and second modes merge at finite values of R, as they do in the inviscid results. The consequence

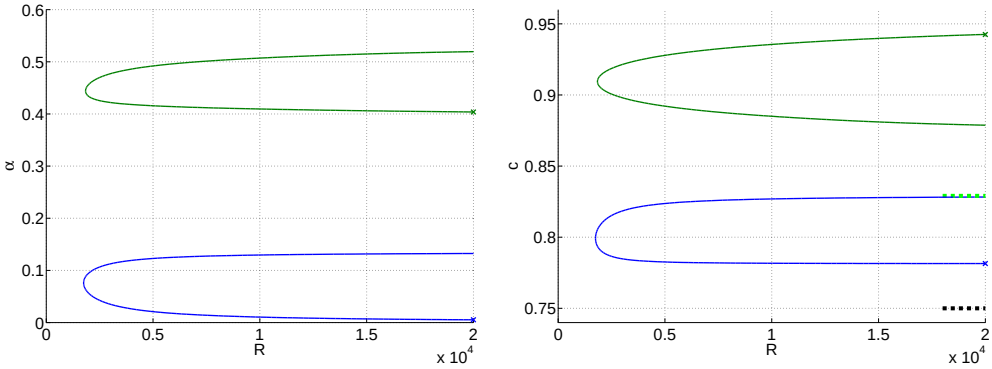

(a) α vs R

(b) c vs R, with inflectional velocity (– – –) and sonic velocity (– – –)

Figure 5.4: Neutral curves (upstream family, blue; first downstream family, green) for boundary-layer case 1 ($M = 4$, $g_w = g_{ad}$, $\beta = 0$).

for the viscous analysis is that the neutral curves combine and form a single large unstable region. A close analysis of the merging process reveals that the merge happens as the neutral curves intersect in α-R-c space. At higher Mach numbers the third and higher modes are unstable at lower values of R, attain higher growth rates and also merge with this large unstable region.

In section 3.4 it was found that overshoot boundary layers possess another unstable inviscid mode for low values of α that exists along with the traditional first mode. In figure 5.6 neutral curves for a boundary layer with a moderate velocity overshoot are plotted. When this new mode (red curve) is isolated, or does not interact with other modes, the lower branch corresponds to the new low-wavenumber inviscid mode located at the velocity maximum, and its upper branch is another new inviscid non-inflectional neutral mode at $c = c_m$. The blue neutral curve consists of the traditional first, second, and third modes. At approximately $R = 1800$, $\alpha = 0.45$, $c = 1.03$ there is a near intersection. In fact if β is slightly decreased the merge has taken place. In figure 5.7 neutral curves are presented showing the behaviour just as the merge has happened.

The behaviour of the neutral curves is made more complicated by the presence of velocity overshoot. This is because interaction with the second and higher modes may now occur with either the traditional first mode or the new mode. Further

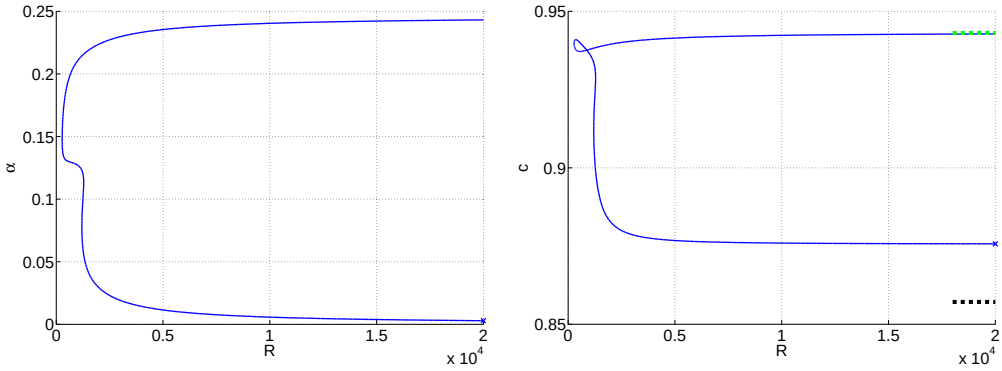

(a) α vs R

(b) c vs R, with inflectional velocity (– – –) and upstream sonic velocity (– – –)

Figure 5.5: Neutral curve (upstream family) for boundary-layer case 2 ($M = 7$, $g_w = g_{ad}$, $\beta = 0$).

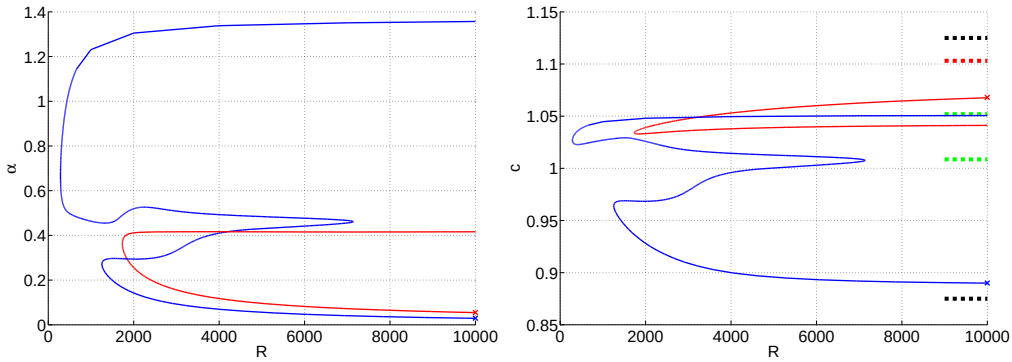

(a) α vs R

(b) c vs R, with inflectional velocities (– – –), sonic velocities (– – –) and maximum velocity (– – –)

Figure 5.6: Neutral curves (upstream family, blue; new family, red) for boundary-layer case 3 ($M = 8$, $g_w = 1.2$, $\beta = 0.4$).

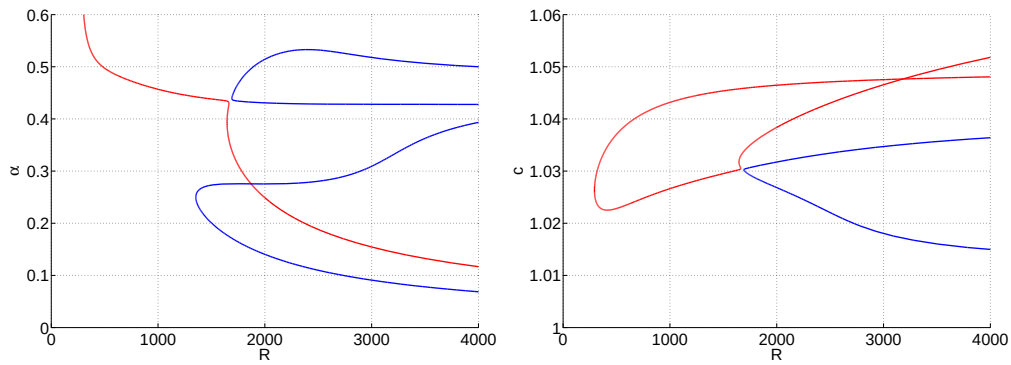

(a) α vs R (b) c vs R

Figure 5.7: Neutral curves (upstream family, blue; new family, red) for boundary-layer case 3a ($M = 8$, $g_w = 1.2$, $\beta = 0.38$).

complications arise when the inflectional velocities, c_m, and velocity maximum no longer reside in the subsonic zone.

The neutral curves presented in 5.8 demonstrate interesting behaviour. The blue curve consists of the lower branch of the first (upstream) mode and the upper branch of the first mode. The red curve consists of the lower branch of the new mode and the upper branch of the third mode, which is not shown in 5.8a and approaches $\alpha \approx 1.31$ and an inflectional velocity. The green curve is of interest here, its lower branch is in fact the upper branch of the new mode and its upper branch is the lower branch of the third mode. In fact, careful calculation at higher values of R indicates that the upper branches of the blue and green curves meet and the green curve is in fact part of the blue curve. This observation is supported by the inviscid results for this boundary layer, where the first mode and higher modes have merged (figures 3.8-3.11). The value of R where the meeting occurs is reduced when β (or g_w) is increased; figure 5.9 illustrates the movement of the loop when β is slightly increased. To the left of this loop in the α-R plane of figure 5.9a, the large unstable second mode is merged with the new mode, otherwise it is merged with the upstream (first) mode.

Next, the case where the overshoot is increased to such a level that $\bar{u}_{max}$ is above $1+1/M$ is examined. In figure 5.10 the neutral curves for such a boundary layer are presented. The lower branch associated with the new inviscid mode (red curve) no

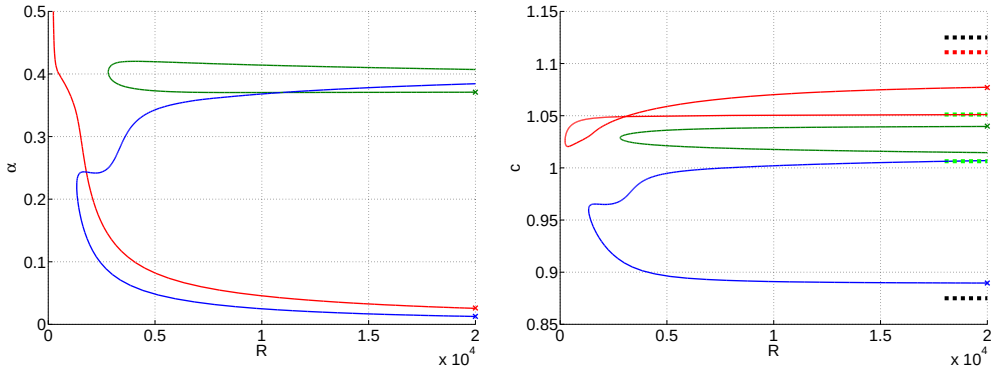

(a) α vs R

(b) c vs R, with inflectional velocities (– – –), sonic velocities (– – –) and maximum velocity (– – –)

Figure 5.8: Neutral curves (upstream family, blue and green; new family, red) for boundary-layer case 4 ($M = 8$, $g_w = 1.3$, $\beta = 0.3$).

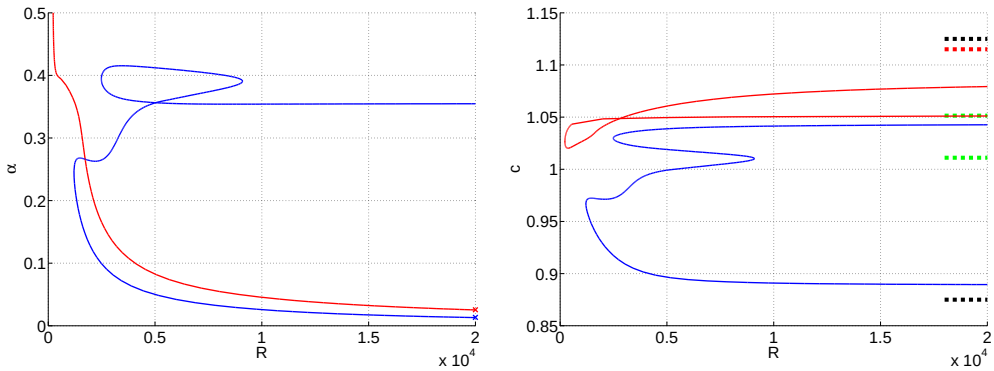

(a) α vs R

(b) c vs R, with inflectional velocities (– – –), sonic velocities (– – –) and maximum velocity (– – –)

Figure 5.9: Neutral curves (upstream family, blue; new family, red) for boundary-layer case 4a ($M = 8$, $g_w = 1.3$, $\beta = 0.32$.

longer approaches $c = \bar{u}_{max}$ in the high R limit; it instead approaches a wavespeed of less than $1 + 1/M$, which may be one of the inflectional velocities. The neutral mode wavespeeds in the high R limit are best analysed using figure 5.10c, where the wavespeeds have been plotted against $1/R$. The green curve encloses a viscous region of stability where the new mode is damped. The upper branch of this curve approaches $c = 1+1/M$, which corresponds to the new mode of the inviscid results. The lower branches of the red and green curves become irrelevant in the high R limit. Unlike in figure 5.8 the wavespeeds do not appear to match so it is unlikely the green curve is a loop; it is suggested that these exist as discrete inviscid neutral modes at $\alpha = 0$. The lower branch of the blue curve is the inviscid upstream mode and the upper branch appears to correspond to the new non-inflectional neutral mode, refer to the inviscid results of figure 3.12.

Finally, in figure 5.11 a case where the overshoot is further increased such that $\bar{u}_{max}$ and all of the inflectional velocities are no longer subsonic is presented. The blue curve consists of the upper branch of the new mode, approaching $c = 1+1/M$, and the lower branch of the (upstream) first mode, approaching $c = 1 - 1/M$. For low values of R (completely to the left of the blue curve) the new mode and its merged second and higher modes form the entire unstable region. At higher values of R, the new mode becomes stable at the wavenumber corresponding to the upper part of the blue curve. In the high R limit, the new mode is completely stabilised and the only unstable modes remaining are the classical modes; it is not featured in the inviscid results of figure 3.13. The upper branch of the red curve is supersonic and no longer appears to approach the inflectional velocity, as per the aforementioned inviscid results.

5.4 Viscous Neutral-Mode Eigenfunctions

In this section the viscous neutral modes are examined at high Reynolds number, which correspond to the inviscid neutral modes, and examine their eigenfunctions. The eigenfunctions can give physical insight into the nature of the disturbance propagation (Mack, 1984), by indicating regions in the boundary-layer flow where

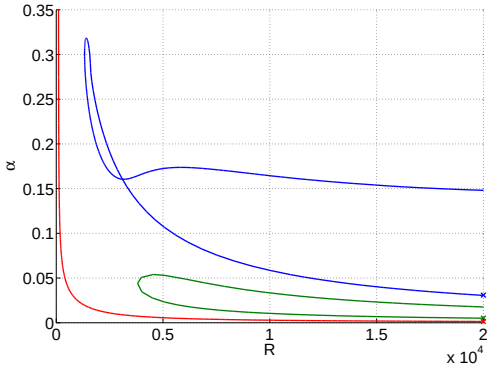

(a) α vs R

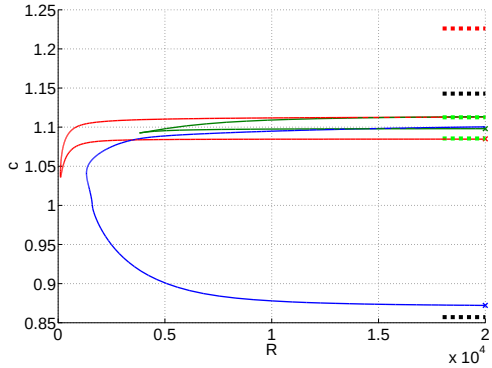

(b) c vs R, with inflectional velocities (– – –), sonic velocities (– – –) and maximum velocity (– – –)

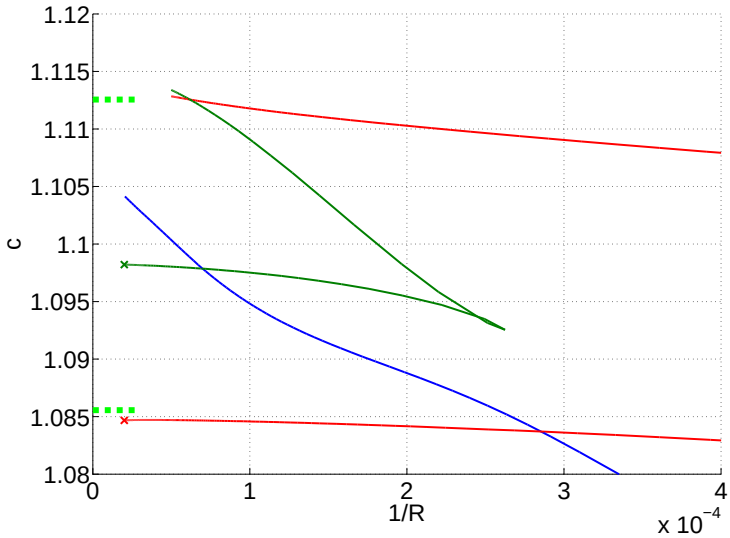

(c) c vs $1/R$, with inflectional velocities (– – –)

Figure 5.10: Neutral curves (upstream family, blue; new family, red) for boundary-layer case 5 ($M = 7$, $g_w = 1.5$, $\beta = 1$)

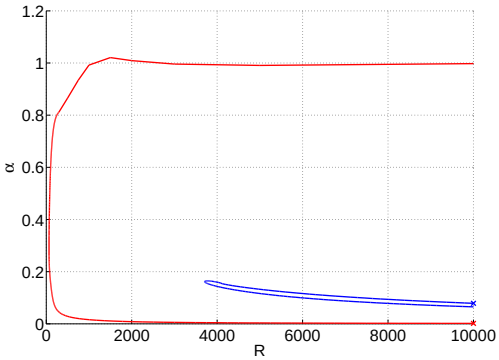

(a) α vs R

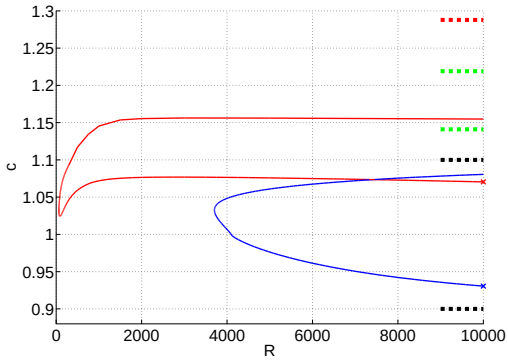

(b) c vs R, with inflectional velocities (– – –), sonic velocities (– – –) and maximum velocity (– – –)

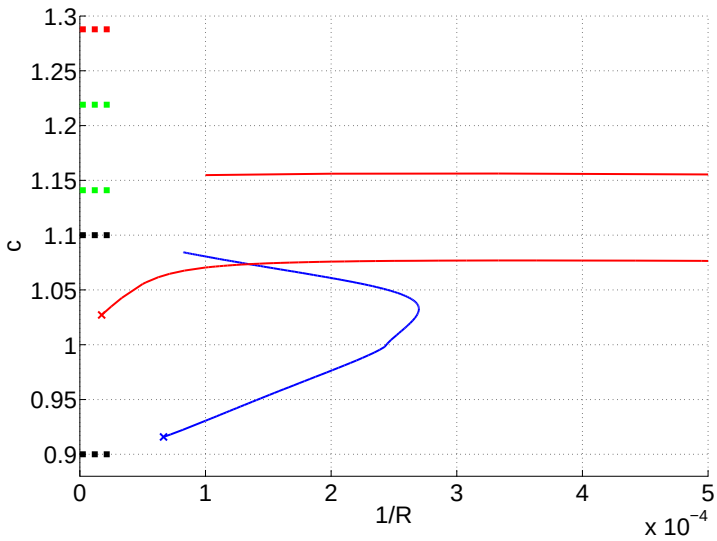

(c) c vs $1/R$, with inflectional velocities (– – –), sonic velocities (– – –) and maximum velocity (– – –)

Figure 5.11: Neutral curves (upstream family, blue; new family, red) for boundary-layer case 6 ($M = 10$, $g_w = 1.5$, $\beta = 0.7$)

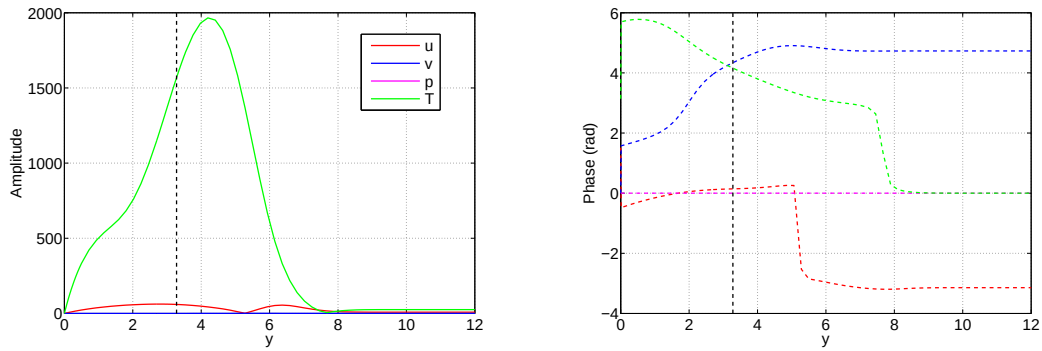

(a) Eigenfunction amplitude

(b) Eigenfunction phase

Figure 5.12: Lower-branch ($R = 50000$) upstream-mode eigenfunctions for boundary-layer case 3 ($M = 8$, $g_w = 1.2$, $\beta = 0.4$).

the disturbance is localised.

Due to the linearity of the system the eigenfunctions may be scaled arbitrarily, however the usual scale in the work presented here is chosen such that the pressure eigenfunction is unity at the wall. The phases have unwrapped; large phase jumps have been corrected by $\pm 2\pi$ to better represent true phase changes.

The vertical lines are locations in the boundary layer where $\bar{u} = c$, indicating possible the locations of critical layers. The dash-dotted lines correspond to an inflectional velocity, whereas dashed lines correspond to a non-inflectional velocity.

5.4.1 Lower-Branch Neutral Modes

The lower-branch neutral modes are classified as those whose wavenumber $\alpha \to 0$ as $R \to \infty$. These are long wavelength disturbances whose eigenfunctions decay in the freestream like $\exp(-\alpha y)$, as can be seen in equation (1.65), for example. There are two such neutral modes in overshoot boundary layers. The first of these lower-branch modes is the upstream sonic mode, present in both non-overshoot and overshoot boundary layers. Its wavespeed $c \to 1 - 1/M$ and its nature is discussed in depth by Lees and Lin (1946). Some typical eigenfunctions for this mode are illustrated in figure 5.12.

The second lower-branch mode, depicted in figure 5.13, is associated with the new inviscid mode and has a wavespeed $c \to \bar{u}_{max}$ if $\bar{u}_{max} < 1 + 1/M$.

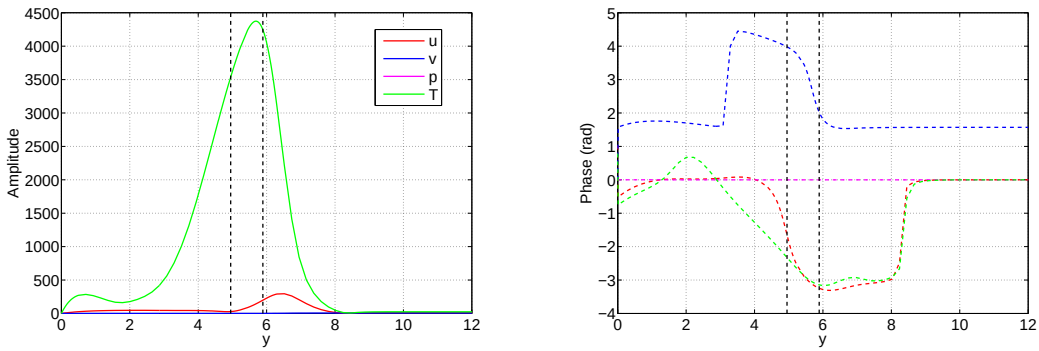

(a) Eigenfunction amplitude

(b) Eigenfunction phase

Figure 5.13: Lower-branch ($R = 50000$) new-mode eigenfunctions for boundary-layer case 3 ($M = 8$, $g_w = 1.2$, $\beta = 0.4$).

For both of these sets of lower branch eigenfunctions, the temperature perturbation is the largest but no perturbation shows any near-singular behaviour. In both results, the pressure perturbation is effectively constant (equal to 1) for the domain plotted. Although the value of R may be large, α is small, and αR is not large enough to form a significant critical layer. All eigenfunctions decay exponentially, albeit slowly for large y. The cases where the new mode does not approach $c \to \bar{u}_{max}$, cases 5 and 6, do not seem to alter the eigenfunctions significantly.

5.4.2 Upper-Branch Neutral Modes

The traditional upper-branch neutral mode is examined first in figure 5.14. There is one critical layer, which is inflectional. The real parts of the eigenfunctions are presented, each normalised by their maximum absolute value, to demonstrate each component's behaviour. When not normalised, the temperature perturbation is very large (about 1000 times larger than the pressure), followed by the streamwise and normal velocities (both about 15 times larger than the pressure). These components clearly show rapid variation around the critical layer. The pressure perturbation, meanwhile, is stationary at the critical point. It has one zero indicating that this upper-branch mode corresponds to the second mode Mack (1969).

This can be compared to the corresponding case in an overshoot boundary layer (case 3, figure 5.15), where the inflectional velocity is greater than unity. In this

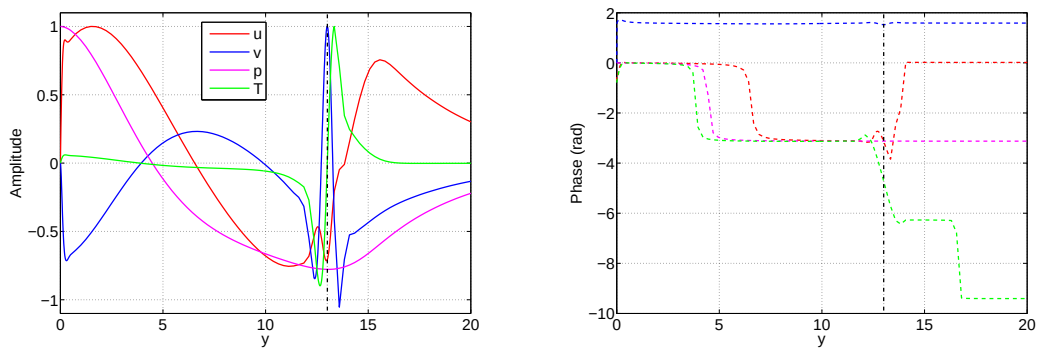

(a) Normalised real parts of the eigenfunctions

(b) Eigenfunction phase

Figure 5.14: Upper-branch ($R = 50000$) inflectional-mode eigenfunctions for boundary-layer case 2 ($M = 7$, $g_w = g_{ad}$, $\beta = 0$).

case, there is a critical layer either side of the velocity maximum, but only one is inflectional. The normalised real parts of the eigenfunctions are presented; again the temperature perturbation is largest, followed by the velocity perturbations and then the pressure. The pressure perturbation has two real zeros, indicating it corresponds to the third mode. It is expected that the solution is analytic at the inflectional critical point in the inviscid limit. However, both the inflectional and non-inflectional critical layers behave similarly with rapid variation in the vicinity of the critical points. When passing the critical point in the inviscid limit, there is a logarithmic singularity in $\hat{u}$ (see equations 1.59 and 4.4) with a coefficient of $D(D\bar{u}/\bar{T})$, and hence at an inflection point this singularity should disappear. However, the neutral wavespeed at $R = 20000$ is 1.05124... as compared to the inflectional velocity of 1.05195..., so $D(D\bar{u}/\bar{T})$ is small but not zero.

The upper branch of the new mode is examined in figure 5.16. In the inviscid limit this approaches the non-inflectional wavespeed c_m and as such it has two non-inflectional critical layers. The pressure perturbation has no zeros and could thus be classified as a first mode disturbance.

For the boundary-layer case 6, all of the inflectional velocities are greater than the $1 + 1/M$ and hence the inflectional neutral mode is supersonic. If the inviscid far-field pressure disturbance as in equation 1.65 is considered, the term under the square root, $1 - M^2(1 - c)^2$ is negative when $c > 1 + 1/M$ (or $c < 1 - 1/M$) and

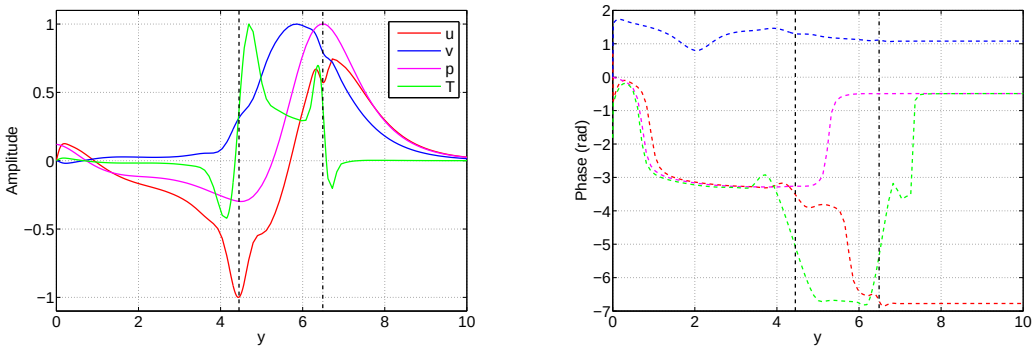

(a) Normalised real parts of the eigenfunctions (b) Eigenfunction phase

Figure 5.15: Upper-branch ($R = 50000$) inflectional-mode eigenfunctions for boundary-layer case 3 ($M = 8$, $g_w = 1.2$, $\beta = 0.4$).

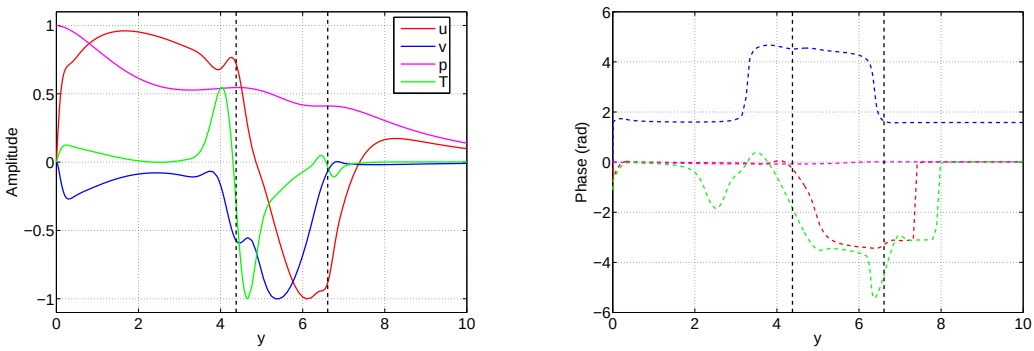

(a) Normalised real parts of the eigenfunctions (b) Eigenfunction phase

Figure 5.16: Upper-branch ($R = 50000$) non-inflectional-mode eigenfunctions for boundary-layer case 3 ($M = 8$, $g_w = 1.2$, $\beta = 0.4$).

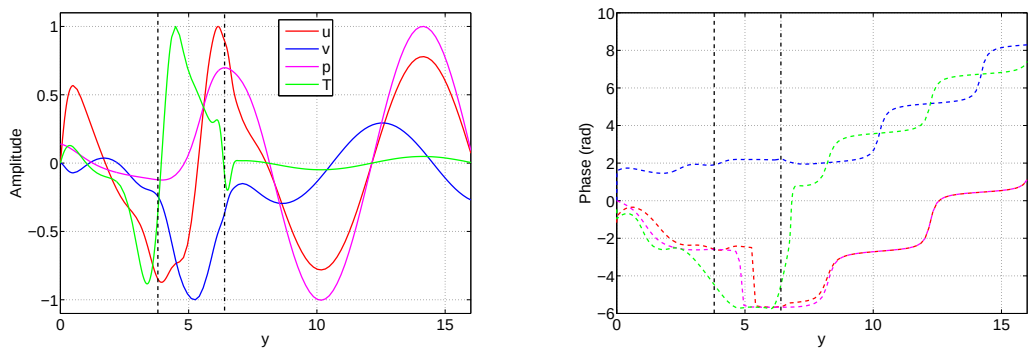

(a) Normalised real parts of the eigenfunctions

(b) Eigenfunction phase

Figure 5.17: Upper-branch ($R = 10000$) supersonic inflectional-mode eigenfunctions for boundary-layer case 6 ($M = 10$, $g_w = 1.5$, $\beta = 0.7$).

is real. In this case, both far-field solutions are bounded sinusoids and therefore valid. However, for non-neutral disturbances, $1 - M^2(1-c)^2$ is complex and only one solution is bounded. In figure 5.17 the oscillatory nature of the far-field solution is evident.

5.5 Summary

The inviscid stability results presented in Chapters 3 and 4 are confirmed through comparison with the viscous stability analysis in the large Reynolds number limit, in particular the new small-wavenumber neutral mode and the new non-inflectional mode. The existence of the new mode alongside the first mode complicates the viscous stability behaviour; the additional possibilities for mode interaction cause loops and collisions in the curves of neutral stability. In cases where the characteristic neutral wavespeeds are supersonic there can be additional neutral curves that are closed in the inviscid limit.

Chapter 6

Concluding Remarks and Future Work

The development of efficient high-speed aircraft requires a comprehensive understanding of the structure of the fluid flow over the body surface, and the laminar-turbulent transition behaviour. In many current hypersonic vehicle prototypes, the boundary-layer flow and the disturbances that cause transition are predominantly two-dimensional. The literature of two-dimensional, compressible boundary-layer stability is mature but analysis of boundary layers with a velocity overshoot has not yet been addressed. Velocity overshoot occurs in accelerated compressible boundary layers over a heated surface and can present additional generalised points of inflection that are responsible for inviscid instabilities.

The existence of velocity overshoot in these boundary layers was demonstrated asymptotically and a range of boundary-layer properties were presented over the large parameter space studied. Among these results, cases are presented where the generalised point of inflection associated with the neutralisation of the first-mode disturbance can be removed; later shown to correspond to complete stabilisation of the first mode. In the high Mach number limit, an analytic solution to the self-similar boundary-layer equations was presented along with an expression for the maximal velocity.

In investigating the linear stability of these overshoot boundary layers, a new family of inviscid, subsonic eigenvalues was discovered that contains set of new un-

stable solutions. An analytic solution for the new low-wavenumber neutral mode associated with this family was presented to further strengthen the numerical solutions. The nonzero-wavenumber neutral mode which has been identified, where the new mode is stabilised, is not inflectional and its eigenfunction is singular in the inviscid limit. A viscous stability analysis was also completed, confirming that the inviscid results presented correspond to the high Reynolds number limit of the viscous results. When the Mach number is sufficiently large the new mode eventually becomes stabilised, although for an oblique travelling disturbance it may still be unstable.

The classical Mack modes are also affected by the velocity overshoot, the range of wavespeeds unstable inviscid Mack modes may attain increases and this corresponds to an increase in the growth rate. An increase in Mach number can result in all inflectional velocities being supersonic, however unlike the cooled boundary-layer case, the Mack modes are still neutralised in the inviscid limit but instead at a supersonic non-inflectional wavespeed.

This thesis comprises an investigation into the stability of heated, accelerated compressible boundary layers, focussing on the two-dimensional temporal stability. The new mode identified can have growth rates comparable to the classical modes and a spatial stability analysis could serve to estimate the overall effect on the transition process. Also of particular interest would be to investigate the non-parallel forms of the new-mode upper and lower branch solutions, which could serve to provide physical insight into this new instability.

Bibliography

M. Abramowitz and I. A. Stegun. *Handbook of mathematical functions*. Dover Publications, Inc., New York, 1966.

A. P. Bassom and J. S. B. Gajjar. Non-stationary cross-flow vortices in three-dimensional boundary-layer flows. *Proceedings of the Royal Society of London*, 417(1852):179–212, 1988.

A. P. Bassom and P. Hall. On the interaction of stationary crossflow vortices and Tollmien-Schlichting waves in the boundary layer on a rotating disc. *Proceedings of the Royal Society of London*, 430:25–55, 1990.

H. Blasius. The boundary layers in fluids with little friction. *NACA Technical Memorandum 1256 (English translation of original German language publication in 1908)*, pages 1–37, 1950.

R. J. Bodonyi and F. T. Smith. The upper branch stability of the Blasius boundary layer, including non-parallel flow effects. *Proceedings of the Royal Society A: Mathematical, Physical and Engineering Sciences*, 375(1760):65–92, February 1981.

D. Bountin, T. Chimitov, A. Maslov, A. Novikov, I. Egorov, A. V. Fedorov, and S. Utyuzhnikov. Stabilization of a hypersonic boundary layer using a wavy surface. *AIAA Journal*, 51(5):1203–1210, May 2013.

W. B. Brown and P. L. Donoughe. Tables of exact laminar-boundary-layer solutions when the wall is porous and fluid properties are variable. *NACA Technical Note 2479*, 1951.

D. R. Chapman and M. W. Rubesin. Temperature and velocity profiles in the compressible laminar boundary layer with arbitrary distribution of surface temperature. *Journal of the Aeronautical Sciences*, 16(9):547–565, 1949.

C. B. Cohen and E. Reshotko. Similar solutions for the compressible laminar boundary layer with heat transfer and pressure gradient. *NACA Technical Report 1293*, 1955.

S. Cowley and P. Hall. On the instability of hypersonic flow past a wedge. *Journal of Fluid Mechanics*, 214:17–42, April 1990.

S. J. Cowley and F. T. Smith. On the stability of Poiseuille-Couette flow: a bifurcation from infinity. *Journal of Fluid Mechanics*, 156:83–100, 1985.

J. P. Denier and E. W. Mureithi. Weakly nonlinear wave motions in a thermally stratified boundary layer. *Journal of Fluid Mechanics*, 315:293–316, 1996.

C. F. Dewey and J. F. Gross. Exact similar solutions of the laminar boundary-layer equations. *Advanced Research Projects Agency Memorandum*, RM-5089-AR, 1967.

A. A. Dorodnitsyn. Boundary layer in compressible gas. *Prikl. Mat. Mekh*, 6(6): 449–486, 1942.

P. G. Drazin. *Hydrodynamic stability.* Cambridge University Press, second edi edition, 2004.

V. M. Falkner and S. W. Skan. Solutions of the boundary-layer equations. *The London, Edinburgh, and Dublin Philosophical Magazine and Journal of Science*, 12(80):865–896, April 1931.

A. V. Fedorov. Transition and stability of high-speed boundary layers. *Ann. Rev. Fluid Mech.*, 43(1):79–95, January 2011.

A. V. Fedorov. Prediction and control of laminar-turbulent transition in high-speed boundary-layer flows. *Procedia IUTAM*, 14:3–14, 2015.

A. V. Fedorov, H. G. Hornung, N. D. Malmuth, and A. Rasheed. Stabilization of hypersonic boundary layers by porous coatings. *AIAA Journal*, 39(4):605–610, April 2001.

J. S. B. Gajjar. Nonlinear evolution of the first mode supersonic oblique waves in compressible boundary layers. Part I - heated/cooled Walls. *NASA Technical Memorandum 106087*, 1993.

M. Gaster. A note on the relation between temporally-increasing and spatially-increasing disturbances in hydrodynamic stability. *Journal of Fluid Mechanics*, 14(02):222, March 1962.

M. Gaster. On the effects of boundary-layer growth on flow stability. *Journal of Fluid Mechanics*, 66:465–480, 1974.

H. Görtler. On the three-dimensional instability of laminar boundary layers on concave walls. *NASA Technical Memorandum 1375 (English translation of original German language publication in 1940)*, 1954.

N. Gregory, J. T. Stuart, and W. S. Walker. On the stability of three-dimensional boundary layers with application to the flow due to a rotating disk. *Philosophical Transactions of the Royal Society of London. Series A, Mathematical and Physical Sciences*, 248(943):155–199, 1955.

P. Hall. An asymptotic investigation of the stationary modes of instability of the boundary layer on a rotating disc. *Proceedings of the Royal Society of London*, 406(1830):93–106, 1986.

P. Hall. Görtler vortices in growing boundary layers: the leading edge receptivity problem, linear growth and the nonlinear breakdown stage. *Mathematika*, 37(2): 151–189, 1990.

P. Hall, M. R. Malik, and D. I. A. Poll. On the stability of an infinite swept attachment line boundary layer. *Proceedings of the Royal Society of London*, 395:229–245, 1984.

D. R. Hartree. On an equation occurring in Falkner and Skan's approximate treatment of the equations of the boundary layer. *Proc. Camb. Phil. Soc*, 12(1931), 1937.

L. Howarth. Concerning the effect of compressibility on laminar boundary layers and their separation. *Proceedings of the Royal Society of London. Series A. Mathematical and Physical Sciences*, 194(1036):16–42, 1948.

C. R. Illingworth. Some solutions of the equations of flow of a viscous compressible fluid. *Mathematical Proceedings of the Cambridge Philosophical Society*, 1950.

D. Küchemann. Störungsbewegungen in einer gasströmung mit grenzschicht. *Zeitschrift für Angewandte Mathematik und Mechanik*, 18:207–222, 1938.

L. Lees. The stability of the laminar boundary layer in a compressible fluid. *NACA Technical Note 1360*, 1947.

L. Lees and C. C. Lin. Investigation of the stability of the laminar boundary layer in a compressible fluid. *NACA Technical Note*, 1115, 1946.

I. Leyva. Transition delay in hypervelocity boundary layers by means of CO2/acoustic instability interactions. *47th AIAA Aerospace Sciences Meeting*, 2009.

T. Y. Li and H. T. Nagamatsu. Similar solutions of compressible boundary layer equations. *J. Aeronaut. Sci*, pages 607–616, 1955.

C. C. Lin. On the stability of two-dimensional parallel flows. *Quarterly of Applied Mathematics*, 3(2):117–142, 1945.

L. M. Mack. Boundary-layer linear stability theory. Technical report, Jet Propulsion Laboratory Document 900-277 Rev. A, Pasadena, CA, 1969.

L. M. Mack. Special course on stability and transition of laminar flow. *AGARD report*, 709, 1984.

L. M. Mack. Review of linear compressible stability theory. *Stability of time dependent and spatially varying flows*, pages 164–187, 1987.

M. R. Malik. Wave interactions in three-dimensional boundary layers. *AIAA paper*, 1986.

M. R. Malik. Numerical methods for hypersonic boundary layer stability. *J. Comp. Phys.*, 86(2):376–413, February 1990.

J. B. McLeod and J. Serrin. The behaviour of similar solutions in a compressible boundary layer. *Journal of Fluid Mechanics*, 34(02):337–342, 1968a.

J. B. McLeod and J. Serrin. The existence of similar solutions for some laminar boundary layer problems. *Archive for Rational Mechanics and Analysis*, 31, 1968b.

J. C. P. Miller. On the choice of standard solutions for a homogeneous linear differential equation of the second order. *The Quarterly Journal of Mechanics and Applied Mathematics*, III(2):225–235, 1950.

F. K. Moore. Laminar boundary layer on cone in supersonic flow at large angle of attack. *NACA Technical Report 1132*, 1953.

M. V. Morkovin. On the many faces of transition. In C. S. Wells, editor, *Viscous drag reduction*, pages 1–31. Springer, New York, 1969.

E. W. Mureithi, J. P. Denier, and J. Stott. The effect of buoyancy on upper-branch Tollmien-Schlichting wares. *IMA J. Appl. Math.*, 58(April 1995):19–50, 1997.

A. H. Nayfeh. Effect of streamwise vortices on Tollmien-Schlichting waves. *Journal of Fluid Mechanics*, 107:441–453, 1981.

L. Prandtl. Motion of fluids with very little viscosity. *NACA Technical Memorandum 452 (English translation of original German language publication in 1904)*, 1928.

A. Rasheed, H. G. Hornung, A. V. Fedorov, and N. D. Malmuth. Experiments on passive hypervelocity boundary-layer control using an ultrasonically absorptive surface. *AIAA Journal*, 40(3):481–489, March 2002.

L. Rayleigh. On the stability, or instability, of certain fluid motions. *Proceedings of the London Mathematical Society*, 1:57, 1879.

H. L. Reed. Wave interactions in sweptwing flows. *Physics of Fluids (1958-1988)*, 1984.

H. L. Reed. Disturbance-wave interactions in flows with crossflow. In *23rd Aerospace Sciences Meeting*, 1985.

H. L. Reed and P. Balakumar. Compressible boundary-layer stability theory. *Physics of Fluids A*, 2:1341–1349, 1990.

H. L. Reed and W. S. Saric. Linear stability theory applied to boundary layers. *Annual review of fluid mechanics*, 1996.

H. L. Reed, E. Reshotko, and W. S. Saric. Receptivity: The inspiration of Mark Morkovin. *45th AIAA Fluid Dynamics Conference*, 2015.

E. Reshotko and I. E. Beckwith. Compressible laminar boundary layer over a yawed infinite cylinder with heat transfer and arbitrary Prandtl number. *NACA Technical Report*, 1379, 1958.

A. I. Ruban and J. S. B. Gajjar. *Fluid dynamics part 1: classical fluid dynamics*. Oxford University Press, first edit edition, 2014.

W. S. Saric, H. L. Reed, and E. J. Kerschen. Boundary-layer receptivity to freestream disturbances. *Annual review of fluid mechanics*, 34:291–319, 2002.

H. Schlichting. Berechnung der anfachung kleiner störungen bei der plattenströmung. *Zeitschrift für Angewandte Mathematik und Mechanik*, 13(3):171–182, 1933.

G. B. Schubauer. Laminar-boundary-layer oscillations and transition on a flat plate. *NACA Wartime Report*, 9595, 1948.

A. M. O. Smith and N. Gamberoni. *Transition, pressure gradient and stability theory*. Douglas Aircraft Company, El Segundo Division, 1956.

F. T. Smith. On the non-parallel flow stability of the Blasius boundary layer. *Proceedings of the Royal Society A: Mathematical, Physical and Engineering Sciences*, 366(1724):91–109, May 1979.

F. T. Smith. On the first-mode instability in subsonic, supersonic or hypersonic boundary layers. *Journal of Fluid Mechanics*, 198:127–153, 1989.

F. T. Smith and S. N. Brown. The inviscid instability of a Blasius boundary layer at large values of the Mach number. *Journal of Fluid Mechanics*, 219:499–518, April 1990.

S. O. Stephen and V. Michael. Effects of porous walls on hypersonic boundary layers over a sharp cone. *AIAA Journal*, 51(5):1234–1244, May 2013.

K. Stewartson. *The theory of laminar boundary layer in compressible fluids*. Cambridge University Press, 1964.

K. Stewartson and P. G. Williams. Self-induced separation. *Proceedings of the Royal Society of London*, 312(1509):181–206, 1969.

W. Sutherland. The viscosity of gases and molecular force. *Philosophical Magazine Series 5*, 36(223):507–531, December 1893.

W. Tollmien. The production of turbulence. *NACA Technical Memorandum 609*, 1931.

A. P. Tunney, J. P. Denier, T. W. Mattner, and J. E. Cater. A new inviscid mode of instability in compressible boundary-layer flows. *Journal of Fluid Mechanics*, 785:301–323, November 2015.

J. L. Van Ingen. A suggested semi-empirical method for the calculation of the boundary layer transition region. *Delft University of Technology Report UTHL-74*, 1956.

V. Wartemann, H. Lüdeke, and N. D. Sandham. Numerical investigation of hypersonic boundary-layer stabilization by porous surfaces. *AIAA Journal*, 50(6): 1281–1290, June 2012.